Inorganic Chemistry Communications 146 (2022) 110149

Contents lists available at ScienceDirect

Inorganic Chemistry Communications

journal homepage: www.elsevier.com/locate/inoche

The influence of activated carbon annealing temperature on sunlight-driven photocatalytic dye degradation and biological activity

M. Amalanathan [a,*], M. Aravind [b,*], Nafis Ahmed [c], M. Sony Michel Mary [d], P. Velusamy [e], T. Kumaresubitha [f], Razia Noreen [g], Shafaqat Ali [h,i,*]

[a] Department of Physics, Nanjil Catholic College of Arts and Science, Kaliyakkavilai, Kanyakumari, Tamil Nadu 6291513, India
[b] Department of Physics, National Engineering College, K.R Nagar, Kovilpatti, Thoothukudi, Tamil Nadu 628503, India
[c] SSN Research Centre, Sri Sivasubrananiya Nadar College of Engineering, Kalavakkam 603110, Tamil Nadu, India
[d] Department of Physics, Nesamony Memorial Christian College Marthandam, Kanyakumari, Tamil Nadu 629165, India
[e] Department of Physics, Thiagarajar College of Engineering, Thiruparankundram, Madurai 625015, Tamil Nadu, India
[f] Department of Botany, Pachaiyappa's College, Chennai 600 030, Tamil Nadu, India
[g] Department of Biochemistry, Government College University, Faisalabad
[h] Department of Environmental Sciences & Engineering, Government College University, Faisalabad, 38000, Pakistan.
[i] Department of Biological Sciences and Technology, China Medical University, Taichung, 40402, Taiwan

ARTICLE INFO

Keywords:
Activated carbon
E-Coli
Graphitic carbon
Methylene blue
Photocatalytic degradation

ABSTRACT

In this study, activated carbon (AC) produced from jasmine flowers was effectively manufactured using a hydrothermal carbonization procedure at various annealing temperatures. The XRD pattern revealed the graphitic phase of carbon. The surface morphology of nanoparticles exhibits uneven shapes. To investigate the photocatalytic activity of methylene blue (MB), it was photodegraded using visible light irradiation. Under solar light irradiation, the prepared activated carbon was used as a potential photo catalyst for the photo catalytic degradation of brilliant green dye, which revealed 96% degradation. The antibacterial activity of activated carbon was tested against *S. Aureus (*MTCC-737) and *E. coli* (MTCC-443) microbial pathogens, and the zone of inhibition layer was studied. To the best of our knowledge this is the first study to use jasmine flower based AC as a photocatalyst for the efficient breakdown of MB dye.

1. Introduction

Water is an important component of daily existence. According to the UNESCO World Water Assessment Programme (WWAP), one hundred million humans, one million seabirds, and one hundred thousand marine animals perish annually due to water pollution [1]. Industrial sludge, heavy metals, pesticides, organic dyes, and other substances greatly pollute the water supply. Humans acquire a variety of illnesses due to water contamination. Even minute amounts of dye can degrade water quality. During the colouring process, the textile and paper industries release a large amount of dye waste [2]. Methylene blue is a heterocyclic aromatic dye that appears blue when oxidised but is colourless when reduced. Methylene blue causes loss of coordination, fast heartbeat, hallucinations, fever, nausea, vomiting, and diarrhoea. The non-biodegradable colour methylene blue causes several health issues and environmental pollutions [3]. Traditional techniques cannot breakdown methylene blue adequately. Only photocatalysis totally destroys dye without producing sludge or by-products. It is frequently used to treat coloured molecules as a result of its low cost, environmental friendliness, and absence of sludge [4]. Because of their large surface area and porosity, activated carbons (AC) are commonly used as an active material for methylene blue degradation. Activated carbon is utilised in a variety of environmental applications, including wastewater treatment, mercury removal, water purification, and gas purification, as well as energy storage, super capacitors, and batteries [5]. Corn cob, wheat straw, and rice hull in agricultural biomass-derived activated carbon [6], hazelnut shells [7], walnut shells [8], and peanut shells [9], egg-shells [10], and coconut shells [11] were utilised. Activated carbon is produced using a variety of synthetic techniques, including pyrolysis, physical activation, and chemical activation. To convert carbon, the physical activation process requires high temperature and pressure. By completing the heat degradation of raw material with chemical reactions, chemical activation may be done in a single step. Chemical

* Corresponding authors.
E-mail addresses: nathan.amalphysics@gmail.com (M. Amalanathan), aravind-sh@nec.edu.in (M. Aravind), shafaqataligill@yahoo.com (S. Ali).

https://doi.org/10.1016/j.inoche.2022.110149
Received 4 June 2022; Received in revised form 9 October 2022; Accepted 25 October 2022
Available online 30 October 2022

Nomenclature

AC	Activated carbon
FT-IR	Fourier Transform Infrared Spectroscopy
H_2SO_4	Sulphuric acid
H_3PO_4	Ortho phosphoric acid
HCL	Hydrochloric acid
K_2CO_3	Potassium carbonate
KOH	Potassium hydroxide
MB	Methylene Blue
Na_2CO_3	Sodium Carbonate
NaOH	Sodium hydroxide
O_2	Superoxides
OH	Hydroxyl radicals
SEM	Scanning Electron Microscope
TEM	Transmission Electron Microscope
XRD	X-ray Diffraction
$ZnCl_2$	Zinc Chloride

activation operations are conducted using acidic reagents, such as $ZnCl_2$, H_3PO_4, HCL, and H_2SO_4, or with essential reagents, such as KOH, K_2CO_3, and NaOH. Because they are very stable and can transfer electricity, carbonaceous materials can be used to stabilise hybrid systems and make photocatalytic energy happen.

Zhang et al., 2021 [12] stated that carbon stalk-derived hydrothermally treated activated carbon for the photodegradation of methylene blue removal obtained a 99.4% degradation efficiency at a 150 mg/L methylene blue concentration. Nizam et al., 2021 [13] described activated carbon produced from rubber seed and shell for cationic methylene blue elimination. The interaction and hydrogen bonding result in the elimination of methylene blue. Wang et al., 2020 [14] generated activated carbon by utilising phosphoric acid as the activation agent in an integrated corncob hydrothermal carbonization process. Activated carbon's surface area was measured at 480 m^2/g. The ability of activated carbon to absorb dye rose from 41% to 82%. Emrooz et al., 2020 [15] created micro and mesoporous activated carbon produced from Azolla to remove methylene blue. According to this study, at the conclusion of 120 min, activated carbon mediated by jasmine flowers achieves a maximum degradation efficiency of 94%. Comparing the observed results to earlier reports. The hydrothermal carbonization method is the simplest, most ecologically friendly, time-and energy-efficient method for incorporating nanoparticles. The fundamental objective of this study is to produce a low-cost, high performance, low-temperature absorbent. Lin et al., 2021 [16]. The activator NaOH improves the surface area and photocatalytic activity of the material.

This study seeks to manufacture the catalytic activity of activated carbon by degrading methylene blue dye under UV irradiation using conventional and simple carbon. Jasmine flowers will be used as a biomaterial in an affordable hydrothermal carbonization process. In addition, the biological activities of activated carbon at various temperatures of annealing were evaluated against a variety of microorganisms that cause disease. This research covers, to the best of our knowledge, the production of activated carbon using jasmine flower extract. The annealing temperature regulated the nanoparticles' form and size.

2. Experimental procedure

2.1. Materials

All of the chemicals and reagents are utilized without being purified further. Sodium hydroxide (NaOH), Methylene blue ($C_{16}H_{18}ClN_3S$), Hydrochloric acid (HCL) were purchased from Merck. Methylene blue is a pollutant dye used for degradation.

2.2. Preparation of activated carbon

Jasmine flower-derived activated carbon was effectively produced by the hydrothermal carbonization method. Jasmine flower powder was added to 20 ml of distilled water togetherwith an activating agent (NaOH) at a ratio of 4:1, followed by three hours of stirring. The solution was transferred to a 100 ml Teflon autoclave and placed in an oven at 100 degreesCelsius for three hours. To eliminate untreated biomass, the solution was cooled, filtered, and washed with distilled water and HCL. The sample was baked in an oven at 80 °C for one night, and then it was put together at different annealing temperatures (400 °C, 500 °C, 600 °C) [17].

2.3. Characterization techniques

A PAN analytical XPERT PRO diffractometer with Cu-K radiation (-1.54) was used to identify the structural and phase characteristics of activated carbon generated from jasmine flowers. FT-IR spectroscopy was used to analyses functional groups. The FT-IR spectra were captured using a Perkin Elmer spectrophotometer. SEM analysis was used to analyse surface morphology and particle size measurement. The Joel JSM 6390 Scanning Electron microscope was used for SEM examination. The high-resolution transmission electron microscopy was captured with the Gatan Quantum ER 965. The spectrum was acquired using Nanoplus and a particle size analyzer.

2.4. Photo catalytic performance of activated carbon

In the photo degradation investigation, the as-prepared photo catalyst (AC) was disseminated in 100 ml aqueous solution of MB dye. The solution was ultrasonically agitated for 30 min in a dark room before being exposed to radiation to provide the right adsorption/desorption conditions. The solution was then exposed to direct sunlight while being stirred magnetically. The reaction solution was kept at 37 °C while 5 ml of the suspension was taken every 10 min and centrifuged for 10 min at 3000 rpm. The UV–Vis spectrophotometer was then used to analyse the photodegradation behaviour [18].

2.5. Reactive species experiment

Reactive oxidative species entrapment studies were carried out to investigate the potential photocatalyst mechanism of MB dye over the AC. By adding 1.0 mM of disodium ethylenediamine tetra-acetic (h^+), ethanol (e^-), isopropyl alcohol ($OH^•$), and benzoquinone ($O_2^{•-}$), respectively, different types of scavengers were used in this experiment to trap photogenerated electrons, holes, hydroxyl radicals, and superoxide radicals. For the scavenger investigation, the same photocatalytic experimental methodology was used.

2.6. Antibacterial activity

AC synthesised using jasmine flower were evaluated for their ability to combat *E-Coli* and *Staphylococcus aureus* using the disc diffusion method. All samples were inoculated into sterile nutrient broth (Hi Media) (5 ml). Additionally, they were incubated for 3 to 5 h to bring the culture up to McFarland standards (106 CFC/ml). By spreading 100 ml of revived culture on Mueller Hinton-Agar/Hi Media using a spreader, 3 repetitions of each individual organism were organised. 50 ml samples of AC nanoparticles were put in one well (7 mm- diameter) (7 mm-diameter). All of the petri plates with organisms whose antibacterial effect was indicated by a zone of inhibition in mm were kept in the incubator at 37 °C for one day.

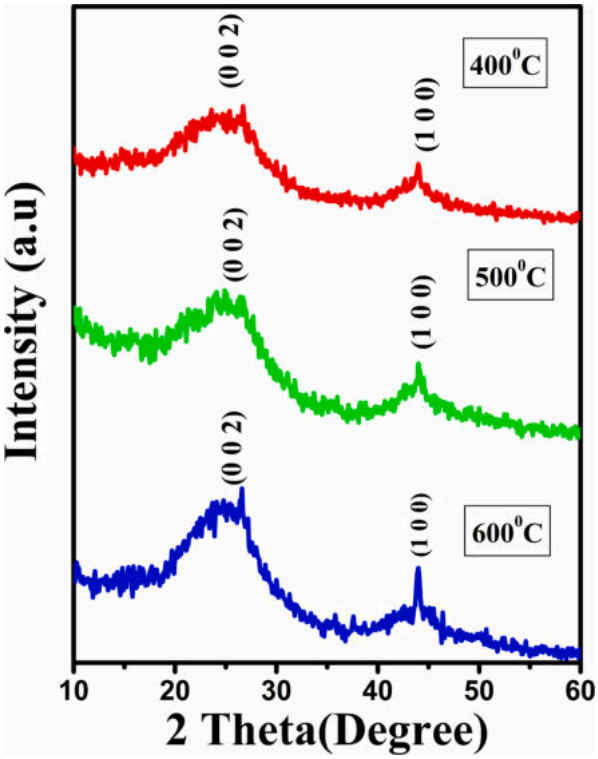

Fig. 1. XRD spectrum of Activated carbon (AC) NP's.

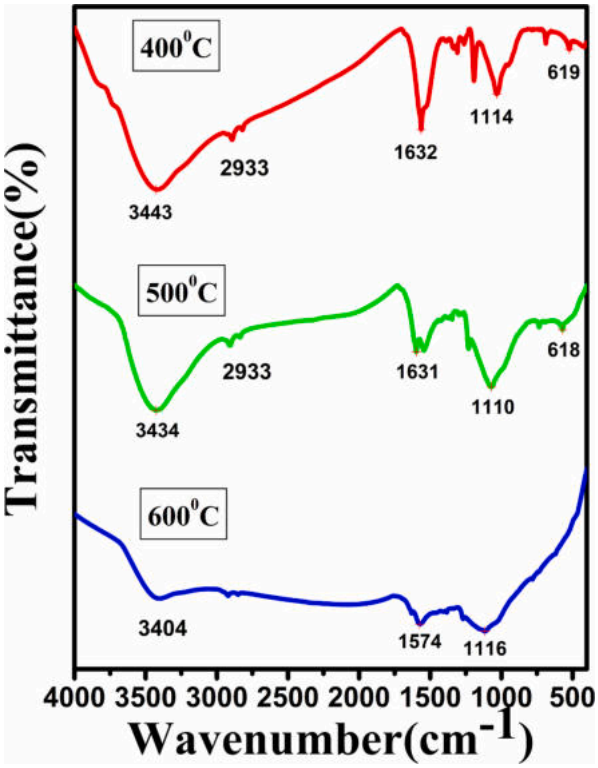

Fig. 2. FTIR spectrum of Activated carbon (AC) NP's.

3. Results and discussion

3.1. X-Ray diffraction

Using XRD analysis, the phase and crystalline nature of activated carbon were determined. Fig. 1 depicts the XRD pattern of activated carbon at various temperatures of annealing. The X-ray diffraction peaks at 26° and 43.2° correspond to Bragg reflection planes (0 0 2) and (1 0 0), respectively. The observed pattern corresponded to JCPDS. 7440-44-0 [19] is the file number. The peak at 26° shows disordered carbon or amorphous carbon, whereas the peak at 44°denotes the graphitic phase of carbon. Activated carbon's X-ray diffraction reveals a hexagonal graphite structure that corresponds well with JCPDS file number 75-1621 [20]. Due to an increase in the interplanar distance of the activated carbon, the noticeable peak visible at 43.2° progressively shifts upward when the annealing temperature is increased. The increase in annealing temperature facilitates the proper migration of atoms inside the lattice [21]. The small change in diffraction peak locations may be attributable to the presence of strain in the crystal structure, which is common in nanocrystalline produced using an eco-friendly process.

3.2. Fourier Transform Infrared spectroscopy

FT-IR spectroscopy was utilized to analyse the functional groups of the studied activated carbon. Fig. 2 depicts the FT-IR spectra of activated carbon at various annealing temperatures. The designated band at 3744, 3434, 3443, 3393 cm^{-1} corresponds to the O-H stretching vibration of alcohol, phenol, carboxylic acid, or water [22]. This frequency corresponds to the C-H stretching vibration of the aliphatic molecule. The band at 1631 cm^{-1}corresponds to the C = C transition. Vibrational stretching of the aromatic ring [10]. The band seen at 1578 cm^{-1} corresponds to the sulphate group's adsorption. The band found at 1337 cm^{-1} corresponds to C-H asymmetries. C-O stretching vibrations are represented by the band at 1270 cm^{-1}. The detected band at 1110–1114 cm^{-1}corresponds to the vibrational bending of CO-H bonds. The peaks at 780 and 619 cm^{-1} are from the O-H group [23,24]. Annealing temperature increases, water molecules are eliminated. Due to varying annealing temperatures, there is a little difference in peak shift and intensity.

3.3. Scanning electron microscope with EDX

Using SEM and TEM photographs, the morphological analysis of activated carbon was observed. Fig. 3A-D displays SEM images of activated carbon heated to 400 °C, 500 °C, and 600 °C, respectively. The enhanced surface morphology of activated owing to a higher annealing temperature [25] is revealed by SEM pictures of irregular and agglomerated nanoparticles. A number of holes and cavities are present on the surface of activated carbon as a result of the emission of hot gases during the annealing procedure. Energy Dispersive X-ray Analysis was used to identify the components of the produced activated carbon nanoparticles (EDX). Carbon and oxygen peaks have been proven to exist. The remaining small peaks are attributable to plant extracts, and their quantities are negligible. Fig. 4 A-C depicts the elemental analysis spectrum.

3.4. Transmission electron microscope

Transmission electron microscopy (TEM) images of activated carbon nanoparticles at 600 °C are shown in Fig. 5 A and B. The uneven forms of activated carbon result from theparticles' synthesis. The photos demonstrate the activated carbon's high surface area, which can hinder the recombination process and potentially activate charge carriers. These approaches are quite effective at catalysis.

3.5. Particle size analyser

Fig. 6 displays the DLS spectrum of activated carbon. At 400 °C, 500 °C, and 600 °C, the average particle size of activated carbon is 120 nm, 185 nm, and 190 nm, withpolydisperse index values of 0.387, 0.375, and 0.345, respectively. According to the DLS spectrum, particle

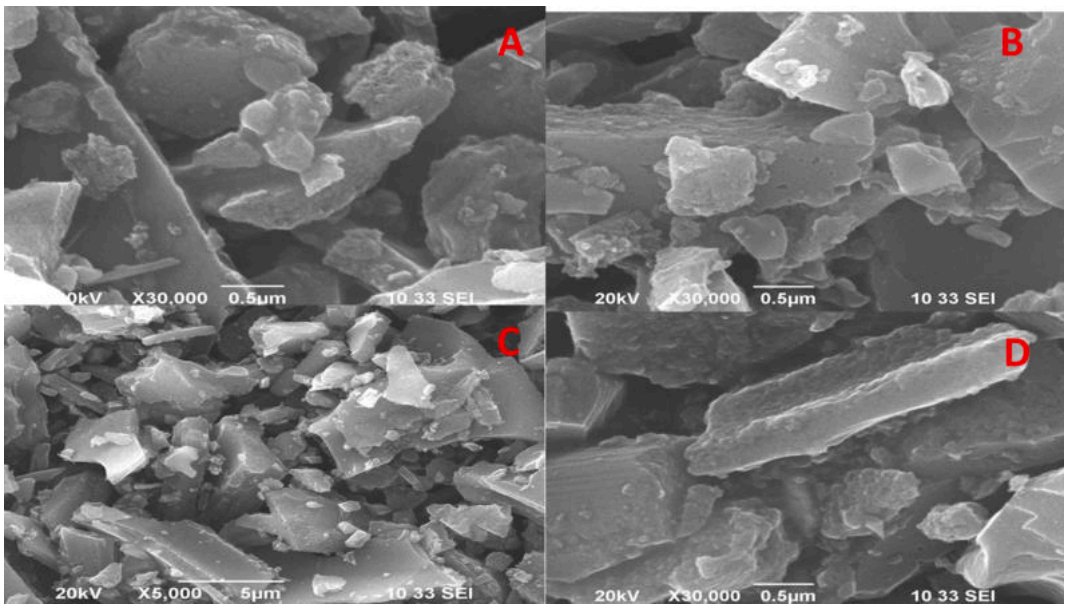

Fig. 3. SEM images of Activated carbon (AC) a. (400 °C), b (500 °C), c and d (600 °C) at different magnifications.

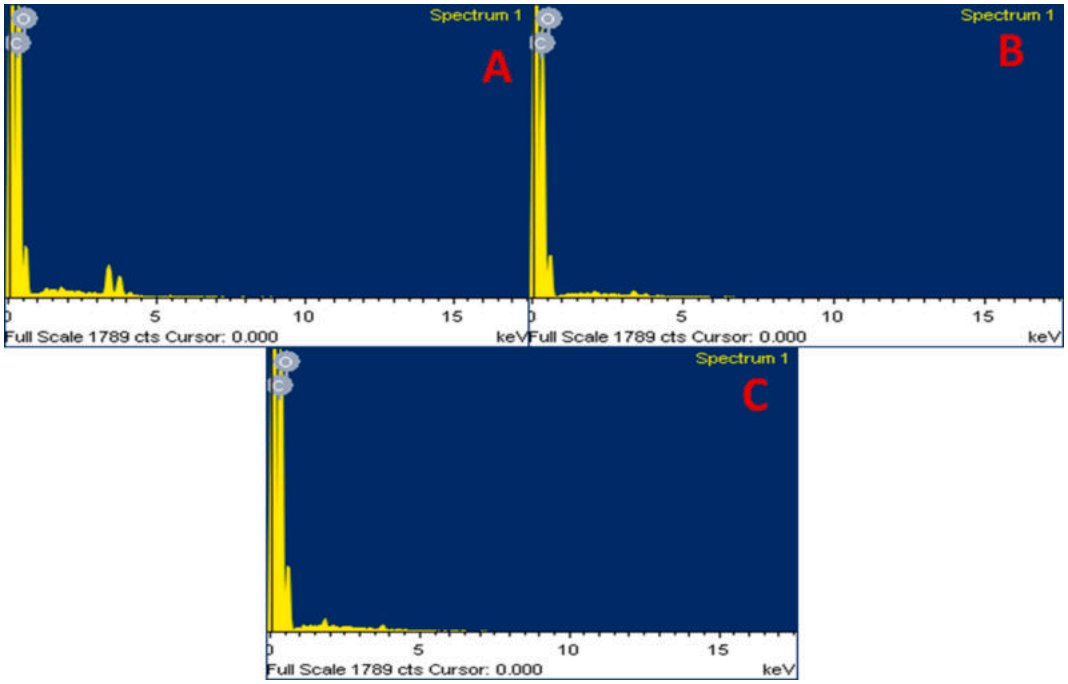

Fig. 4. (A-C) EDX spectra of Activated carbon (AC) NP's.

size values increase as the temperature rises.

3.6. UV–Visible spectroscopy

UV–Visible spectroscopy was used to study the optical characteristics of activated carbon. Fig. 7 depicts the absorbance spectra of activated carbon at various temperatures of annealing. The UV spectrum may be used to forecast surface morphology, oxygen deprivation, and contaminants. As a result of the electrical shift from the valance band to the conduction band, activated carbon with a preset absorbance peak at 249 nm absorbs light. The values of the energy band gap may be estimated using the Tauc plot.

$$\alpha h\nu = (h\nu - Eg)^{n} \quad (1)$$

Where is the absorption coefficient, α represents a constant, h represents the energy of light, and Eg represents the energy bandgap [26]. The energy band gap values of activated carbon at temperatures of 400 °C, 500 °C, and 600 °C are 2.04 eV, 2.00 eV, and 1.94 eV, respectively. Due to an increase in annealing temperature, band gap values may fluctuate somewhat. Bandgap energy values decrease owing to an increase in crystallite size and annealing temperature. This phenomenon suggests that the interatomic distance increases when the amplitude of atomic vibrations grows in response to an increase in thermal energy. The annealing temperature decreased the optical band gap of activated carbon (Fig. 7 b-d), with 600 °C annealing reducing the optical band gap somewhat more than 400 °C and 500 °C annealing. However, the altering effects on the band gap of activated carbon did not appear to be

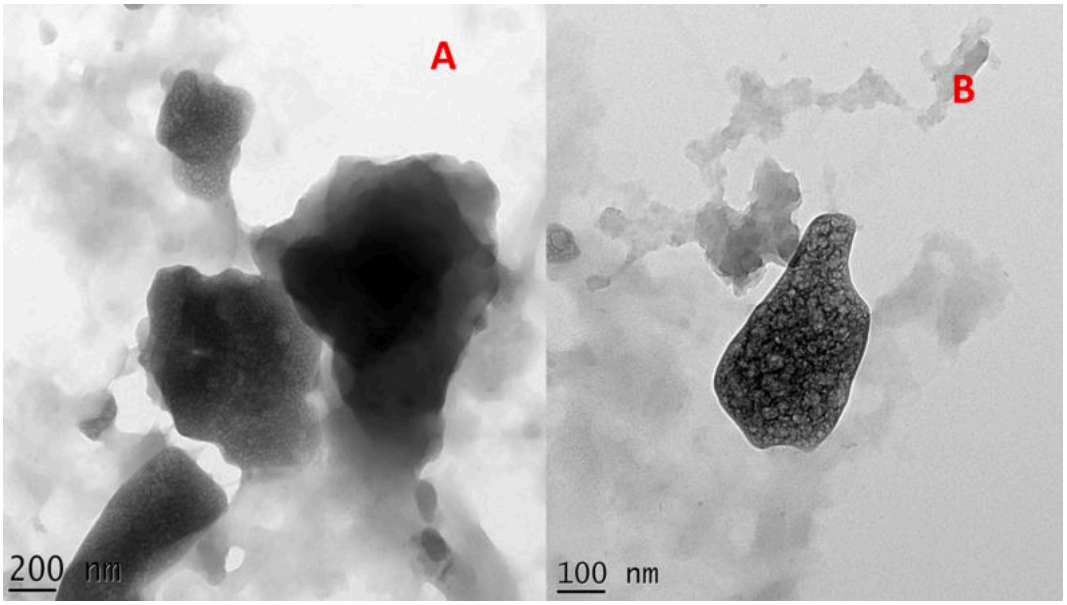

Fig. 5. A, & B TEM images of Activated carbon (AC) NP's at (600 °C).

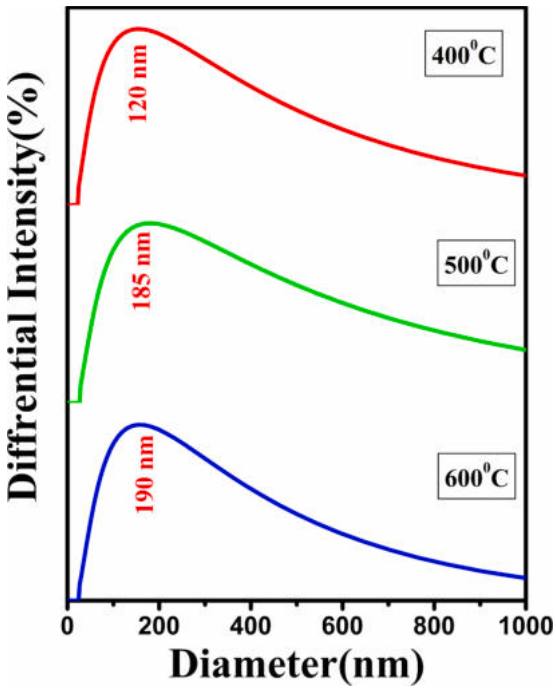

Fig. 6. (A-C) DLS spectra of Activated carbon (AC) NP's.

significant. The effects of thermal annealing on photocatalytic activity and its dependence on annealing temperature cannot be explained only by the optical bandgap decrease generated by thermal annealing, according to these results.

3.7. X-ray photoelectron spectroscopy

The XPS analysis was used to determine the surface electrical state and chemical composition. The XPS spectra of synthesised activated carbon (600 °C) were shown in Fig. 8. The synthesised Activated carbon contains C and O elements, according to the XPS survey spectra. Two unique peaks can be seen in the X-ray photoelectron spectroscopy (XPS) spectra of AC at energies of 284.5 and 532.2 eV, which are ascribed to carbon and oxygen, respectively. Fig. 8 displays the XPS high resolution narrow scan C 1s spectrum. It has a large peak at 284.5 eV, which is consistent with a non-functionalized carbon, as well as contributions from aliphatic C sp^3 and C sp^2 hybridization, all of which are associated with the carbon surface. The existence of a C-C/C-H transition in an aromatic compound might be responsible for the binding energies 284.5 shown in the figure. The range 532.2 eV was where the surface O 1s peak was seen. The O 1s signal is not very responsive to the kind of oxygen ring bonds [27].

3.8. Photocatalytic activity

The photocatalytic activity of methylene blue (MB) was investigated by observing its photodegradation under visible light irradiation. Fig. 9 depicts the photocatalytic activity of activated carbons at various annealing temperatures. Activated carbon breaks down methylene blue quickly because its pores are very active and it has a lot of surface area. Maximum absorbance spectra of methylene blue are observed at 650 nm due to the absorption of the azo bond present in MB dye [28]. When ultraviolet light is allowed to penetrate through the surface of carbon, electrons from the valance band are stimulated into the conduction band, leaving holes. The positive holes interact with H_2O to produce free radicals ($OH^{\bullet}$), whereas photo generated electrons interact with the surface of carbon to make superoxides (O_2^-). Free radicals ($OH^{\bullet}$) and superoxides ($O_2^{\bullet-}$) are a major cause of methylene blue degradation [29,30,31]. Together, these reactive radicals break down organic substances into CO_2, H_2O, and other minerals. Oxygen vacancies and defects turn into active centres to collect photo induced electrons during the photo catalytic reaction process. As a result, photo induced electron and hole recombination can be successfully suppressed. The absorption of O_2, which is transformed into superoxide radicals (O_2•-) by contact with photo induced electrons, can also be aided by an increase in oxygen vacancies. These superoxide radicals are active in the oxidation of organic contaminants by generating additional radicals like OH• and H_2O_2. Fig. 10 is a diagram illustrating photocatalytic activity. Free radicals and superoxide react with dye molecules to produce carbon dioxide, water, and other organic chemicals. During deterioration, the following processes occur:Fig. 11.

$$\text{Carbon} + h\nu \rightarrow h^+ + e^- \quad (2)$$

$$h^+ + OH^- \rightarrow OH^* \text{ (Hydroxyl radicals)} \quad (3)$$

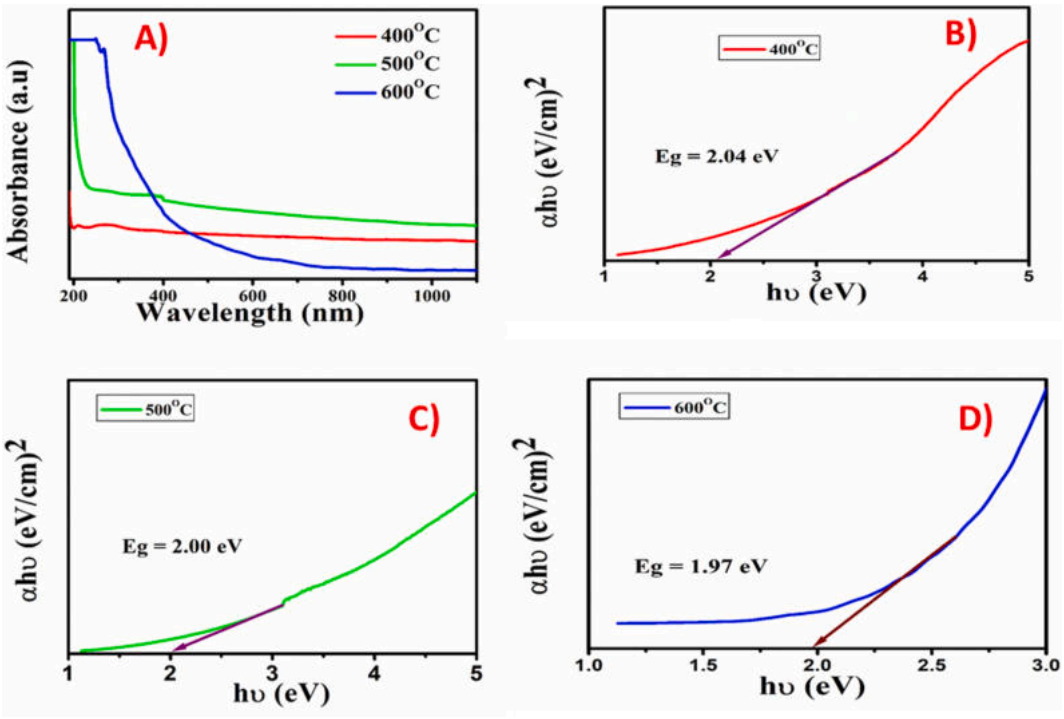

Fig. 7. A UV-absorbance spectrum and (B-D) Tauc plot of Activated carbon (AC) NP's.

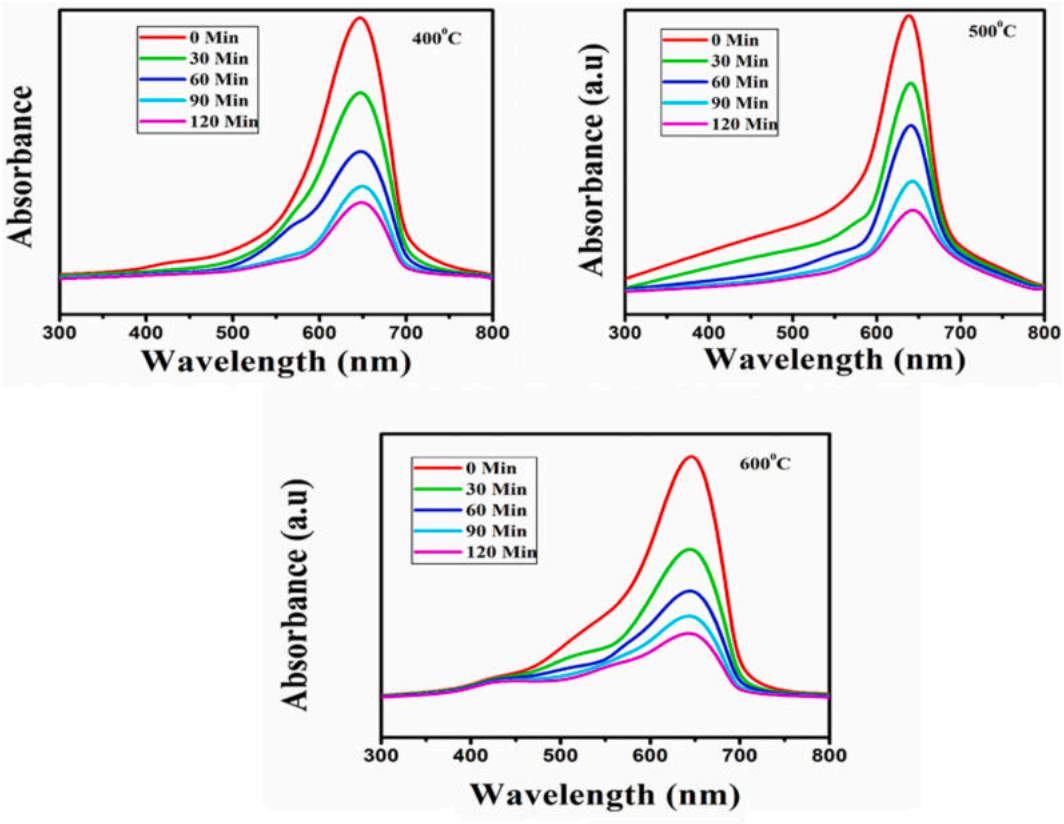

Fig. 8. (a-c) XPS spectra of activated carbon (600 °C).

$h^+ + H_2O \rightarrow H^+ + OH^*$ (4)

$e^- + O_2 \rightarrow O_2$ (5)

$OH^* + \text{MB dye} \rightarrow H_2O + CO_2$ (Degradation products) (6)

$O_2^{\bullet --} + \text{MB dye} \rightarrow H_2O + CO_2$ (Degradation products) [32] (7)

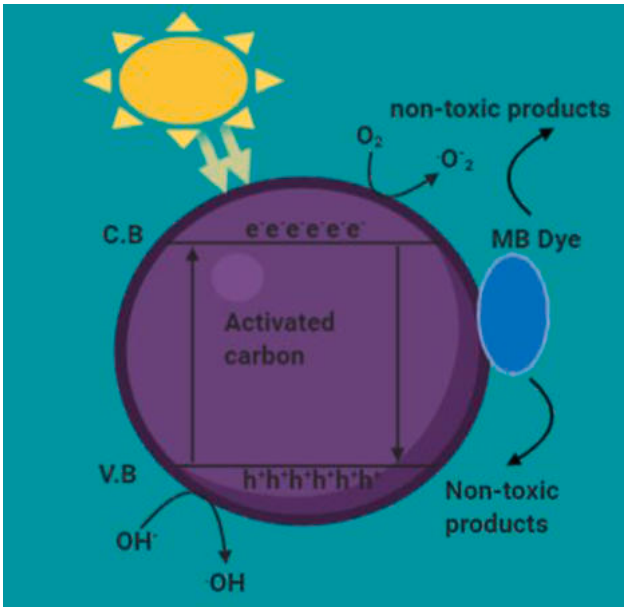

Fig. 9. Time-dependent UV–vis absorption spectra for degradation of MB (400 °C, 500 °C and 600 °C).

Activated carbon annealed at different temperatures (400 °C, 500 °C, and 600 °C) exhibits maximum degradation efficiencies of 86%, 90%, and 94% after 2 h, respectively. The conversion of the amorphous phase to the graphitic phase enhances the efficiency of degradation. Photocatalytic performance is improved by highly active pores and surface area [33]. The surface polarity, surface area, and aromaticity that result from the adsorption of organic pollutants [34] are crucial properties. During photodegradation, methylene blue is transformed to leuco methylene, resulting in a shift in hue from dark blue to colourless [35]. Several characteristics, including carrier recombination, particle size, surface area, surface acidity, and the presence of a greater number of hydroxyl groups, affect the photocatalytic activity of catalytic material.

In this study and previous research, 600 °C (sample 3) exhibits a greater percentage of degradation than 400 °C (sample 1). Due to the higher surface-to-volume ratio and low recombination rate of electron-hole pairs formed by optical exposure, theenhanced photocatalytic activity can be attributed to the many accessible surface states. As part of this investigation, the comparison in Table 1 shows how unique the study is about how methylene blue breaks down.Table 2.

3.8.1. Photocatalytic performance of activated carbon based photocatalyst

The results obtained are summarized in Table 1 and compared to earlier publications on photocatalyst, including activated carbon. Under the impact of UV or visible light, several nanostructures of photocatalyst based on activated carbon were utilised to degrade organic dyes. According to Table 1, activated carbon generated from egg shells can breakdown 82% of Methylene Blue dye for 120 min in the presence of sunshine, and the majority of reported activated carbon nanoparticles

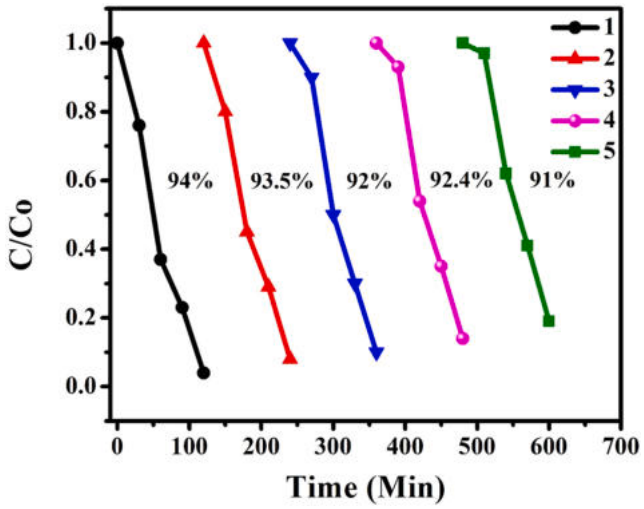

Fig. 11. shows reusability of activated carbon (600 °C) after 5 cycles.

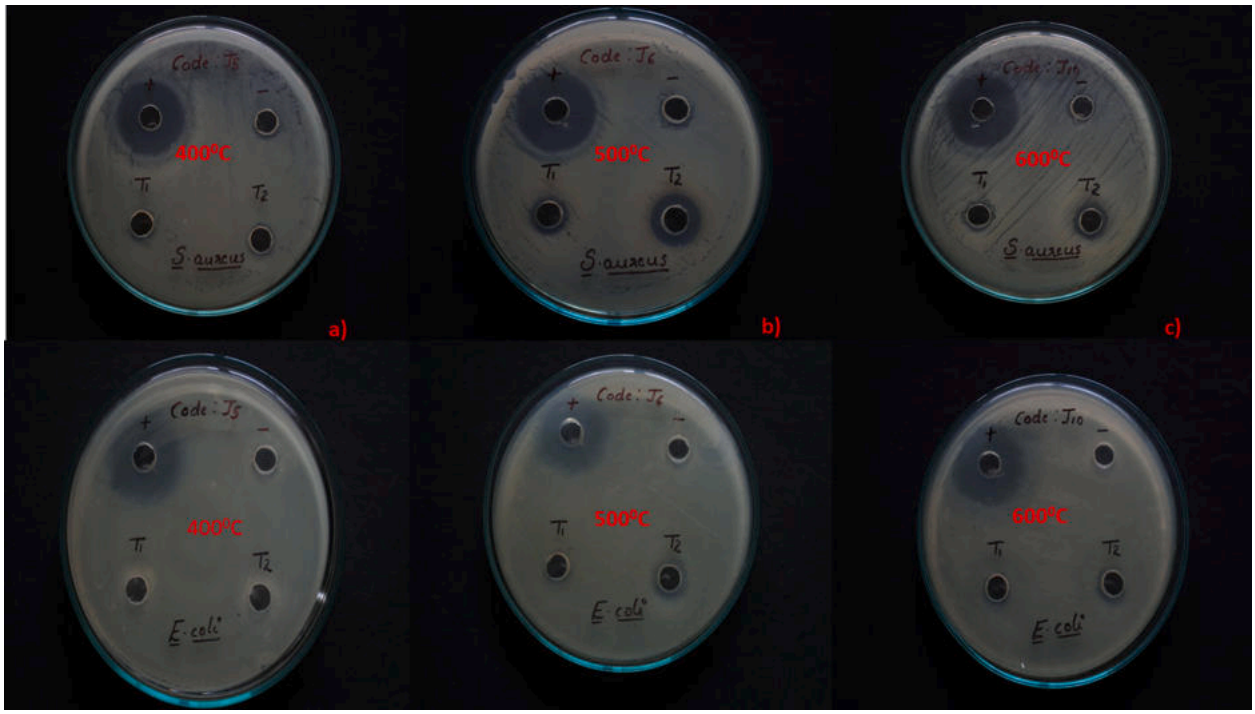

Fig. 10. Schematic representation of Photocatalytic degradation of MB dye.

Table 1
Photocatalytic performance of AC-based photocatalyst for the degradation of organic dyes in aqueous solution.

S.No	Nanocatalyst	Time	Dye	Degradation efficiency	References
1.	Activated Carbon (Coconut shell)	120 mins	Methylene blue	68%	[36]
2	Activated Carbon (coffee grounds)	150 Min	Methylene blue	20.97%	[37]
3	Activated Carbon (Jack fruit leaves)	30 Min	Methylene blue	84%	[38]
4	Activated Carbon (Egg shell)	180 Mins	Methylene blue	82.8%	[39]
5	Activated Carbon (fir bark)	180 Mins	Methylene blue	96%	[40]
6.	CuS, CdS and CuS-CdS	10 Mins	Methylene blue	80, 59 and 99.97%	[41]
7	La-doped ZnO	90 Mins	Methylene blue	88%	[42]
8	Zinc sulfide	60 Mins	Rhodamine B	93	[43]
9	ZnS	90 min	Brilliant green	88	[44]
10	ZnS, CdS and CuS	60 min	Bromothymol blue dye	63.88%), 83.42% and 46.23%	[45]
11	CdS and Sn-doped CdS	180 min	Methylene blue	91.39% and 97.56%	[46]
12	CdS, TiO_2, CdS-TiO_2	60 min	Acid Blue dye	68%, 09%, and 84%	[47]
13	ZnO-AC/A + P	60 min	Malacite Green and Congo Red	92%	[48]
14	ZnO-NR/ACF	120 mins	Methylene blue	90%	[49]
15	Nano Zinc Oxide/Nanohydroxyapatite	100 min	Methylene Blue	91%	[50]
16	Activated Carbon (Jasminum)	120 Mins	Methylene blue	94%	This Work

Table 2
Antibacterial efficacy of AC.

Nanomaterials	Bacterial pathogen	Zone of inhibitions (mm)	References
Zinc oxide	*Staphylococcus aureus*	29	[57]
	Escherichia coli	22	
Ag NPs	*Aspergillus niger*	25	[58]
	Microsporum canis	23	
	Staphylococcus aureus	17	
Ag-NPs	*Escherichia coli*	7	[59]
	Staphylococcus aureus	12	
Ag-NPs	*Escherichia coli,*	15	[60]
	Klebsiella pneumoniae	10	
	Salmonella Typhimurium	20	
	Salmonella Enteritidis	20	
AC	*Aspergillus flavus*	21	[61]
	Aspergillus Niger	22	
	Fusarium solani	22	
	Candida albican	24	
	S. cerevisae	23	
AC (600 °C)	*E scherichia coli*	12	Present work
	Staphylococcus aureus	10	

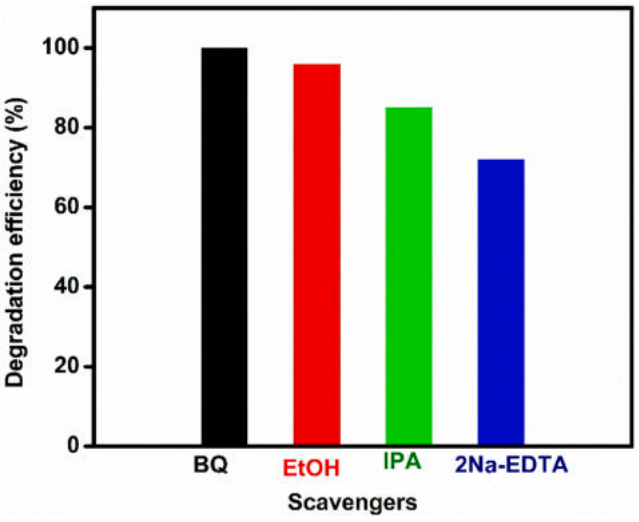

Fig. 12. Scavenger studies of activated carbon (600 °C).

can degrade the dye for more than two hours. However, after 120 min of sun irradiation, 600 °C activated carbon had a maximum photodegradation efficiency of 94% for MB dye. In the near future, the activated carbon in its current state may be useful for the photodegradation of MB dye using sunlight.

3.9. Reusability

Fig. 12 shows reusability of activated carbon (600 °C) after 5 cycles. The long-term stability and reusability of the optimized AC photocatalyst (600 °C) towards the degradation of MB dye was studied under five cycles of sunlight exposure. The concentration of MB dye should be constant in each cycle, and the recovered centrifuged catalyst is used in subsequent cycles of the degradation process. The catalyst remains efficient and has remarkable photostability even after four cycles. Maximum MB dye degradation occurs after 120 min, and the efficiencies for the first, second, third, fourth, and fifth cycles are 94%, 93.5%, 92%, 92.4%, and 91%, respectively. The results of the present investigation therefore support the fact that AC formed during the photocatalytic destruction of MB dye under sunlight irradiation may exhibit excellent photostability, stability and excellent photo corrosion resistance.

3.10. Scavenger studies

Fig. 12 shows the experiment for capturing reactive species while AC is being photocatalysis by sunlight. It was found that the addition of IPA and 2Na-EDTA scavengers reduced the photocatalytic efficacy of AC toward the degradation of MB dye. However, the degradation of MB in comparison to AC as a photocatalyst is not noticeably altered by the addition of ethanol and BQ. These findings suggest that the main reactive species involved in the photocatalytic breakdown of MB under solar illumination are holes and hydroxyl radicals.

3.11. Electrochemical impedance spectroscopy

Using an electrochemical analyzer in a typical three-electrode setup, measurements for Mott-Schottky (MS) and electrochemical impedance spectroscopy (EIS) were made. The working electrode's active area was 0.5 cm^2 by 1 cm^2. EIS was carried out using an open circuit voltage of 0.2 V and an AC voltage amplitude of 5 mV, with a frequency range of

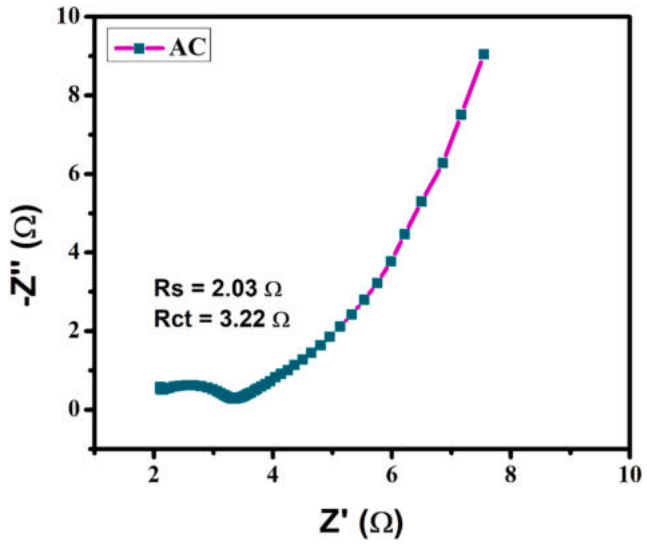

Fig. 13. Electrochemical impedance spectra of o activated carbon (600 °C).

0.1 Hz to 100 kHz. The analysis of the photogene rated charge separation and transfer during the photocatalytic process was done using the electrochemical impedance spectroscopy (EIS) of as prepared activated carbon. Generally, the Nyquist plot's semicircle's radius represents the rate of reaction taking place at the photocatalyst's surface. The reduced arc radius in the Nyquist plot (see Fig. 13) suggests that surface imperfections in the produced AC may be the cause of the rapid reaction rate and efficient charge transfer with decreased electrical resistance [51].

3.12. Morphological stability of prepared AC

TEM and SEM were used to assess the morphological stability of the recycled/recovered photocatalyst. According to TEM and SEM analysis, even after the third cycle of photodegradation, the AC authenticates that no structural change has been seen even after fifth cycle (Fig. 14). The fact that the degradation efficiency was still 96% even after three cycles further demonstrates the high photostability and reusability of the as-prepared AC under simulated visible-light irradiation.

3.13. Antibacterial activity

Fig. 15 depicts the antibacterial action of activated carbon. The antimicrobial effectiveness of activated carbon was evaluated using the disc diffusion technique. The antibacterial activity of gram-positive (*S. aureus*) and gram-negative (*E. coli*) bacteria was evaluated (*E-Coli*). Possible response mechanisms include the following:

1. Electrostatic interaction between nanoparticles and the cell wall membrane
2. Individual particle diffusion to the cell membrane.
3. Superoxides and free radicals are produced.

It is possible that superoxides and free radicals would arise since the experiment was conducted in a dark environment [52]. The interaction between the carbon surface and the negative cell wall membrane of *E-Coli* results in electrostatic attraction, and the rupture of the cell wall leads to protein denaturation and cell death. The adsorption ability of carbon leads to effective antibacterial activity against *E-Coli* [53]. The cell wall of Gram-negative bacteria has an outer lipopolysaccharide membrane and a thin layer of peptidoglycan, whereas the cell wall of Gram-positive bacteria has a thick layer of peptidoglycan [54]. These results suggest that not all positively charged NPs are more biocidal than negatively charged AC NPs toward the pathogens under study. Furthermore, it is challenging to say which pathogens are more vulnerable to exposure to positively charged AC NPs. In the literature, it is hypothesised that the electrostatic attraction between negatively charged microbial cell membranes and AC NPs with a positive surface charge can significantly increase the adhesion of AC NPs, giving positively charged AC NPs stronger antibacterial activities than negatively charged AC NPs. In this investigation, bio-formed activated carbon nanoparticle agglomerates were utilized. These large aggregates are less likely to penetrate the bacterial cell membrane and cause internal harm. It appears that direct interactions between activated carbon nanoparticles and the membrane surfaces of bacteria result in the mechanical rupture of the cell wall, which might be an efficient mechanism for the antibacterial activity of the sample. It was discovered that when the concentration of activated carbon-NPs increased, the size of the inhibitory zone grew. Crystalline structure and particle shape have a minimal effect on antibacterial activity, but surface area and concentration have a significant impact [55,56]. Gram-positive bacteria result in a smaller inhibition zone because it is difficult to destroy *S. aureus'* cell wall. Compared to amorphous carbon, the graphitic phase of carbon has superior antibacterial activity. Antibacterial activity is determined by the surface area, crystallinity, crystallite size, and particle size. A high concentration of activated carbon results in a larger inhibitory zone. The fact that the activated carbon material being studied is very good at killing bacteria shows that it is a great choice for treating wastewater.

4. Conclusion

This work used a hydrothermal carbonization method and a jasmine flower as biomass to make activated carbon. The hexagonal graphite phase of carbon is shown by the XRD pattern. FT-IR spectroscopy was used to identify the functional groups in activated carbon. The

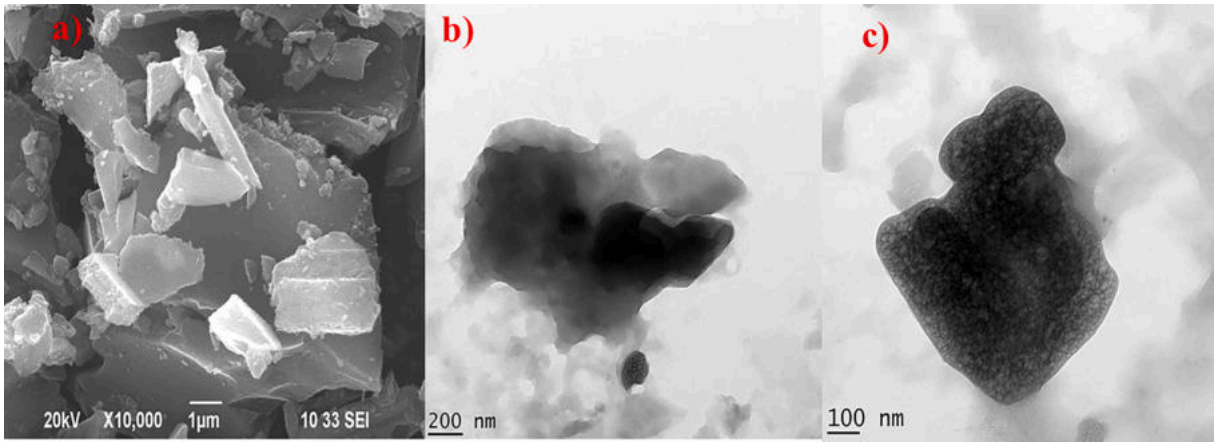

Fig. 14. a, b, c Morphological stability of activated carbon (600 °C) after 5 cycles.

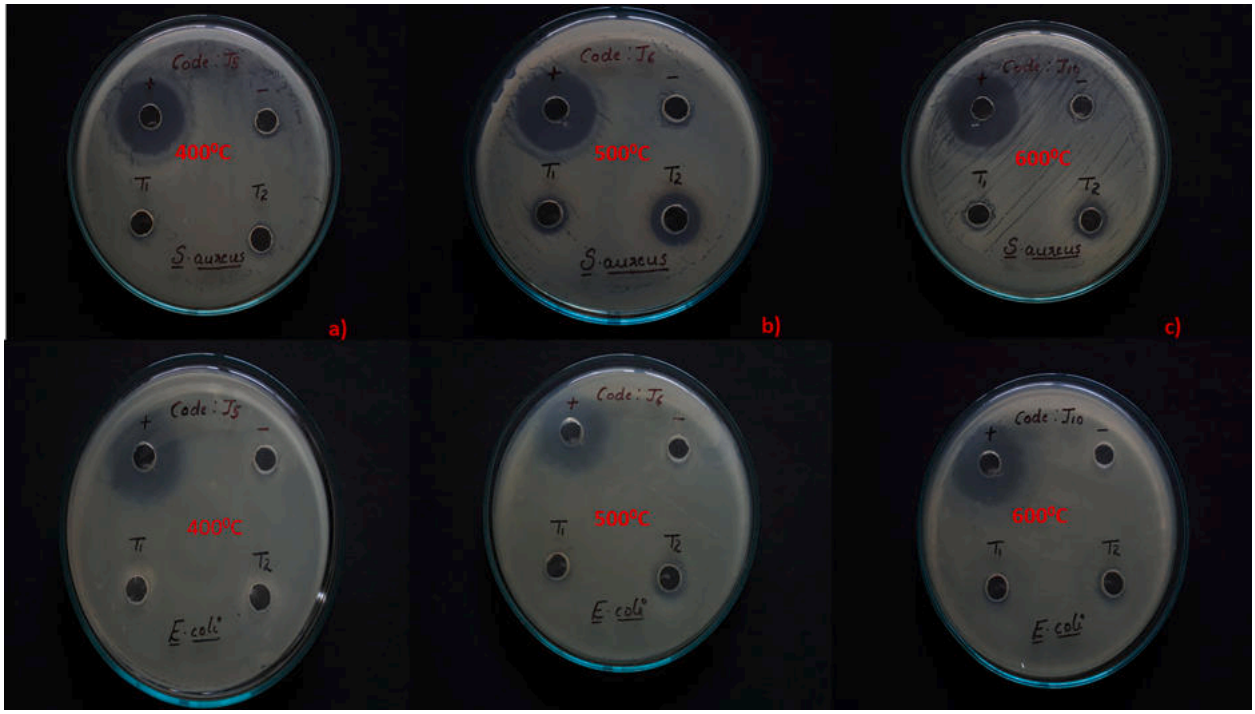

Fig. 15. Antibacterial activity of Activated carbon (400 °C, 500 °C and 600 °C).

production of agglomerated and irregular-shaped nanoparticles was shown by SEM and TEM. The optical absorption occurs at 249 nm in the UV spectrum. At different annealing temperatures, the energy band gap of activated carbon is 2.04 eV, 2.00 eV, and 1.97 eV (400 °C, 500 °C, and 600 °C), respectively. Under visible light irradiation, the greatest photocatalyticdegradations for MB was recorded at 94 percent. As itself, activated carbon has strong antibacterial action. According to the findings, the generated activated carbon material is very suitable for wastewater treatment and environmental applications. The Nyquist plot's smaller arc radius verifies the efficient separation of photogenerated electron and hole pairs. The reusability investigations reveal that AC still display remarkable photostability and degradation efficiency even after four cycles. It is firmly believed that the prepared AC may serve as a potential photocatalyst for environmental remediation in the near future because they exhibit excellent photocatalytic performance even in their pristine form due to small crystallite size, high sunlight absorption, effective separation of charge carriers for a longer period of time, and high reduction and oxidation ability.

CRediT authorship contribution statement

M.Amalanathan: Supervision. **M. Aravind:** Synthesis, Manuscript Writing, Review, Conceptualizaion, Data curation. **M. Sony Michael Mary:** Formal analysis. **Nafis Ahmed:** Resources. **P. Velusamy:** Validation. **Kumari Subitha T:** Writing help. **Raazia Noreen:** Investigation. **Shafaqat Ali:** Investigtion.

Declaration of Competing Interest

The authors declare that they have no known competing financial interests or personal relationships that could have appeared to influence the work reported in this paper.

Data availability

Data will be made available on request.

Acknowledgement

The authors thank SSN college of Engineering and National Engineering College for providing lab facilities to complete the project.

References

[1] M. Aravind, A. Ahmad, I. Ahmad, M. Amalanathan, K. Naseem, S.M.M. Mary, C. Parvathiraja, S. Hussain, T.S. Algarni, M. Pervaiz, M. Zuber, Critical green routing synthesis of silver NPs using jasmine flower extract for biological activities and photocatalytical degradation of methyleneblue, J. Environ. Chem. Eng. 9 (1) (2021) 104877, https://doi.org/10.1016/j.jece:2020.104877.

[2] M. Aravind, M. Amalanathan, M. Mary, Synthesis of TiO_2 nanoparticles by chemical and green synthesis methods and their multifaceted properties, SN Appl. Sci. 3 (4) (2021) 1–10.

[3] T. Ahmad, M. Rafatullah, A. Ghazali, O. Sulaiman, R. Hashim, Oil palm biomass–Based adsorbents for the removal of water pollutants—A review, J. Environ. Sci. Health, Part C 29 (3) (2011) 177–222.

[4] R. Sharma, M. Almási, S.P. Nehra, V.S. Rao, P. Panchal, D.R. Paul, I.P. Jain, A. Sharma, Photocatalytic hydrogen production using graphitic carbon nitride (GCN): A precise review, Renew. Sustain. Energy Rev. 168 (2022) 112776, https://doi.org/10.1016/j.rser.2022.112776.

[5] V. Benedetti, F. Patuzzi, M. Baratieri, Characterization of char from biomass gasification and its similarities with activated carbon in adsorption applications, Appl. Energy 227 (2018) 92–99.

[6] M. Aravind, M. Amalanathan, M.S.M. Mary, C. Parvathiraja, A.A. Alothman, S. M. Wabaidur, M.A. Islam, Enhanced photocatalytic and biological observations of green synthesized activated carbon, activated carbon doped silver and activated carbon/silver/titanium dioxide nanocomposites, J. Inorg. Organomet. Polym Mater. 32 (1) (2022) 267–279.

[7] Y. Ma, Comparison of activated carbons prepared from wheat straw via $ZnCl_2$ and KOH activation, Waste and biomass valorization 8 (3) (2017) 549–559.

[8] Y. Chen, Q. Chen, H. Zhao, J. Dang, R. Jin, W. Zhao, Y. Li, Wheat straws and corn straws as adsorbents for the removal of Cr (VI) and Cr (III) from aqueous solution: kinetics, isotherm, and mechanism, ACS Omega 5 (11) (2020) 6003–6009.

[9] K. Lewicka, Activated carbons prepared from hazelnut shells, walnut shells and peanut shells for high CO_2 adsorption, Polish J. Chem. Technol., 19(2), 2017.

[10] M. Aravind, M. Amalanathan, Structural, morphological, and optical properties of country egg shell derived activated carbon for dye removal, Mater. Today:. Proc. 43 (2021) 1491–1495.

[11] F. Gao, X. Tang, H. Yi, B. Zhang, S. Zhao, J. Wang, T. Gu, Y. Wang, NiOmodified coconut shell based activated carbon pre-treated with KOH for the high efficiency adsorption of NO at ambient temperature, Ind. Eng. Chem. Res. 57 (49) (2018) 16593–16603.

[12] L. Zhang, J. Tan, G. Xing, X. Dou, X. Guo, Cotton stalk-derived hydrothermal carbon for methylene blue dye removal: investigation of the raw material plant tissues, Bioresources and Bioprocessing 8 (1) (2021) 1–11.

[13] N.U.M. Nizam, M.M. Hanafiah, E. Mahmoudi, A.A. Halim, A.W. Mohammad, The removal of anionic and cationic dyes from an aqueous solution using biomass-based activated carbon, Sci. Rep. 11 (1) (2021) 1–17.

[14] X. Chen, L. Yu, S. Zou, L. Xiao, J. Fan, Zeolite cotton in tube: A simple robust household water treatment filter for heavy metal removal, Sci. Rep. 10 (1) (2020) 1–9.

[15] H.B.M. Emrooz, M. Maleki, A. Rashidi, M. Shokouhimehr, Biomass Convers. Biorefinery. 1–12 (2020).

[16] Y. Zhang, J. Xu, B. Li, Z. Xie, X. Li, J. Tang, S. Fan, Enhanced adsorption performance of tetracycline in aqueous solutions by KOH-modified peanut shell-derived biochar, Biomass Conversion and Biorefinery (2021) 1–15.

[17] S. Haj Yahia, K.K. Lee, B. Ayed, N. Hedin, T.L. Church, Activated carbons from Hydrochars prepared in Milk, Sci. Rep. 9 (1) (2019) 1–11.

[18] C. Parvathiraja, S. Shailajha, S. Shanavas, J. Gurung, Biosynthesis of silver nanoparticles by Cyperuspangorei and its potential in structural, optical and catalytic dye degradation, Applied Nanoscience 11 (2) (2021) 477–491.

[19] D. Rattan Paul, S.P. Nehra, Graphitic carbon nitride: a sustainable photocatalyst for organic pollutant degradation and antibacterial applications, Environ. Sci. Pollut. Res. 28 (4) (2021) 3888–3896.

[20] E. Martínez-Periñán, C.W. Foster, M.P. Down, Y. Zhang, X. Ji, E. Lorenzo, C. E. Banks, Graphene encapsulated silicon carbide nanocomposites for high and low power energy storage applications, C 3 (2) (2017) 20.

[21] M. Goswami, N.C. Adhikary, S. Bhattacharjee, Effect of annealing temperatures on the structural and optical properties of zinc oxide nanoparticles prepared by chemical precipitation method, Optik 158 (2018) 1006–1015.

[22] D. Vikraman, I. Rabani, S. Hussain, K. Sundaram, S. Ramesh, H.S. Kim, H.S. Kim, Mixed- phase MoS2 decorated reduced graphene oxide hybrid composites for efficient symmetric supercapacitors, Int. J. Energy Res. 45 (6) (2021) 9193–9209.

[23] T.H.A. Corrêa, J.N.F. Holanda, Calcium pyrophosphate powder derived from avian eggshell waste, Cerâmica 62 (363) (2016) 278–280.

[24] K. Salma, N. Borodajenko, A. Plata, L. Berzina-Cimdina, A. Stunda, Fourier transform infrared spectra of technologically modified calcium phosphates. In 14th Nordic-Baltic conference on biomedical engineering and medical physics (pp. 68-369 71). Springer, Berlin, Heidelberg, 2008.

[25] J. Ram, R.G. Singh, R. Gupta, V. Kumar, F. Singh, R. Kumar, Effect of annealing on the surface morphology, optical and structural properties of nanodimensional tungsten oxide prepared by coprecipitation technique, Journal of ElectronicMaterials 48 (2) (2019) 1174–1183.

[26] G.N. Narayanan, R. Sankar Ganesh, A. Karthigeyan, Effect of annealing temperature on structural, optical and electrical properties of hydrothermal assisted zinc oxide nanorods, Thin Solid Films 598 (2016) 39–45.

[27] K.V. Rao, G. Kishore, K.S. Rao, K.N.K. Vani, M.N. Rao, Y.H. Rao, X-ray photoelectron spectroscopy studies on activated carbon prepared from rind of Citrus nobilis, Asian J. Chem. 22 (6) (2010) 4377–4381.

[28] V.K. Palaniswamy, B. Ramasamy, K. Manoharan, K. Raman, R. Sundaram, Enhanced photocatalytic degradation of tetracycline antibiotic using m-$BiVO_4$photocatalyst under visible light irradiation, Chem. Phys. Lett. 771 (2021), 138531.

[29] D.R. Paul, R. Sharma, P. Panchal, S.P. Nehra, A.P. Gupta, A. Sharma, Synthesis, characterization and application of silver doped graphitic carbon nitride as photocatalyst towards visible light photocatalytic hydrogen evolution, Int. J. Hydrogen Energy 45 (44) (2020) 23937–23946.

[30] D.R. Paul, S. Gautam, P. Panchal, S.P. Nehra, P. Choudhary, A. Sharma, ZnO-modified g-C3N4: a potential photocatalyst for environmental application, ACS Omega 5 (8) (2020) 3828–3838.

[31] J. Schneider, M. Matsuoka, M. Takeuchi, J. Zhang, Y.u. Horiuchi, M. Anpo, D. W. Bahnemann, Understanding TiO_2 photocatalysis: mechanisms and materials, Chem. Rev. 114 (19) (2014) 9919–9986.

[32] H. Yamashita, Y. Ichihashi, M. Takeuchi, S. Kishiguchi, M. Anpo, Characterization of metal ion-implanted titanium oxide photocatalysts operating under visible light irradiation, J. Synchrotron Radiation 6 (3) (1999) 451–452.

[33] E.I. García-López, G. Marcì, Preparation of photocatalysts by physical methodologies, in: Materials Science in Photocatalysis, Elsevier, 2021, pp. 37–62.

[34] B. Neppolian, D.R. Eddy, S. Sakai, Y. Okada, H. Nishijima, M. Anpo, Preparation of TiO_2 nano-particle photocatalysts by a multi-gelation method: the effect of pH change, Res. Chem. Intermed. 34 (1) (2008) 103–111.

[35] R. Benisha, M. Amalanathan, M. Aravind, M.S.M. Mary, A. Ahmad, S. Tabassum, I. Ahmad, Catharanthusroseus leaf extract mediated Ag-MgO nanocatalyst for photocatalytic degradation of Congo red dye and their antibacterial activity, J. Mol. Struct. 1262 (2022), 133005.

[36] S. Moosavi, R.Y.M. Li, C.W. Lai, Y. Yusof, S. Gan, O. Akbarzadeh, Z.Z. Chowhury, X.-G. Yue, M.R. Johan, Methylene blue dye photocatalytic degradation over synthesised Fe_3O_4/AC/TiO_2 nano-catalyst: degradation and reusability studies, Nanomaterials 10 (12) (2020) 2360, https://doi.org/10.3390/nano10122360.

[37] A. Maddu, R. Meliafatmah, E. Rustami, Enhancing Photocatalytic Degradation of Methylene Blue Using ZnO/Carbon Dots Nanocomposite Derived From Coffee Grounds, Polish J. Environ. Stud. 30 (1) (2021).

[38] D. Saramas, S. Ekgasit, Nano-zinc oxide-doped activated carbon from popped rice and its application for feed additive, Eng. J. 25 (3) (2021) 41–50.

[39] A. Ahmad, D. Jini, M. Aravind, C. Parvathiraja, R. Ali, M.Z. Kiyani, A. Alothman, A novel study on synthesis of egg shell based activated carbon for degradation of methylene blue via photocatalysis, Arabian J. Chem. 13 (12) (2020) 8717–8722.

[40] L.u. Luo, X.i. Wu, Z. Li, Y. Zhou, T. Chen, M. Fan, W. Zhao, Synthesis of activated carbon from biowaste of fir bark for methylene blue removal, R. Soc. Open Sci. 6 (9) (2019) 190523, https://doi.org/10.1098/rsos.190523.

[41] M. Mahanthappa, N. Kottam, S. Yellappa, Enhanced photocatalytic degradation of methylene blue dye using CuSCdS nanocomposite under visible light irradiation, Appl. Surf. Sci. 475 (2019) 828–838.

[42] R. Bomila, S. Srinivasan, S. Gunasekaran, A. Manikandan, Enhanced photocatalytic degradation of methylene blue dye, opto-magnetic and antibacterial behaviour of pure and La-doped ZnO nanoparticles, J. Supercond. Novel Magn. 31 (3) (2018) 855–864.

[43] V.K. Palanisamy, K. Manoharan, K. Raman, R. Sundaram, Efficient sunlight-driven photocatalytic behavior of zinc sulfide nanorods towards Rose Bengal degradation, J. Mater. Sci.: Mater. Electron. 31 (17) (2020) 14795–14809.

[44] S. Kaur, S. Sharma, A. Umar, S. Singh, S.K. Mehta, S.K. Kansal, Solar light driven enhanced photocatalytic degradation of brilliant green dye based on ZnS quantum dots, Superlattices and Microstructures 103 (2017) 365–375.

[45] D. Ayodhya, G. Veerabhadram, Facile fabrication, characterization and efficient photocatalytic activity of surfactant free ZnS, CdS and CuS nanoparticles, J. Sci.: Adv. Mater. Devices 4 (3) (2019) 381–391.

[46] N. Venkatesh, K. Sabarish, G. Murugadoss, R. Thangamuthu, P. Sakthivel, Visible light–driven photocatalytic dye degradation under natural sunlight using Sn-doped CdS nanoparticles, Environ. Sci. Pollut. Res. 27 (34) (2020) 43212–43222.

[47] N. Qutub, P. Singh, S. Sabir, S. Sagadevan, W.C. Oh, Enhanced photocatalytic degradation of Acid Blue dye using CdS/TiO2 nanocomposite, Sci. Rep. 12 (1) (2022) 1–18.

[48] P. Raizada, P. Singh, A. Kumar, G. Sharma, B. Pare, S.B. Jonnalagadda, P. Thakur, Solar photocatalytic activity of nano-ZnO supported on activated carbon or brick grain particles: role of adsorption in dye degradation, Appl. Catal. A 486 (2014) 159–169.

[49] M.A. Abu-Dalo, S.A. Al-Rosan, B.A. Albiss, Photocatalytic degradation of methylene blue using polymeric membranes based on cellulose acetate impregnated with ZnO nanostructures, Polymers 13 (19) (2021) 3451.

[50] M.S. Elsayed, I.A. Ahmed, D.M. Bader, A.F. Hassan, Green Synthesis of Nano Zinc Oxide/Nanohydroxyapatite Composites Using Date Palm Pits Extract and Eggshells: Adsorption and Photocatalytic Degradation of Methylene Blue, Nanomaterials 12 (1) (2021) 49.

[51] Y. Liu, Q. Zhu, M. Tayyab, L. Zhou, J. Lei, J. Zhang, Single-Atom Pt Loaded Zinc Vacancies ZnO–ZnS Induced Type-V Electron Transport for Efficiency Photocatalytic H2 Evolution, Solar Rrl 5 (11) (2021) 2100536.

[52] S. Azizi, R. Mohamad, A. Bahadoran, S. Bayat, R.A. Rahim, A. Ariff, W.Z. Saad, Effect of annealing temperature on antimicrobial and structural properties of bio-synthesized zinc oxide nanoparticles using flower extract of Anchusaitalica, J. Photochem. Photobiol., B 161 (2016) 441–449.

[53] V. Poornima Parvathi, M. Umadevi, R. Sasikala, R. Parimaladevi, V. Ragavendran, J. Mayandi, G.V. Sathe, Novel silver nanoparticles/activated carbon co doped titania nanoparticles for enhanced antibacterial activity, Mater. Lett. 258 (2020) 126775, https://doi.org/10.1016/j.matlet.2019.126775.

[54] A. Gibała, P. Żeliszewska, T. Gosiewski, A. Krawczyk, D. Duraczyńska, J. Szaleniec, M. Szaleniec, M. Oćwieja, Antibacterial and antifungal properties of silver nanoparticles—Effect of a surface-stabilizing agent, Biomolecules 11 (10) (2021) 1481, https://doi.org/10.3390/biom11101481.

[55] P. Panchal, D.R. Paul, A. Sharma, P. Choudhary, P. Meena, S.P. Nehra, Biogenic mediated Ag/ZnO nanocomposites for photocatalytic and antibacterial activities towards disinfection of water, J. Colloid Interface Sci. 563 (2020) 370–380.

[56] A. Hajimohammad, L. Fozouni, Antibacterial Effect of Zinc Oxide Nanoparticles on Mupirocin-Resistant Staphylococcus aureus Isolated from Nasal Carriers, Int. J. Basic Sci. Med. 3 (2) (2018) 78–82.

[57] E.K. Zarrindokht, C. Pegah, Antibacterial activity of ZnO nanoparticle on gram-positive and gram-negative bacteria, Afric. J. Microbiol. Res. 5 (12) (2011) 1368–1373.

[58] F. Yusof, S. Chowdhury, N. Sulaiman, M.O. Faruck, Effect of process parameters on the synthesis of silver nanoparticles and its effects on microbes, Jurnal Teknologi 80 (3) (2018).

[59] D. Paredes, C. Ortiz, R. Torres, Synthesis, characterization, and evaluation of antibacterial effect of Ag nanoparticles against Escherichia coli O157: H7 and methicillin-resistant Staphylococcus aureus (MRSA), Int. J. Nanomed. 9 (2014) 1717.

[60] Y.Y. Loo, Y. Rukayadi, M.A.R. Nor-Khaizura, C.H. Kuan, B.W. Chieng, M. Nishibuchi, S. Radu, In vitro antimicrobial activity of green synthesized silver nanoparticles against selected gram-negative foodborne pathogens, Front. Microbiol. 9 (2018) 1555.

[61] O.T. Osuntokun, T.A. Jemilaiye, A.M. Yusuf-Babatunde, Synergistic Bioactivity of Activated Carbon (Charcoal), Anogeissus Leiocarpus and Nauclea Latifolia on Selected Clinical Isolates.

Chemosphere 321 (2023) 138077

Contents lists available at ScienceDirect

Chemosphere

journal homepage: www.elsevier.com/locate/chemosphere

Hydrothermally synthesized Ag-TiO_2 nanofibers (NFs) for photocatalytic dye degradation and antibacterial activity

M. Aravind [a,*], M. Amalanathan [b], Sadia Aslam [c], Arsh E Noor [d], D. Jini [b], Saadat Majeed [e], P. Velusamy [f], Asma A. Alothman [g], Razan A. Alshgari [g], Mohammed Sheikh Saleh Mushab [g], Mika Sillanpaa [h]

[a] Department of Physics, National Engineering College, K.R Nagar, Kovilpatti, 628503, Tamilnadu, India
[b] Department of Physics, Nanjil Catholic College of Arts and Science, Kaliyakkavilai, Tamilnadu, India
[c] Department of Botany, Government College University Faisalabad, Pakistan
[d] Department of Environmental Science and Engineering, Government College University Faisalabad, Pakistan
[e] Institute of Chemical Sciences, Bahauddin Zakariya University, Multan, 60800, Pakistan
[f] Department of Physics, Thiagarajar College of Engineering, Madurai, Tamilnadu, India
[g] Department of Chemistry, College of Science, King Saud University, Riyadh, 11451, Saudi Arabia
[h] Department of Biological and Chemical Engineering, Aarhus University, Norrebrogade 44, 17 8000, Denmark

HIGHLIGHTS

- Ag nanoparticles modified with TiO2 nanofibers was synthesized by the hydrothermal method.
- TheAg-TiO2 Nanofiber achieved high photocatalytic performance toward the removal of Methylene blue.
- The Ag–TiO2 Nanofibers displayed the attractive antibacterial efficacy against both gram positive and gram negative bacteria.
- The Ag–TiO2 nanofibers are suitable for waste water treatment and biomedical applications.

GRAPHICAL ABSTRACT

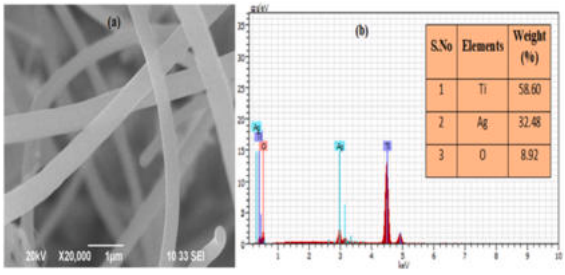

ARTICLE INFO

Handling Editor: Muhammad Mubashir

Keywords:
Hydrothermal method
Methylene blue
Photodegradation
Antibacterial
Visible light irradiations.

ABSTRACT

This work successfully utilised eco-friendly green synthesis to produce Ag–TiO_2 nanofibers (NFs). As pollution and energy limitations have become global issues, there is an ongoing need to develop more effective catalysts through straightforward and environmentally friendly methods. The Ag–TiO_2 nanofibers (NFs) XRD pattern exhibits an anatase TiO_2 and FCC crystal structure of Ag nanoparticles. The SEM investigation revealed a nanofiber-like surface morphology. The Ag–TiO_2 nanofibers (NFs) exhibits an optical band gap energy is 2.5 eV. Methylene blue (MB), malachite green (MG), Congo red (CR), and crystal violet (CV) dye aqueous solutions were used to evaluate the photocatalytic performance of the synthesized Ag-modified TiO_2 nanofibers (NFs) under direct sunlight irradiation. The effects of catalyst size on the efficient breakdown of MB dye were also investigated. The optimum catalyst concentration was found to be at 0.02 mg/mL. At 120 min of direct sunlight, the highest photosynthetic degradation efficiency (DE percentage) of 94% was achieved for MB dye. Ag–TiO_2 nanofibers (NFs) have been demonstrated to have exceptional antibacterial activity against Gram-positive bacteria such as *Staphylococcus aureus* and Gram-negative bacteria *E-Coli*. Because of these great qualities, it seems

* Corresponding author.
E-mail address: aravinthajinm@gmail.com (M. Aravind).

https://doi.org/10.1016/j.chemosphere.2023.138077
Received 29 October 2022; Received in revised form 10 January 2023; Accepted 5 February 2023
Available online 7 February 2023

likely that the Ag–TiO_2 nanofibers (NFs) made could be a great photocatalyst for getting dye pollutants out of wastewater.

1. Introduction

In recent years the most important challenges facing humanity now are the scarcity of clean water, growing population and pollution of existing water sources. There is a correlation between pesticides and other organic dyes in water sources and the transmission of water-borne diseases. A significant and widespread negative influence on the water supply is caused by impurities such as plastics, textiles, electronic trash, and industrial wastes. In recent years, addressing environmental issues resulting from huge releases of toxic substances has become a vital priority for the scientific community. Dye pollutants are exceedingly difficult to remove from wastewater. MB is a negative polar dye frequently employed in textile and artwork printing and painting. The negative effects of methylene blue are headaches, nausea, vertigo, and skin discolouration. Numerous technologies, including adsorption Liu et al. (2020), the biological process Javaid et al. (2011), membrane filtration Kurt et al. (2012), improved oxidation Yasar et al. (2013), and other physical and chemical processes, have been utilised to eliminate hazardous colours from wastewater. These procedures have the drawbacks of high temperatures, high pressure, energy consumption, and a longer time frame. Due to issues with effluent, sludge formation, and adsorbent repair, none of these approaches is superior for dye degradation. When dye molecules are exposed to sunlight they break down into carbon dioxide, water molecules, and simple mineral acids Priyanka and Lens (2022). Therefore, heterogeneous photocatalysis paves the way for an eco-friendly, cost-effective, and effective method of environmental clean-up (Thakur et al., 2020; Roongraung et al., 2020a,b).

Gaurav K. Upadhyay et al. (2019) synthesized that ZnO: TiO_2 nanocomposite for removing methylene blue. The optical bandgap of the ZnO: TiO_2 nanocomposites has decreased from 3.30 eV to 3.10 eV. After 120 min, the ZnO-modified TiO_2 nanocomposite degrades at its fastest rate, between 75 and 90%. Moradi et al. (2018) reported that under UV irradiation, the magnetic $NiFeO_4$@ZnO nanocomposite degrades direct blue dyes and reactive blue dyes. $NiFeO_4$@ZnO nanocomposites degrades natural blue dyes and reactive blue dyes by 98.5% and 96.5%, respectively. Mukhopadhyay et al. (2016) synthesized that plasmonic Au-coated ZnO/TiO_2 catalysts completely degrades under CR and MB under UV light irradiation. According to Aqeel et al. (2020) sol-gel process was used to prepare the nano photocatalyst Zr/Ag/TiO_2. Zr/Ag/TiO_2 nanocomposites have 93% dye degradation efficiency. Santos et al. (2015) used a hydrothermal technique to prepare Ag/TiO_2 nanocomposite to decolourize tartrate azo dye. According to Kumar et al. (2020) the photocatalytic activity of the Ag/TiO_2 composites degrades 78 percent of methyl orange dye after 180 min.

Noble metal nanoparticles have strong Surface Plasmon Resonance (SPR) properties and a high electron trapping capacity. In the present research work aims to synthesis and analyse Ag–TiO_2 nanofibers (NFs) for the effective photodegradation of Methylene blue (MB), malachite green (MG), Congo red (CR), and crystal violet (CV) dye aqueous dye solution under solar irradiation. Ag–TiO_2 nanofibers (NFs) may be able to absorb UV and visible light from the sun and attract additional dye molecules to the surface, which is a good way to break down organic dyes. The most important factors for enhancing photocatalytic activity are metal ions dopants (Cu, Co, Ag, Au), composite networks, and the different kinds of light sources used (UV/Visible or sunlight). Metal doping can reduce charge carrier recombination and improve photocatalyst visible light absorption based on ZnO and TiO_2.

2. Materials and methods

2.1. Materials

The ingredients Titanium Tetra Isopropoxide (TTIP), Silver nitrate ($AgNO_3$), and Methylene blue ($C_{16}H_{18}ClN_3S$) were purchased from Sigma Aldrich. Without any additional purification, all chemicals and reagents are used.

2.2. Synthesis of Ag–TiO_2 nanofibers (NFs)

Ag–TiO_2 nanofibers (NFs) were synthesized by employing a simple and environmentally friendly hydrothermal method Aravind et al. (2021). After adding 10 mL of titanium tetra-isopropoxide (TTIP) to a beaker with a capacity of 100 mL, the next step was to add 5 mL of jasmine flower extract and 20 mL of distilled water. The solution was constantly stirred at a pace of 400 revolutions per minute (rpm). The titanium solution should now have added 0.1 M of an $AgNO_3$ solution. The solution was kept warm in an autoclave made of stainless steel and heated for one day in a muffle furnace at a temperature of 180 °C. Calcination took place for 6 h at a temperature of 500 °C Wang et al. (2020).

2.3. Characterizations of Ag–TiO_2 nanofibers (NFs)

The Panalytical X-Pert Pro diffractometer was used to measure powder X-ray diffraction. The Shimadzu Prestige 20 IR-Spectrophotometer was used to record the FT-IR spectrum with an area of 400–4000 cm^{-1}. Scanning Electron Microscopes with Energy Dispersive X-Ray Spectroscopy (Jeol JSM 6390 and Quintox KM9106) were used to analyse surface micro-morphology and their elemental analysis. A Jasco V630 UV–Visible Spectrophotometer was used to measure UV–visible absorbance spectra. Dielectric measurements were made with a CHI604E electrochemical analyser and a Hioki LCR impedance analyser.

2.4. Photocatalytic measurement

The degradation of MB aqueous dye in visible light was investigated. The Ag–TiO_2 nanofibers (NFs) were distributed in a 100 mL aqueous MB dye. So that adsorption and desorption may occur properly before irradiation can take place. The solution was ultrasonically agitated for 60 min inside a dark room. Every 30 min, 5 mL of solution was collected and centrifuged at 3000 rpm for 10 min. The temperature of the reaction mixture was kept constant at 37 °C. The photodegradation behavior was evaluated using a UV–Vis analyser. Similarly, different quantities of catalysis (0.005 mg–0.02 mg) of Ag–TiO_2 were used to assess the catalytic effectiveness of the samples. The following equation is used to determine the degradation efficiency (DE) of dye.

$$\text{Degradation Efficiency } (\%) = (C_o - C) \ / \ C_o \times 100\ \% \quad (1)$$

where C_o – Initial concentration of dye solution.

C – Final concentration of dye solution Ahmad et al. (2020).

2.5. Antibacterial properties

The antibacterial properties of Ag–TiO_2 nanofibers (NFs) were investigated using disc diffusion. The antibacterial activity of Ag–TiO_2 nanofibers (NFs) was examined using gram-positive (*S. aureus*) and gram-negative (*E. coli*) bacterial pathogens Wong et al. (2020). 8 (milli

meters) mm wells were punched in Mueller Hinton Agar (MHA) and wiped with positive and negative strains. In each well was poured a solution of prepared Ag–TiO_2 nanofibers (NFs) of varying concentrations. The agar plate was incubated for 24 h at 37 °C. The inhibitory layer was measured in millimetres Rao et al. (2019).

3. Results and discussion

3.1. XRD analysis

Fig. 1 a) Demonstrates the XRD pattern of Ag–TiO_2 nanofibers (NFs). The Braggs reflection planes (101), (110), (004), (111), (102), (200), (105), (211), (204), (220), and (116) correspond to the diffraction peaks 2(θ) at 25.56°, 27.48°, 36.17°, 38.28°, 41.36°, 48.37°, 54.54°, 56.92°, 62.81°, 64.35°, and 69.20°. The diffraction peaks measured at 38.28°, 48.37°, and 64.35° correlates to the FCC crystal structure of Ag–TiO_2 nanoparticles. The detected XRD peaks precisely matched with the JCPDS card numbers 07–6173 and 04–0774 Roongraung et al. (2020). The average crystallite size of Ag–TiO_2 nanofibers (NFs) is 33 nm (nm). In the XRD pattern of Ag–TiO_2 nanofibers, dual phases consisting of a tetragonal anatase phase and a face-centred cubic lattice of silver nanoparticles are seen. The Ag nanoparticles couldn't get into the TiO_2 crystal lattice, so they gathered on its surface.

3.2. UV–visible absorbance spectroscopy

Fig. 1 (c and d) depicts the UV–visible and Tauc plots of Ag modified TiO_2 nanofibers (NFs). The Ag modified TiO_2 nanofibers reveals the absorbance peak reaching between 208 and 396 nm (NFs) Liang et al. (2022). The redshift is triggered by the presence of Ag-nanoparticles on the surface of the TiO_2 nanostructure. Because of the localized SPR effect, the plasmonic Ag nanoparticles in the TiO_2 catalyst may easily absorb light and excite the surface electron for transmission to an acceptor Li et al. (2018). The Tauc plot was used to obtain the optical band gap values,

$$h\nu = A\left(h\nu - E_g\right)^n / \alpha \quad (2)$$

where α is the optical absorption coefficient, E_g is the bandgap energy, A is an optical constant, and n indicates the transition order Arifin et al. (2022). The optical band gap values of the Ag–TiO_2 nanofibers (NFs) determined are 2.5 eV. While Ag nanoparticles have been added on the surface of TiO_2 nanoparticles, compared to commercial TiO_2 nanoparticles, the bandgap gradually decreases. When Ag nanoparticles are present on the surface of the TiO_2 nanostructure, a huge quantity of photons with a longer wavelength are absorbed. It makes photocatalysis work better. Electrons are excited from the VB (valance band) to the CB (conduction band) and subsequently shifted to the Ag fermi level. UV spectra result in a decreased photoelectron carrier recombination rate Shen et al. (2022).

3.3. Fourier transform –infra red (FT-IR) spectroscopy

Fig. 1 b) shows the vibrational spectra of as-prepared Ag–TiO_2 nanofibers (NFs) using jasmine flower extract. The band obtained at

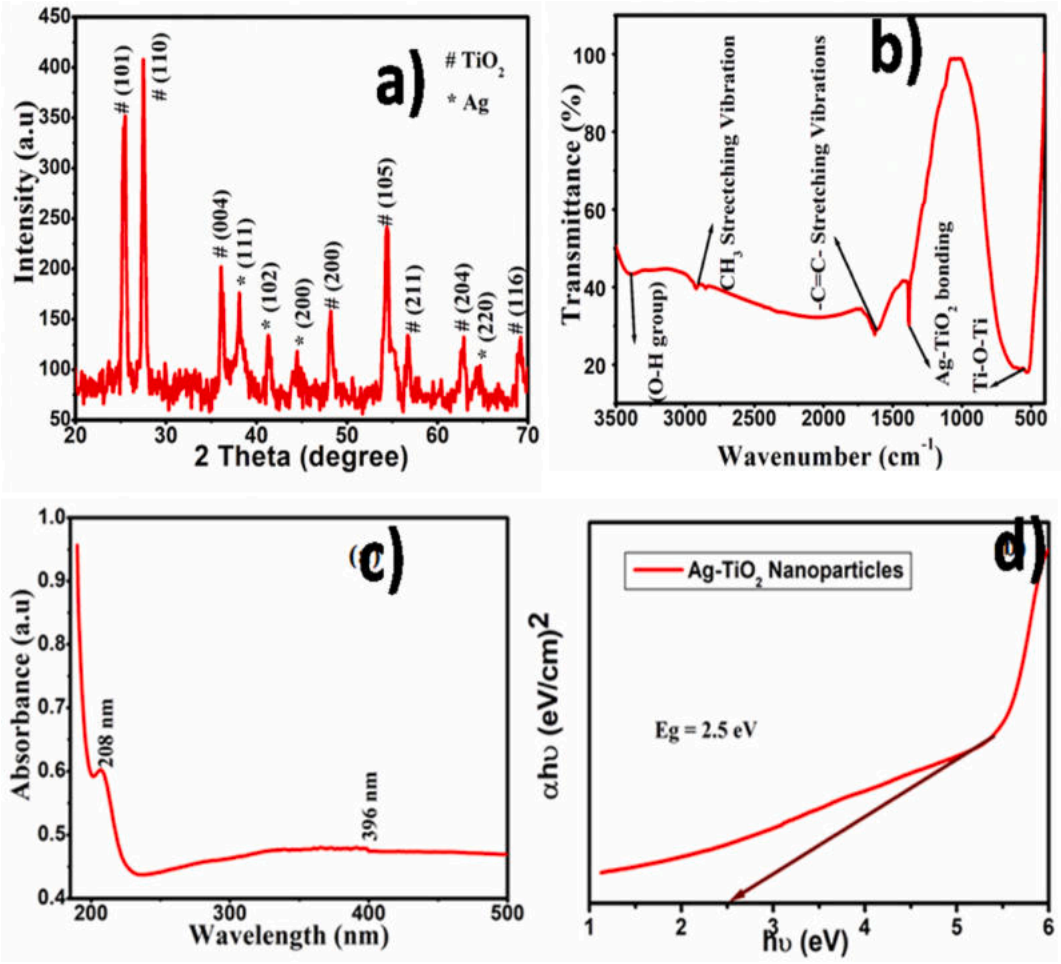

Fig. 1. a) XRD pattern of Ag–TiO_2 nanofibers (NFs), b) FT-IR spectra of Ag–TiO_2 nanofibers (NFs) using jasmine flower extract (c and d) UV–visible absorbance spectra and Tauc Plot of Ag–TiO_2 nanofibers (NFs).

3385.3 cm^{-1} denotes the hydroxyl (O–H) groups Zhang et al. (2012). The peak at 2851 cm^{-1} corresponds to the – CH_3 stretching mode of vibration Ashraf et al. (2020). The – C = C - aromatic stretching vibrations band obtained at 1631.30 cm^{-1} Jaber et al. (2020). The band observed at 1355 cm^{-1} represents the Ag–TiO bond. The signal at 1355 cm^{-1} supports silver NPs deposition on the surface of TiO_2 NFs. The Ti–O–Ti vibrations in Ti are seen by the 528 cm^{-1} peak Carvalho et al. (2018).

3.4. Scanning electron microscope with elemental dispersive analysis X-ray spectrum

Fig. 2 (a and b) display the SEM and EDAX images of the Ag–TiO_2 nanofibers (NFs) respectively. The surface morphology demonstrates that a vast number of nanofibers made of TiO_2 are regularly aligned Kang et al. (2019). When Ag nanoparticles are decorated on the surface of the nano-structured TiO_2 nanofibers results in the size and form of the composites may be controlled to a certain extent. The EDAX spectrum of Ag–TiO_2 nanofibers (NFs) reveals the presence of key components, including silver, titanium, and oxygen.

3.5. Photocatalytic performance

3.5.1. Mechanism of photodegradation of dye molecules

The photocatalytic dye degradation of Methylene Blue is shown in Fig. 3. When sunlight falls on the surface of Ag–TiO_2 NFs, photoelectrons (e^-) may be excited from the valance band to the conduction band by leaving holes (h^+) in the Valance band. Photo generated e^- and h^+ migrated to the Ag–TiO_2 nanofibers (NFs) surface, preventing electron hole pair recombination. However, because Ag has a higher fermi energy level than TiO_2, electrons move from Ag to TiO_2. When light (visible) is irradiated on the surface of Ag–TiO_2 nanofibers (NFs), the Schottky barrier effect mechanism causes Ag and TiO_2 to form new F_e (Fermi energy) levels and change some values, resulting in improved photocatalytic activity. Water molecules infiltrate the gaps in the valance band, allowing hydroxyl radicals ($^{\bullet}OH$) and hydrogen ions (H^+) to get through. Superoxides ($O_2^{\bullet}$) are formed when photo generated electrons absorb dissolved oxygen. Reactive hydroxyl groups and superoxide react with aqueous solutions to produce CO_2 and H_2O as by-products Kang et al. (2019).

$$\text{Ag–TiO}_2\text{ nanofibers (NFs)} + hv \rightarrow e- + h+ \quad (3)$$

$$h+ + H_2O \rightarrow {}^{\bullet}OH + H^+ \quad (4)$$

$$O_2 + e\text{-} \rightarrow O_2^{-} \quad (5)$$

$$O_2- + H^+ \rightarrow {}^{\bullet}HO_2 \quad (6)$$

$$2{}^{\bullet}HO_2 \rightarrow H_2O_2 + 1O_2\text{ (Singlet oxygen)} \quad (7)$$

$$H_2O_2 + e- \rightarrow {}^{\bullet}OH + OH^- \quad (8)$$

$${}^{\bullet}OH + H^+ + \text{MB dye} \rightarrow CO_2 + H_2O \quad (9)$$

The accumulation of noble metal (Ag) nanoparticles to the surface of a TiO_2 catalyst prevents the trapping of electron hole pairs and decreases the rate of electron-hole pair recombination. Due to the SPR effect, the incorporation of silver nanoparticles increases the visible light absorption capability of TiO_2 nanoparticles and their catalytic activity Chen et al. (2012). TiO_2 is one of the most effective photocatalysts for removing persistent contaminants such as organic dyes, medicinal chemicals, bacteria, and viruses. The rapid recombination of charge carriers and the inefficient utilisation of light remain significant hurdles to its broad application. By altering the TiO_2 lattice with the noble metal silver, it is possible to enhance the catalytic performance of TiO_2 and shift its photocatalytic response to the UV to the visible light spectrum.

3.5.2. Effect of catalyst

The impact of the initial photocatalyst concentration was investigated by increasing the initial Ag–TiO_2 nanofibers (NFs) concentration from 0.005 mg to 0.02 mg per 100 ml in MB dye solution, which can be seen in Fig. 3 (a). When the amount of photoactive catalyst was increased from 0.005 to 0.02 mg, the photocatalytic activity increased, perhaps due to an increase in the active sites on the catalyst surface. Over 0.02 mg of catalyst decreased photocatalytic activity due to the optical scattering and light screening effects of nanoparticles. It is due to particle aggregation, a barrier to light irradiation. The degradation efficiency is diminished with a catalyst concentration of 0.005 mg/mL. Doping metal with TiO_2 may function as cationic dopants, enhance its sensitivity to visible light, and prevent recombination by modifying its electronic band structure. At the end of 120 min, the Ag–TiO_2 nanofibers (NFs) (0.02 mg) may disintegrate at a maximum rate of 94% Palaniswamy et al. (2021).

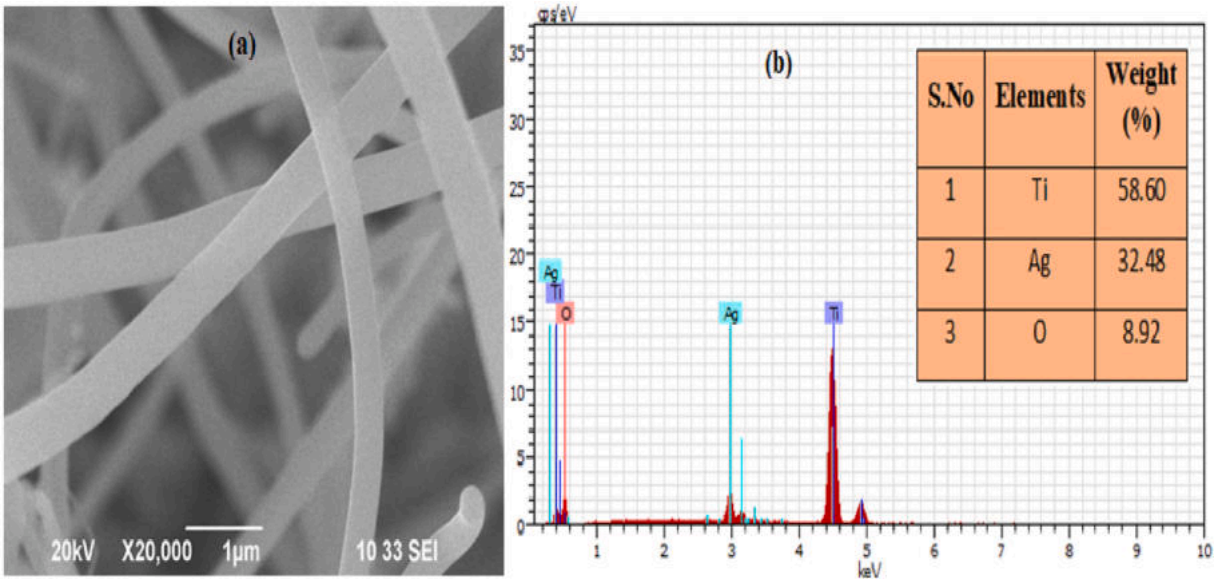

Fig. 2. (a, b) SEM and EDAX spectra of Ag–TiO_2 nanofibers (NFs).

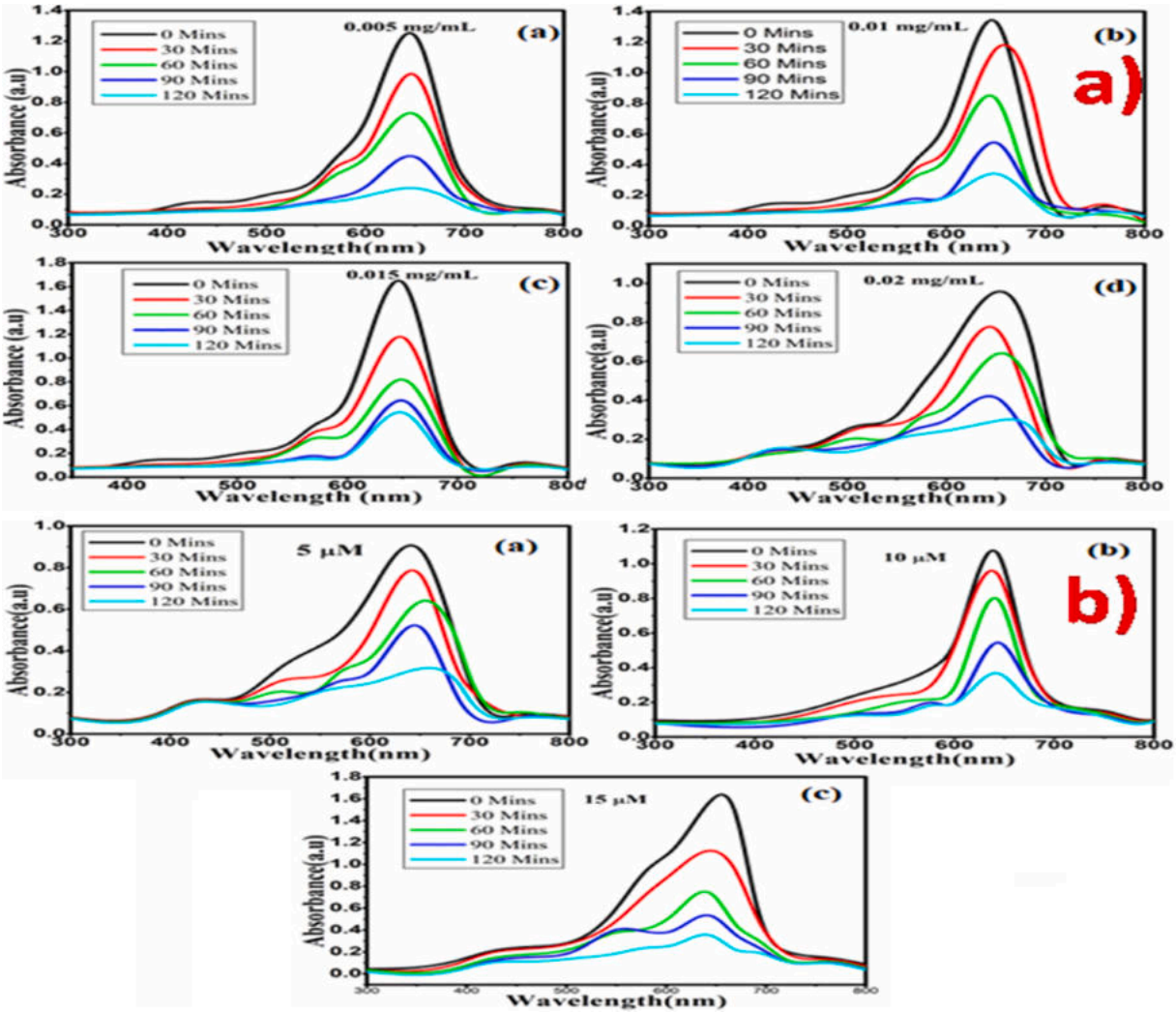

Fig. 3. (a and b): Time-dependent absorbance spectra (UV–Vis) of MB dye degradation (**Effect of catalyst 0.005 mg to 0.02 mg and effect of dye dosage 5 µM to 15 µM**).

3.5.3. *Effect of the dye concentration*

Fig. 3 b) illustrates the influence of diminishing efficiency on MB concentrations (5, 10, and 15 µM). As the dye concentration increases, the effectiveness of photocatalytic degradation decreases. At lower concentrations, more active sites from MB molecules are adsorbed by Ag–TiO_2 NFs. Increasing the dye concentration prevents photons from ever reaching the Ag–TiO_2 nanofibers (NFs) surface, reducing the dye removal efficiency. Increased dye concentrations reduce the travel length of photons, hence decreasing the light-activated catalyst Palanisamy et al. (2020).

3.5.4. *Photocatalytic degradation of malachite green*

Malachite green, commercial dye effluents, was used as a target Organic Compound Model (OCM) to assess the photo activity of the fluorescent Ag–TiO_2 nanofibers (NFs) photocatalyst. In light adsorption, the Ag–TiO_2 nanofibers (NFs) performance was inadequate; only a small percentage (3–4%) of the dye was degraded after 60 min. In Fig. 4 a), the Ag–TiO_2 nanofibers (NFs) photocatalyst reveals the maximum photocatalytic degradation efficiency of 92% at the end of I hrs, when exposed to visible light. As stated in the optical characteristics, the Ag–TiO_2 nanofibers (NFs) photocatalyst has low band-gap energy. Radical recombination outpaces separation when exposed to UV light, whereas electron-hole production is expected, and recombination is weak when exposed to visible light. Malachite green photodegrades in the sunshine without energy, which benefits both financially and environmentally. The negatively charged catalysts can easily be coated with cationic MG dye, and the Ag–TiO_2 nanofibers (NFs) photocatalyst demonstrates outstanding photocatalytic performance.

3.5.5. *Photocatalytic degradation of crystal violet*

The crystal violet photodegradation estimates the catalytic performance of Ag/TiO_2 NFs under sunlight irradiation for 60 min. Fig. 4 b) Shows the time-dependent UV–Vis absorbance spectra of crystal violet dye degradation. The first experiment subjected the CV solution to sunlight irradiation without using photocatalyst. According to the findings, solar radiation causes materials to degrade at roughly 3%. Degradation was barely detectable.

On the one hand, we observe that the photocatalytic activities of Ag–TiO_2 nanofibers (NFs) photocatalysts in sunlight are distinct. After 60 min of direct sunlight exposure, the photodegradation efficiency for Ag–TiO_2 nanofibers (NFs) photocatalyst shows 80.3%. The photocatalytic activity was often sensitive to the crystalline, surface OH groups, particular surface area, and photocatalyst surface roughness. As a result, the Ag–TiO_2 nanofibers (NFs) photocatalyst exhibits superior photocatalytic performance when exposed to visible radiation. Doping ions will increase the number of electrons and hole traps in the Ag–TiO_2 nanofibers (NFs) photocatalyst lattice, fastening the charge carriers and preventing the recombination rate of photo generated e^- and h^+,

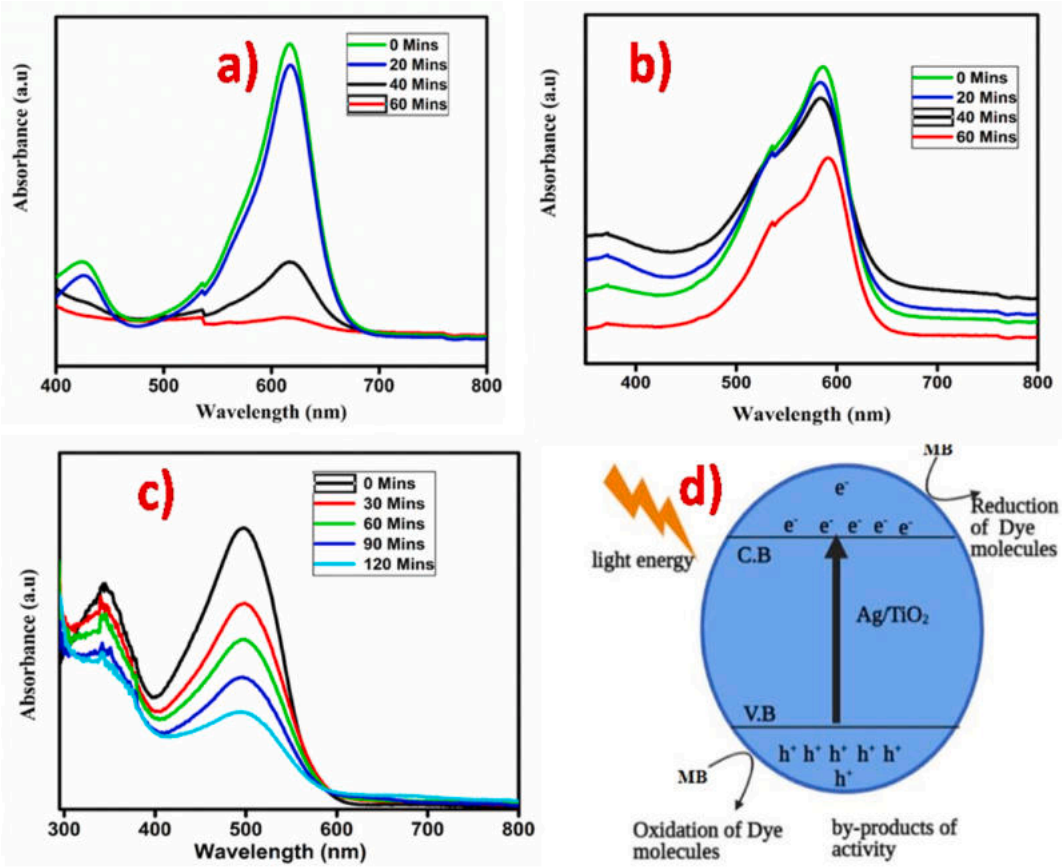

Fig. 4. (a–c) Time-dependent UV–Visible absorbance spectra of Malachite green, Crystal violet and Congo red and d) Possible reaction mechanism of dye degradation.

improving catalytic activity.

3.5.6. *Photocatalytic degradation of Congo red (CR) dye*

The decolourization of dye with initial concentrations (10 mg/L) CR under solar irradiation was used to evaluate the photocatalytic degradation efficiency of Ag–TiO_2 NFs. Fig. 4 c) shows the time-dependent UV–Vis absorbance spectra of CR dye degradation. The maximum absorbance (λ_{max}) of the supernatant dye solution determines the concentrations of the CR dye at 498 nm. The photocatalytic performance was improved, possibly due to the enhanced surface to volume ratio and band structure alteration of the Ag NPs. It effectively limited the recombination of photogenerated (e^-/h^+) pairs. CR dye degradation using Ag–TiO_2 nanofibers that were hydrothermally produced (NFs). At 492 nm, CR exhibits the highest absorption. The decline in CR dye's maximal absorption at regular intervals of 30 min is indicative of dye degradation. The activity of the catalysts was initially examined using 0.02 mg of the catalyst exposed to visible light for 120 min. However, in 120 min, Ag–TiO_2 nanofibers (NFs) demonstrated 80.5% photocatalytic degradation. The increased photocatalytic activity of Ag–TiO_2 nanofibers (NFs) implies that the addition of silver greatly enhances Ag–TiO_2 nanofibers (NFs) catalytic activity.

However, only about 80.5% of CR was decoloured for 50 mg/L concentrations. Therefore, when the original CR content increased, the photodegradation efficiency of CR photocatalysis by the Ag–TiO_2 nanofibers (NFs) powder also dropped. Two factors are primarily responsible for the decline in the semiconductor's degrading efficiency as CR concentration increases. More molecules are adsorbed on photocatalyst when the CR concentration increases, lowering their active sites. Therefore, as more of the catalyst surface is occupied, the production of hydroxyl radicals will be reduced.

On the other hand, raising the CR can decrease the number of photons that reach the catalyst surface. By adsorbing the light, CR molecules reduce photons' ability to excite photocatalyst particles. Consequently, photo degradation's effectiveness dropped. Under visible-light irradiation, the Ag–TiO_2 nanofibers (NFs) demonstrate effective photocatalytic activity in the breakdown of CR.

3.6. *Ag–TiO_2 based photocatalyst*

The catalytic performance of an Ag–TiO_2-based photocatalyst was compared with some other organics and is tabulated and summarized in Table 1. Table 1 shows that previously published Ag–TiO_2 catalysts could decolourize 79.8% of Methylene Blue dye in 150 min, while most Ag–TiO_2 composites could take more than 2 h to do the same. Compared to ternary composite materials, Ag–TiO_2 nanofibers (NFs) produced hydrothermally has a high photodegradation efficiency of 94% when exposed to sunlight (see Table 2).

3.7. *Structural and morphological stability of Ag–TiO_2 nanofibers (NFs)*

Powder XRD and SEM were used in the study to investigate the structural and morphological stability of Ag–TiO_2 nanofibers (NFs) (Fig. 5 a, b). According to the XRD pattern, the initial crystalline phase and structure of the Ag–TiO_2 nanofibers (NFs) subjected to photodegradation did not change. Because dye molecules were incorporated into the material, the SEM pictures show a few agglomerations, leading to subtle morphological changes when the material was degraded.

3.8. *Reusability*

The stability and reusability of the optimized Ag–TiO_2 nanofibers (NFs) towards the dye degradation of MB were studied under sunlight

Table 1
Comparison of photocatalytic performance of Ag/TiO_2 with reported literature.

Catalyst	Model pollutant Dye	Performance (%)	Source of light	Irradiation time (Min)	Reference
Ag/TiO_2	MB	79.8	Visible	150	Zhao et al. (2017)
PS@Ag@TiO_2	MB	90	Visible	30	Cha et al. (2009)
Ag_2O/ZnO–TiO_2	RhB	95	Visible	150	Wani and Ganie (2021)
Pristine Ag/TiO_2	MO/RhB	77/84	Sunlight	180	Heng et al. (2021)
Ag/Ag_2S–TiO_2	CV	28.92	Sunlight	120	Shuang et al., (2018)
Ag–Ag_2O/TiO_2@polypyrrole	MB	83.9	UV	120	Kumar et al. (2016)
Fe_3O_4–TiO_2–Ag	MB	90.1	Visible light	85	Ghafuri et al. (2019)
Ag_2O/TiO_2	MB	95.4	Visible light	180	Kavitha et al. (2021)
Fe_2O_3/TiO_2	MB	-	UV	60	Ahmed et al. (2013)
g–CN–TiO_2	MB	-	UV	-	Vijayan et al. (2023)
TiO_2-GO	MG and MB	85 and 93	Visible	60	Verma et al. (2023)
SiO_2–TiO_2	MB	90	Visible	30	Mahanta et al. (2022)
Cu_2O–CuO//TiO_2	MB and MO	87	Visible	120	Ansari et al. (2022)
Fe_3O_4/TiO_2	RhB	91	Visible	120	Madima et al. (2022)
G-TiO_2	MB	-	Visible	120	Shimi et al. (2022)
Ag/TiO_2	MB	94	Sunlight	120	**Present work**

Table 2
Shows Zone of inhibition values of bacterial strains.

S.No	Gram positive (S. Aureus)	Gram negative (E-coli)
1.	14 mm	17 mm

exposure for five cycles. The concentration of MB dye should be constant in each cycle, and the recovered centrifuged catalyst should be used in subsequent cycles of the degradation process. The motivation remains efficient and has remarkable photo stability even after four cycles. Maximum MB dye degradation occurs after 120 min, and the efficiencies for the 1st, 2nd, 3rd, 4th, and 5th cycles are 92%, 92%, 92%, 90%, and 90%, respectively. Therefore, the results of the present investigation support the notion that Ag–TiO_2 nanofibers (NFs) formed during the photocatalytic degradation of MB under solar light irradiation may

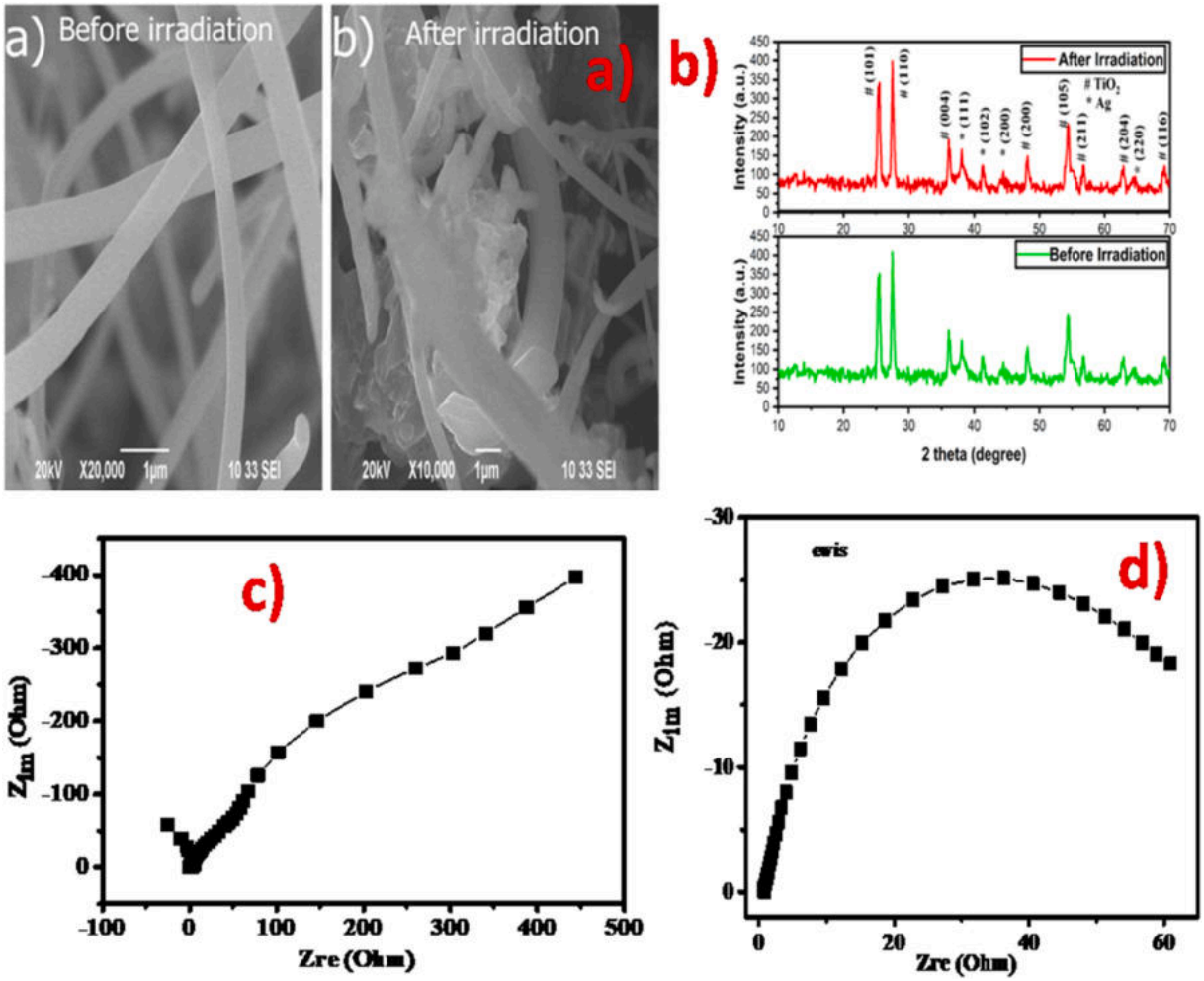

Fig. 5. (a & b) shows Morphological and Structural stability of Ag–TiO_2 nanofibers (NFs) after 5 cycles and (c & d) shows EIS spectra of Ag–TiO_2 nanofibers (NFs).

exhibit excellent photo stability, longer life span, and photo corrosion resistance.

3.9. Electrochemical impedance spectroscopy

The three-electrode electrochemical analyser performed Mott-Schottky (MS) and electrochemical impedance spectroscopy (EIS). The working electrode active area was 0.5 cm^2 by 1.0 cm^2. EIS was carried out using an open circuit voltage of 0.2 V and an AC voltage of 5 mV with a 0.1 Hz to 100 kHz frequency. The photo generated charge carrier separation and transfers were analysed during the catalytic process using the EIS of as-prepared activated carbon. Generally, the Nyquist plot semicircle radius represents the reaction rate at the photocatalyst surface. The reduced arc radius in the Nyquist plot (Fig. 5 c and d) suggests that surface imperfections in the produced Ag–TiO_2 nanofibers (NFs) may be the cause of the enhanced photoreaction and improved efficient charge transfer with decreased electrical resistance Wilke et al. (2018).

3.10. Antibacterial activity

Fig. 6 (a) represents the antibacterial screening of Ag–TiO_2 nanofibers (NFs). Agar diffusion was used to visualise the antibacterial activity of Ag–TiO_2 NFs. Due to their powerful antibacterial capabilities, metals and metal oxides are used to treat various bacterial illnesses. Due to their potent antibacterial activity, silver nanoparticles are traditionally used in medication delivery, biomedical imaging, tissue engineering, and cancer treatment. Nanoparticles based on TiO_2 are frequently employed for many applications Prakash et al. (2016). The cell wall membrane of gram-positive bacteria is composed of thin peptidoglycan easily disrupted by nanoparticles. Positive cell walls are composed of a 30 nm thick coating of peptidoglycan that is tough to degrade. Cell wall membranes are composed of lip polysaccharides, phospholipids, and proteins. Interactions between microorganisms and nanoparticles may change permeability and induce cell death Pinto et al. (2013). The inhibitory mechanism may involve (1) photocatalyst irradiation, (2) the production of active OH groups, and (3) the bombardment of silver ions and hydroxyl radicals on the bacterial cell wall, resulting in damage and death. TiO_2 nanoparticles disrupt bacterial cells by interacting with the cell wall membrane. The way bacteria breathe is changed by the plasmonic ions on the surface of TiO_2 nanofibers that are optically active (Parvathiraja and Shailajha, 2021). The interaction of Ag^+ ions with gram-negative bacteria results in electrostatic attraction. Ag-NPs attach to phosphorus and sulphur in the bacterial cell membrane, as well as other intercellular components like DNA bases and proteins, disrupting bacterial function and eventual death Naseem et al. (2016). As predicted, there is no inhibition zone in control. *E. coli* produces the largest inhibitory zone of the two examined bacterial strains, measuring 7 mm, whereas *S. aureus* produces a zone of 4 mm. Changes in the zone inhibitory layer are attributable to the varying susceptibility and size of nanoparticles. The bactericidal activity of nanoparticles may result from the binding of surface to bacteria, which depends on the

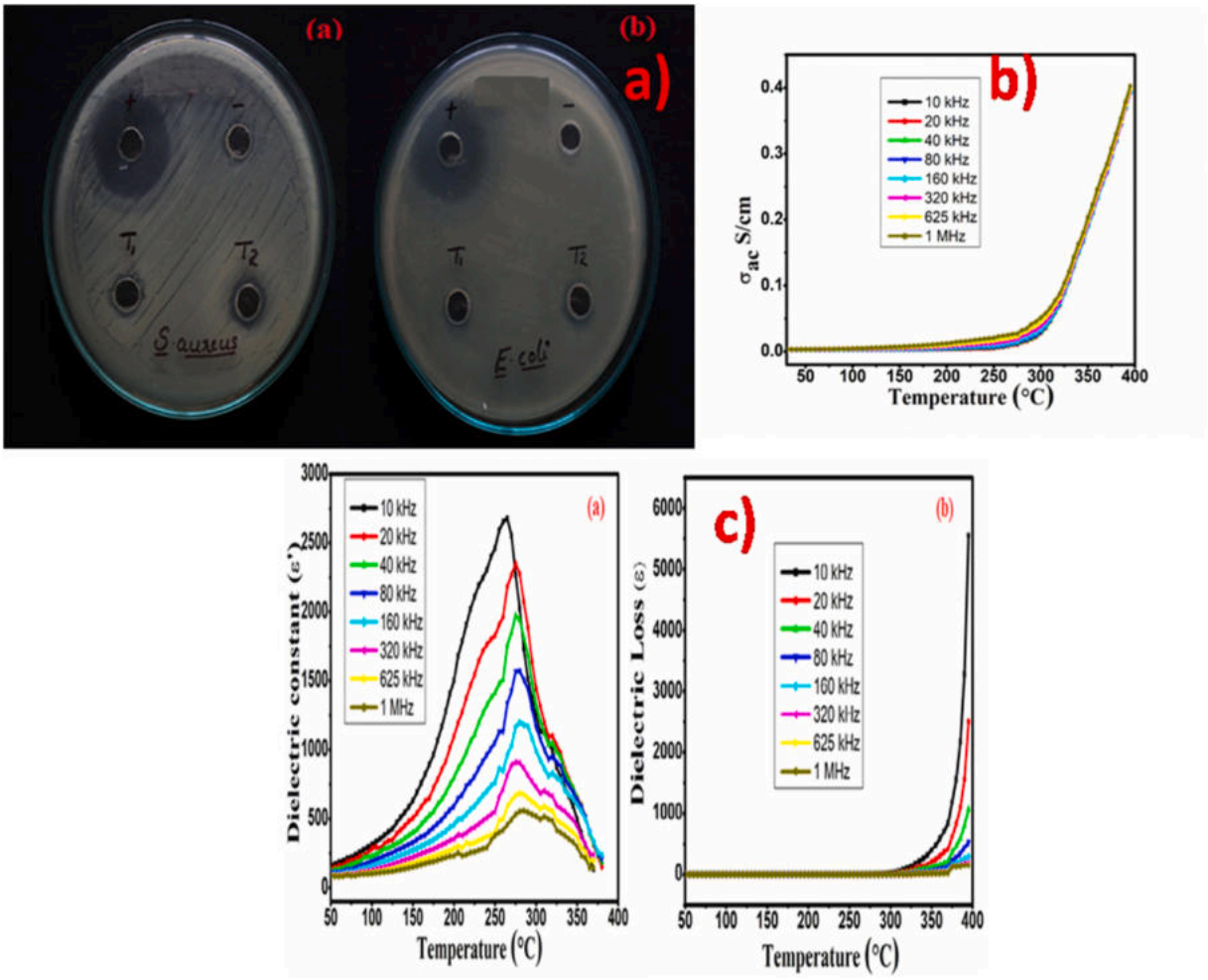

Fig. 6. a) antibacterial activity of Ag–TiO_2 nanofibers b) a. c conductivity spectra of Ag–TiO_2 nanofibers (NFs) and c) Dielectric properties of Ag–TiO_2 nanofibers (NFs).

amount of accessible surface area for interaction. As the particles' size rises, the surface O_2^-also concentration increases, resulting in a more efficient breakdown of the bacteria's cell wall and cytoplasmic membrane. Antibacterial activity is affected by the size and shape of the particles produced. Because of this, the nanocomposite made seems to be good for treating wastewater and biomedical uses. When compared to *Aureus* the gram negative *E-Coli* bacteria result higher zone of inhibition. Hence the prepared nanofibers are highly applicable for wood dressing and food packaging etc.

3.11. Dielectric properties

Fig. 6 (c) illustrate Ag–TiO_2 nanofibers (NFs) dielectric characteristics. Using a hydraulic pressure pellet under high pressure, the pellets were created. At various temperatures, the change in dielectric loss values is measured using frequencies ranging from 10 Hz to 1 MHz. A material's dielectric properties depend on its grain boundaries, grain size, charge carriers, charge orientations, temperature, the outside frequency, and how the experiment is done. Dielectric constant

$$\mathcal{E}' = \frac{Cd}{\mathcal{E}_o A} \tag{10}$$

where, C_p-capacitance, t-thickness, A-samples' area, $\mathcal{E}_o$-permittivity of free space ($\mathcal{E}_0 = 8.85 \times 10^{-12}$ F/m) Sharma et al. (2015).

Dielectric loss or permittivity is obtained from the value of the dissipation factor

$$D = \frac{\mathcal{E}''}{\mathcal{E}'} \tag{11}$$

$$\mathcal{E}'' = D \times \mathcal{E}' \tag{12}$$

where D is the Dissipation factor, $\mathcal{E}'$ is the Dielectric constant Suresh (2014).

As can be seen in Fig. 6 (c), the constant dielectric experiences an exponential decline with increasing frequency up to the point when it reaches a value that is almost constant in the high-frequency region. Results indicate that the dielectric constant values vary concerning temperature. Due to the frequency of electric charge carriers, dielectric constant values decrease with frequency; impurities, crystal flaws, and crystalline size result in greater dielectric loss factors at lower frequencies. When the quantity of nano-Ag in a composite is modest, it can be evenly dispersed to form many Coulomb islands, impeding electron transit and decreasing interfacial polarization. For higher temperatures, the space charge polarization is predominant. All four polarizations are present at low frequencies, so the dielectric constant value is high.

In contrast, these polarizations' progressive loss of significance at higher frequencies may account for their low value Jadhav and Biswas (2016). Positive and negative charges move towards the positive and negative electric field poles, respectively, when Ag–TiO_2 pellets are subjected to an external electric field. So, space-charge polarization happens at the Ag–TiO_2 surfaces, making nanocomposites with a much higher dielectric constant.

3.12. AC conductivity

The AC electrical conductivity were measured with different temperature. AC conductivity of Ag–TiO_2 nanofibers (NFs) was calculated using the formula

$$\sigma_{ac} = \omega \mathcal{E}_o \mathcal{E}' \tan\delta \tag{13}$$

where $\mathcal{E}_0$-permittivity of free space ($\mathcal{E}_0 = 8.85 \times 10^{-12}$ F/m), ω-angular frequency. Fig. 6 b) Illustrates the temperature-dependent AC conductivity of Ag–TiO_2 nanofibers (NFs). The conductivity (σ) was shown to increase with increasing temperature Kumar et al.. (2017). Crystalline size, grain and grain borders, surface-to-volume ratio, and nanocomposite structure determine AC conductivity. Thus, the composite material may be used in nanodevices, optoelectronics, and spintronic.

4. Conclusion

Using a hydrothermal technique effectively produced Ag–TiO_2 nanofibers (NFs). The Ag–TiO_2 nanofibers (NFs) XRD pattern reveals the FCC structure of silver and the anatase phase of TiO_2. From SEM investigation, nanofiber-shaped morphology was observed. The UV spectra of nanocomposites reflect their optical activity. For a 0.02 mg/mL concentration of catalyst, Ag–TiO_2 nanofibers (NFs) have a maximum degradation efficiency of 94%. The increase in photodegradation efficiency may be attributable to a reduction in crystalline size, particle size, e^- and h^+ recombination rates, and other factors. The antibacterial activity of Ag–TiO_2 nanofibers (NFs) is efficient against gram positive and gram-bacteria. So, the Ag–TiO_2 nanofibers (NFs) can be used in electrical, biological, and wastewater treatment applications.

Author contribution

M.A, A.N: Writing – original draft S.A; Data curation T.S; Revising; Reviewing and Editing, A.A, R.A.A, M.S.S.M; Data Collection; M.S; Supervision.

Declaration of competing interest

The authors declare that they have no known competing financial interests or personal relationships that could have appeared to influence the work reported in this paper.

Data availability

No data was used for the research described in the article.

Acknowledgements

This work was funded by the Researchers Supporting Project Number (RSP2023R265) King Saud University, Riyadh, Saudi Arabia.

References

Ahmad, A., Jini, D., Aravind, M., Parvathiraja, C., Ali, R., Kiyani, M.Z., Alothman, A., 2020. A novel study on synthesis of egg shell based activated carbon for degradation of methylene blue via photocatalysis. Arab. J. Chem. 13 (12), 8717–8722.

Ahmed, M.A., El-Katori, E.E., Gharni, Z.H., 2013. Photocatalytic degradation of methylene blue dye using Fe_2O_3/TiO_2 nanoparticles prepared by sol–gel method. J. Alloys Compd. 553, 19–29.

Ansari, F., Sheibani, S., Fernandez-García, M., 2022. Surface modification of Cu2O-CuO photocatalyst on Cu wire through decorating with TiO2 nanoparticles for enhanced visible light photocatalytic activity. J. Alloys Compd. 919, 165864.

Aqeel, M., Ikram, M., Imran, M., Ul-Hamid, A., Qumar, U., Shahbaz, A., Saeed, A., 2020. TiO_2 Co-doped with Zr and Ag shows highly efficient visible light photocatalytic behavior suitable for treatment of polluted water. RSC Adv. 10 (69), 42235–42248.

Aravind, M., Ahmad, A., Ahmad, I., Amalanathan, M., Naseem, K., Mary, S.M.M., et al., 2021. Critical green routing synthesis of silver NPs using jasmine flower extract for biological activities and photocatalytical degradation of methylene blue. J. Environ. Chem. Eng. 9 (1), 104877.

Arifin, M.N., Tarek, M., Khan, M.M.R., 2022. Efficient treatment of organic pollutants by boron doped TiO2 photocatalysts under visible light radiation. Chem. Eng. Res. Des. 180, 212–219.

Ashraf, R., Sofi, H.S., Akram, T., Rather, H.A., Abdal hay, A., Shabir, N., et al., 2020. Fabrication of multifunctional cellulose/TiO_2/Ag composite nanofibers scaffold with antibacterial and bioactivity properties for future tissue engineering applications. J. Biomed. Mater. Res. 108 (4), 947–962.

Carvalho, I., Ferdov, S., Mansilla, C., Marques, S.M., Cerqueira, M.A., Pastrana, L.M., et al., 2018. Development of antimicrobial leather modified with Ag–TiO_2 nanoparticles for footwear industry. Sci. Technol. Mater. 30, 60–68.

Cha, M.A., Shin, C., Kannaiyan, D., Jang, Y.H., Kochuveedu, S.T., Ryu, D.Y., Kim, D.H., 2009. A versatile approach to the fabrication of TiO 2 nanostructures with reverse morphology and mesoporous Ag/TiO 2 thin films via cooperative PS-b-PEO self-assembly and a sol-gel process. J. Mater. Chem. 19 (39), 7245–7250.

Chen, Q., Shi, H., Shi, W., Xu, Y., Wu, D., 2012. Enhanced visible photocatalytic activity of titania–silica photocatalysts: effect of carbon and silver doping. Catal. Sci. Technol. 2 (6), 1213–1220.
Ghafuri, H., Dehghani, M., Rashidizadeh, A., Rabbani, M., 2019. Synthesis and characterization of magnetic nanocomposite Fe_3O_4@ TiO_2/Ag, Cu and investigation of photocatalytic activity by degradation of rhodamine B (RhB) under visible light irradiation. Optik 179, 646–653.
Heng, J.Z.X., Tang, K.Y., Regulacio, M.D., Lin, M., Loh, X.J., Li, Z., Ye, E., 2021. Solar-powered photodegradation of pollutant dyes using silver-embedded porous TiO_2 nanofibers. Nanomaterials 11 (4), 856.
Jaber, M., Mushtaq, A., Zhang, K., Wu, J., Luo, D., Yi, Z., et al., 2020. Gram-scale synthesis of splat-shaped Ag–TiO_2 nanocomposites for enhanced antimicrobial properties. Beilstein J. Nanotechnol. 11 (1), 1119–1125.
Jadhav, J., Biswas, S., 2016. Structural and electrical properties of ZnO: Ag core-shell nanoparticles synthesized by a polymer precursor method. Ceram. Int. 42 (15), 16598–16610.
Javaid, M., Saleemi, A.R., Naveed, S., Zafar, M., Ramzan, N., 2011. Anaerobic treatment of desizing effluent in a mesophilic anaerobic packed bed reactor. J. Pakistan Inst. Chem. Engineers 39 (1), 61–67.
Kang, X., Liu, S., Dai, Z., He, Y., Song, X., Tan, Z., 2019. Titanium dioxide: from engineering to applications. Catalysts 9 (2), 191.
Kavitha, S., Ranjith, R., Jayamani, N., 2021. Facile construction of novel Ag_2O combined TiO_2 nanocomposites with enhanced dye degradation under visible-light photocatalytic activity. Mater. Technol. 1–15.
Kumar, M.A., Abebe, B., Nagaswarupa, H.P., Murthy, H.A., Ravikumar, C.R., Sabir, F.K., 2020. Enhanced photocatalytic and electrochemical performance of TiO_2-Fe_2O_3 nanocomposite: its applications in dye decolorization and as supercapacitors. Sci. Rep. 10 (1), 1–15.
Kumar, N.S., Ganapathy, M., Sharmila, S., Shankar, M., Vimalan, M., Potheher, I.V., 2017. ZnO/$Ni(OH)_2$ core-shell nanoparticles: synthesis, optical, electrical and photoacoustic property analysis. J. Alloys Compd. 703, 624–632.
Kumar, R., El-Shishtawy, R.M., Barakat, M.A., 2016. Synthesis and characterization of Ag-Ag_2O/TiO_2@ polypyrrole heterojunction for enhanced photocatalytic degradation of methylene blue. Catalysts 6 (6), 76.
Kurt, E., Koseoglu-Imer, D.Y., Dizge, N., Chellam, S., Koyuncu, I., 2012. Pilot-scale evaluation of nanofiltration and reverse osmosis for process reuse of segregated textile dyewash wastewater. Desalination 302, 24–32.
Li, Y., Tian, J., Yang, C., Hsiao, B.S., 2018. Nanocomposite film containing fibrous cellulose scaffold and Ag/TiO_2 nanoparticles and its antibacterial activity. Polymers 10 (10), 1052.
Liang, W., Qin, W., Li, D., Wang, Y., Guo, W., Bi, Y., et al., 2022. Localized surface plasmon resonance enhanced electrochemical nitrogen reduction reaction. Appl. Catal. B Environ. 301, 120808.
Liu, Y., Jia, J., Gao, T., Wang, X., Yu, J., Wu, D., Li, F., 2020. Rapid, selective adsorption of methylene blue from aqueous solution by durable nanofibrous membranes. J. Chem. Eng. Data 65 (8), 3998–4008.
Madima, N., Kefeni, K.K., Mishra, S.B., Mishra, A.K., Kuvarega, A.T., 2022. Fabrication of magnetic recoverable Fe3O4/TiO2 heterostructure for photocatalytic degradation of rhodamine B dye. Inorg. Chem. Commun. 145, 109966.
Mahanta, U., Khandelwal, M., Deshpande, A.S., 2022. TiO2@ SiO2 nanoparticles for methylene blue removal and photocatalytic degradation under natural sunlight and low-power UV light. Appl. Surf. Sci. 576, 151745.
Moradi, S., Fardood, S.T., Ramazani, A., 2018. Green synthesis and characterization of magnetic $NiFe_2O_4$@ ZnO nanocomposite and its application for photocatalytic degradation of organic dyes. J. Mater. Sci. Mater. Electron. 29 (16), 14151–14160.
Mukhopadhyay, S., Maiti, D., Chatterjee, S., Devi, P.S., Kumar, G.S., 2016. Design and application of Au decorated ZnO/TiO_2 as a stable photocatalyst for wide spectral coverage. Phys. Chem. Chem. Phys. 18 (46), 31622–31633.
Naseem, S., Khan, W., Naqvi, A.H., 2016. Influence of Ce doping on optical and dielectric properties of TiO2. In: AIP Conference Proceedings, vol. 1728. AIP Publishing LLC, p. *20*313. No. 1.
Palanisamy, V.K., Manoharan, K., Raman, K., Sundaram, R., 2020. Efficient sunlight-driven photocatalytic behavior of zinc sulfide nanorods towards Rose Bengal degradation. J. Mater. Sci. Mater. Electron. 31 (17), 14795–14809.
Palaniswamy, V.K., Ramasamy, B., Manoharan, K., Raman, K., Sundaram, R., 2021. Enhanced photocatalytic degradation of tetracycline antibiotic using m-$BiVO_4$ photocatalyst under visible light irradiation. Chem. Phys. Lett. 771, 138531.
Parvathiraja, C., Shailajha, S., 2021. Bioproduction of CuO and Ag/CuO heterogeneous photocatalysis-photocatalytic dye degradation and biological activities. Appl. Nanosci. 11 (4), 1411–1425.
Pinto, R.J., Daina, S., Sadocco, P., Neto, C.P., Trindade, T., 2013. Antibacterial Activity of Nanocomposites of Copper and Cellulose. BioMed research international, 2013.
Prakash, J., Kumar, V., Kroon, R.E., Asokan, K., Rigato, V., Chae, K.H., et al., 2016. Optical and surface enhanced Raman scattering properties of Au nanoparticles embedded in and located on a carbonaceous matrix. Phys. Chem. Chem. Phys. 18 (4), 2468–2480.
Priyanka, U., Lens, P.N., 2022. Light driven Aspergillus Niger-ZnS nanobiohybrids for degradation of methyl orange. Chemosphere 298, 134162.
Rao, T.N., Babji, P., Ahmad, N., Khan, R.A., Hassan, I., Shahzad, S.A., Husain, F.M., 2019. Green synthesis and structural classification of Acacia nilotica mediated-silver doped titanium oxide (Ag/TiO_2) spherical nanoparticles: assessment of its antimicrobial and anticancer activity. Saudi J. Biol. Sci. 26 (7), 1385–1391.
Roongraung, K., Chuangchote, S., Laosiripojana, N., 2020a. Enhancement of photocatalytic oxidation of glucose to value-added chemicals on TiO2 photocatalysts by a zeolite (Type y) support and metal loading. Catalysts 10 (4), 423.
Roongraung, K., Chuangchote, S., Laosiripojana, N., Sagawa, T., 2020b. Electrospun Ag-TiO_2 nanofibers for photocatalytic glucose conversion to high-value chemicals. ACS Omega 5 (11), 5862–5872.
Santos, L.M., Machado, W.A., França, M.D., Borges, K.A., Paniago, R.M., Patrocinio, A.O., Machado, A.E., 2015. Structural characterization of Ag-doped TiO_2 with enhanced photocatalytic activity. RSC Adv. 5 (125), 103752–103759.
Sharma, S., Nanda, K., Kundu, R.S., Punia, R., Kishore, N., 2015. Structural properties, conductivity, dielectric studiesand modulus formulation of Ni Modified ZnO nanoparticles. J. Atomic, Molecular, Condensed Matter and Nano Phys. 2 (1), 15–31.
Shen, S., Chen, K., Wang, H., Fu, J., 2022. Construction of carbon dots-deposited TiO2 Photocatalysts with visible-light-induced photocatalytic activity for the elimination of pollutants. Diam. Relat. Mater. 124, 108896.
Shimi, A.K., Ahmed, H.M., Wahab, M., Katheria, S., Wabaidur, S.M., Eldesoky, G.E., et al., 2022. Synthesis and applications of green synthesized TiO2 nanoparticles for photocatalytic dye degradation and antibacterial activity. J. Nanomater. 2022.
Shuang, S., Lv, R., Cui, X., Xie, Z., Zheng, J., Zhang, Z., 2018. Efficient photocatalysis with graphene oxide/Ag/Ag_2S–TiO_2 nanocomposites under visible light irradiation. RSC Adv. 8 (11), 5784–5791.
Suresh, S., 2014. Studies on the dielectric properties of CdS nanoparticles. Appl. Nanosci. 4 (3), 325–329.
Thakur, S., Das, P., Mandal, S.K., 2020. Solvent-Induced diversification of CdS nanostructures for photocatalytic degradation of methylene blue. ACS Appl. Nano Mater. 3 (6), 5645–5655.
Upadhyay, G.K., Rajput, J.K., Pathak, T.K., Kumar, V., Purohit, L.P., 2019. Synthesis of ZnO: TiO_2 nanocomposites for photocatalyst application in visible light. Vacuum 160, 154–163.
Verma, N., Chundawat, T.S., Chandra, H., Vaya, D., 2023. An efficient time reductive photocatalytic degradation of carcinogenic dyes by TiO2-GO nanocomposite. Mater. Res. Bull. 158, 112043.
Vijayan, M., Manikandan, V., Rajkumar, C., Hatamleh, A.A., Alnafisi, B.K., Easwaran, G., et al., 2023. Constructing Z-scheme g-C_3N4/TiO_2 heterostructure for promoting degradation of the hazardous dye pollutants. Chemosphere 311, 136928.
Wang, S., Wang, Y., Li, L., Li, L., Fu, G., Shi, R., et al., 2020. Green synthesis of Ag/TiO_2 composite coated porous vanadophosphates with enhanced visible-light photo-degradation and catalytic reduction performance for removing organic dyes. Dalton Trans. 49 (23), 7920–7931.
Wani, S.I., Ganie, A.S., 2021. Ag_2O incorporated ZnO− TiO_2 nanocomposite: ionic conductivity and photocatalytic degradation of an organic dye. Inorg. Chem. Commun., 108567
Wilke, C.M., Wunderlich, B., Gaillard, J.F., Gray, K.A., 2018. Synergistic bacterial stress results from exposure to nano-Ag and nano-TiO_2 mixtures under light in environmental media. Environ. Sci. Technol. 52 (5), 3185–3194.
Wong, C.W., Chan, Y.S., Jeevanandam, J., Pal, K., Bechelany, M., Abd Elkodous, M., El-Sayyad, G.S., 2020. Response surface methodology optimization of mono-dispersed MgO nanoparticles fabricated by ultrasonic-assisted sol–gel method for outstanding antimicrobial and antibiofilm activities. J. Cluster Sci. 31 (2), 367–389.
Yasar, A., Khalil, S., Tabinda, A.B., Malik, A., 2013. Comparison of cost and treatment efficiency of solar assisted advance oxidation processes for textile dye bath effluent. Kor. J. Chem. Eng. 30 (1), 131–138.
Zhang, L., Mohamed, H.H., Dillert, R., Bahnemann, D., 2012. Kinetics and mechanisms of charge transfer processes in photocatalytic systems: a review. J. Photochem. Photobiol. C Photochem. Rev. 13 (4), 263–276.
Zhao, Z.J., Hwang, S.H., Jeon, S., Hwang, B., Jung, J.Y., Lee, J., et al., 2017. Three-dimensional plasmonic Ag/TiO_2 nanocomposite architectures on flexible substrates for visible-light photocatalytic activity. Sci. Rep. 7 (1), 1–11.

Journal of Molecular Structure 1276 (2023) 134672

Contents lists available at ScienceDirect

Journal of Molecular Structure

journal homepage: www.elsevier.com/locate/molstr

Structural, Hirshfeld surface analysis, third order non-linear optical and molecular modelling of imidazolium glutarate single crystals for optical applications

Gino DJ[a,e,*], Chinnasami Sidden[b], Rajesh Paulraj[c], H. Marshan Robert[d,e], S. Ajitha[d,e]

[a] Research Scholar, Register Number: 18213102131006, Department of Physics and Research Centre, Nanjil Catholic College of Arts and Science, Kaliyakkavilai - 629153, Tamilnadu, India
[b] Department of Physics, V.S.B. Engineering College, Karur, Tamil Nadu 639111, India
[c] Centre for Crystal Growth, Department of Physics, SSN College of Engineering, Kalavakkam, Tamilnadu 603110, India
[d] Assistant Professor, Department of Physics and Research Centre, Nanjil Catholic College of Arts and Science, Kaliyakkavilai - 629153, Tamilnadu, India.
[e] Affiliated to Manonmaniam Sundaranar University, Abishekapatti, Tirunelveli - 627012, Tamilnadu, India

ARTICLE INFO

Article history:
Received 5 September 2022
Revised 23 November 2022
Accepted 27 November 2022
Available online 28 November 2022

Keywords:
Single crystal
XRD studies
Hirshfeld surface
Z-scan
Hyperpolarizability
MEP

ABSTRACT

The Imidazolium glutarate (IMGA) single crystal was grown using a low-temperature solution growth method. The title crystal belongs to the triclinic crystal structure with space group P1. ^{13}C and ^{1}H nuclear magnetic resonance spectra were recorded to evaluate the environment of the title compound. The grown crystal (2 0 2) was orientated using powder X-ray diffraction (XRD) studies. The vibrational modes present in the title compound were confirmed through Fourier transform infrared (FT-IR) and FT-Raman spectral studies. The IMGA crystal is stable up to 150 °C and material weight loss occurs between 150 and 258 °C. The UV–Vis-NIR studies show that 75% transmission in the entire visible region. The crystals' dielectric loss and constant were calculated as a function of frequency. Intermolecular interactions and fingerprint plots of the IMGA were executed by the Hirshfeld Surface (HS) analysis. The theoretical nonlinear optical (NLO) properties like first-order hyperpolarizability and dipole moment have been studied. The 3rd order NLO susceptibility and related parameters have been studied by Z-scan measurement.

1. Introduction

Organic materials are more attractive and versatile in the field of molecular optoelectronics [1,2]. The interactions between the molecules in organic compounds provide electrical, conducting, and optical properties [3]. Organic crystals have the significant advantage of being able to be modified according to our demands in terms of material qualities and chemical structure. The molecules in the crystal structure of the imidazolium-based dicarboxylic crystals form hydrogen-bonded chains, with strong N–H···O hydrogen bonds connecting the imidazolium cations and strong O–H···O type connections connecting the carboxylate anions [4,5]. Both kinds of chains self-assemble into layers or a supramolecular network. Imidazole is a critically important nitrogen heterocycle with unique biological and NLO characteristics [6,7]. Because of its chemical structure, imidazole can act as both a weak acid and a base, it serves as a proton transfer agent in living systems. Horike et al. [8], have achieved a significant improvement in proton conductivity in a metal-organic framework (MOF)-based compound by using the proton donor-accepter capacities and rotational motions of a type of heterocyclic imidazole molecule. In addition, MacDonald et al. [9], Fuller et al. [10], and K. Pogorzelec-Glaser et al. [11] have produced anhydrous entirely organic proton conductors that are hydrogen-bonded (H-bonded). The structure of imidazolium glutarate (IMGA) and its electrical properties have been reported by Pogorzelec-Glaser et al. [11]. However, theoretical research can be useful in understanding the relationship between structure and property, which can help in the development of NLO properties. Using the Gaussian 09 w software, the molecular electrostatic potential (MEP), highest occupied molecular orbital and lowest unoccupied molecular orbital (HOMO-LUMO), hyperpolarizability, natural bond orbital (NBO) of the IMGA molecule have been determined [12]. The relationship between structure and NLO properties of imidazolium-based organic single crystals such as imidazolium hydrogen succinate [13], imidazolium L-tartrate [14], imidazolium diphenylacetate diphenylacetic acid [15] and 2ethylimidazolium D-tartrate [16] have been studied both experimental and theoretical. In this point of view, the title compound was studied both experimental (single crystal XRD, powder XRD, FT-IR, FT-Raman, etc.) and theoretical (optimized structure, HOMO-LUMO, NBO,

* Corresponding author.
E-mail address: ginojohnwel@gmail.com (G. DJ).

https://doi.org/10.1016/j.molstruc.2022.134672
0022-2860/

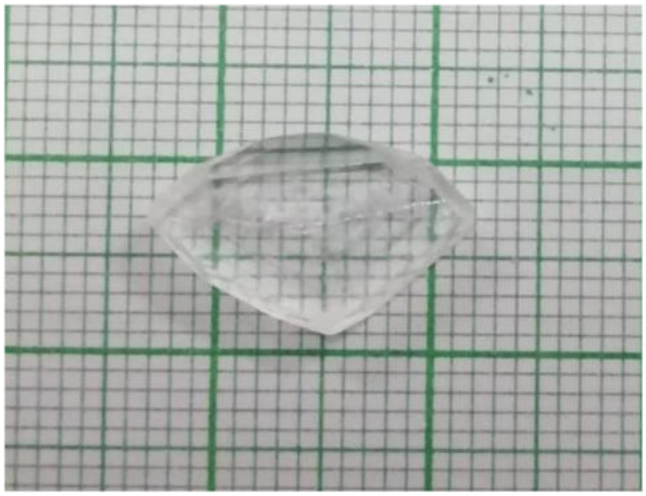

Fig. 1. As grown IMGA single crystal.

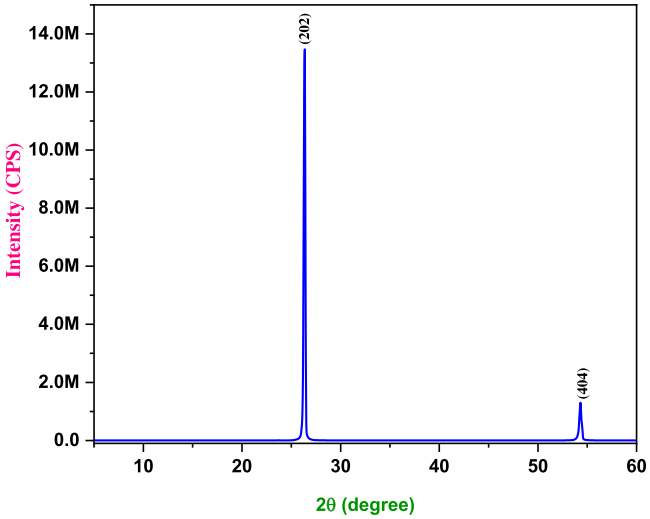

Fig. 3. Powder XRD pattern took along (1 0 1) plane of the IMGA crystal.

MEP, etc.). The obtained results are discussed in the forthcoming sessions.

2. Materials and methods

2.1. Growth of IMGA crystal

IMGA was synthesized by the reaction between imidazole (6.808 g, Merck) and glutaric acid (13.212 g, Loba chemical) taken in a 1:1 ratio. The calculated amount of glutaric acid was slowly added to a saturated aqueous solution of equimolar imidazole at room temperature to prepare the growth solution. A magnetic stirrer was used to thoroughly agitate the supersaturated solution for three hours at room temperature, producing a homogeneous mixing of the solution. Then the solution was filtered twice using a Whatman filter paper and put into a beaker covered with a thin polythene cover to reduce the rate of evaporation. Tiny crystals have been formed on the bottom of the beaker due to spontaneous nucleation. The purity and size of the crystal were improved by two times recrystallization processes. After 30 days, an optically transparent good quality IMGA crystal of size 15 × 10 × 2.5 mm^3 was obtained. Fig. 1 shows the as-grown crystal of IMGA.

2.2. Computational details

The Hirshfeld surface and related fingerprint analysis were performed by CRYSTAL EXPLORER 3.1 [17]. The Gaussian 09 W programme has been used to do the quantum chemical computation (gas phase) of the IMGA using the Becke-3-Lee-Yang-Parr (B3LYP) level of theory [18] supplemented with the standard 6–311++G(d,p) basis set [19,20]. The GAUSSIAN 09 W package was used to determine the geometrical parameters, including energy, band gap, bond angle, dihedral angle, and atomic charges of the title molecule. The Gauss View 5.0 application [21] was used to display the optimized geometry. As a result, the B3LYP/6–311++*G*(d,p) basis set was used to generate the Mulliken atomic charge (MAC) distribution, HOMO-LUMO, MEP, and first-order hyperpolarizability, which were then viewed using the Gauss View 5.0 program. The title molecule's NBO analysis was computed using the NBO 3.1 programme [22].

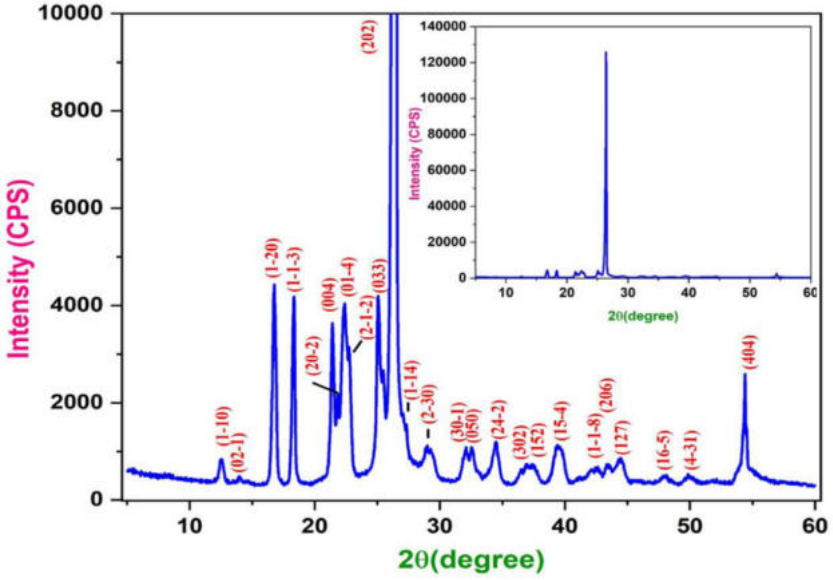

Fig. 2. Enlarged powder XRD pattern and observed powder XRD pattern of IMGA crystal.

Table 1
Observed lattice parameters of IMGA crystal.

Parameters	Single Crystal XRD (Present study)	Reported Data [7]
Crystal structure	Triclinic	Triclinic
a	8.34 Å ± 0.05	8.420 Å (2)
b	13.56 Å ± 0.08	13.685 Å (3)
c	16.97 Å ±0.09	17.068 Å (3)
α	90.53° ±0.09	90.62° (3)
β	103.59° ± 0.20	103.45° (3)
γ	91.17° ± 0.14	91.03° (3)
Volume (A^3)	1890 ± 30	1912.2 (7)

3. Result and discussions

3.1. X-ray diffraction (XRD) analysis

The IMGA crystal was subjected to single crystal X-ray diffraction (SCXRD) technique using SAINT (APEX II) and SHELXTL software for frame Integration and structure solution and refinement, respectively. It reveals that IMGA crystallizes in the triclinic system with space group P1. The observed lattice parameters (Cell lengths, angles, and volume) are given in Table 1. It is in good agreement with the reported data [11]. The powder and as-grown IMGA crystal were subjected to powder XRD (PXRD) analysis using the Empyrean X-ray Diffractometer technique. The observed PXRD pattern of powdered IMGA is shown in Fig. 2. This figure shows that (202) plane intensity is very high (~128,000 CPS) compared to other planes. The sharp high intensity plane indicates the crystalline quality is good. The enlarged PXRD pattern and indexed (hkl) planes of IMGA crystal are shown in Fig. 2.

Basically, the crystals are anisotropic in nature, it gives different optical and electrical parameters for different planes or directions. In this point of view, the grown crystal top surface plane was identified using the same PXRD configuration. The PXRD diffraction pattern of the (101) plane of IMGA crystal is shown in Fig. 3. The crystal's PXRD intensity is very high compared to the powdered sample's PXRD intensity. Fig. 3 indicates the order of (101) planes such as (202) and (404) planes and the corresponding 2θ values are 26.36° and 54.35°, respectively. The observed planes and 2θ values (Fig. 3) are well-matched in powder sample XRD lower angle 2θ values (Fig. 2).

3.2. FT-NMR studies

The ^{1}HNMR (500.23 MHz) and ^{13}CNMR (125. 78 MHz) spectra of the IMGA crystal were recorded using a 500 MHz FT NMR Spectrometer (BRUKER AVIII 500) in DMSO as solvent. The ^{1}H and ^{13}CNMR spectra show the signals due to various protons and carbons as shown in Figs. 4 and 5, respectively. Fig. 4, the strong signal due to imidazolium ring two symmetric protons appears in the region at 7.02 to7.03 ppm. The COOH proton occurs at 7.659 ppm. The –CH protons in the glutarate moiety appear in the region of 1.72 to 2.25 ppm [23]. Fig. 5, the two symmetric -CH carbon present of the imidazolium moiety, which causes the signal at 122.06 ppm. The peak at 135.58 ppm occurs in the spectra due to the peak for –CH carbon, which is located between two NH groups of the imidazolium moiety [24]. The peak at 174.5 ppm occurs in the spectra due to the two symmetric carbonyl carbon presence of glutarate moiety. The presence of other protons and carbons is given in Table 2. Between two NH groups of the imidazolium

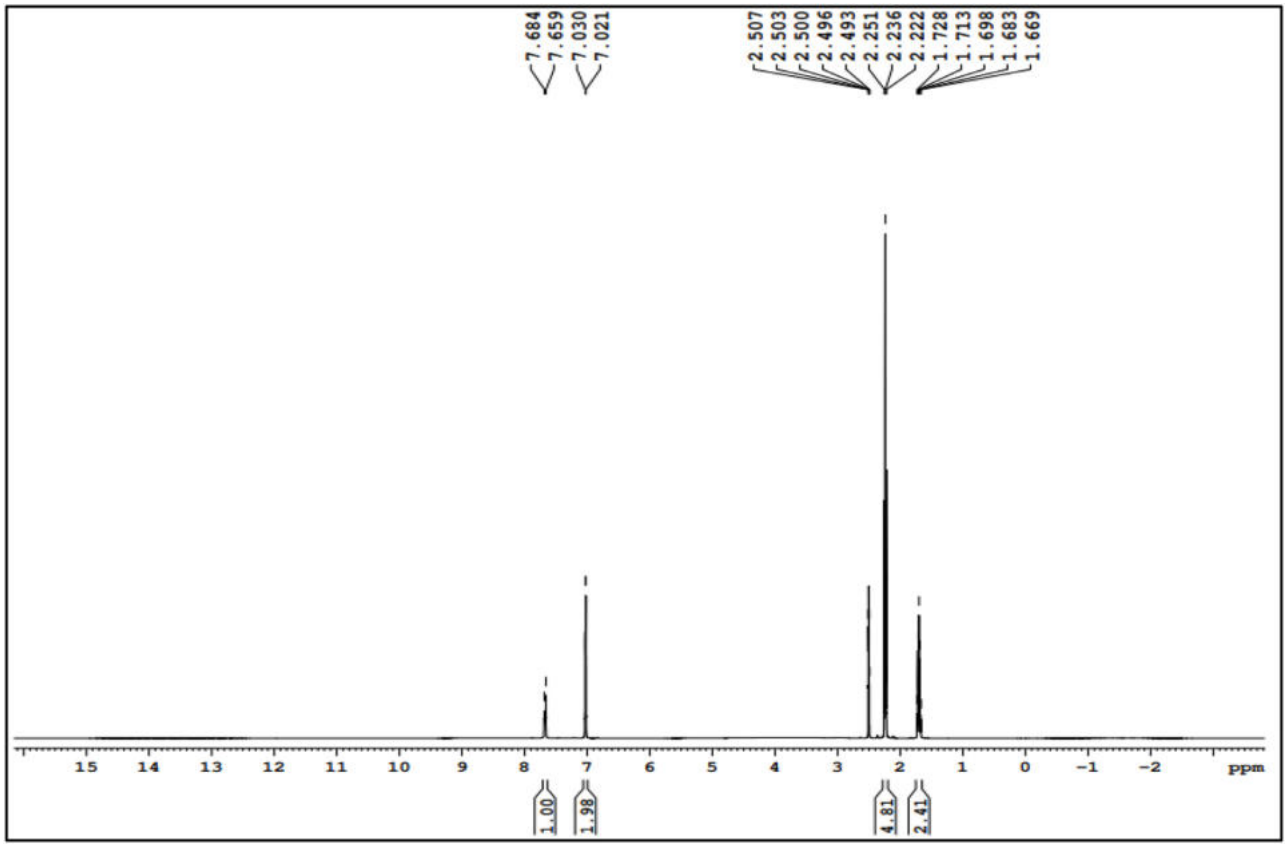

Fig. 4. ^{1}H NMR spectrum of IMGA crystal.

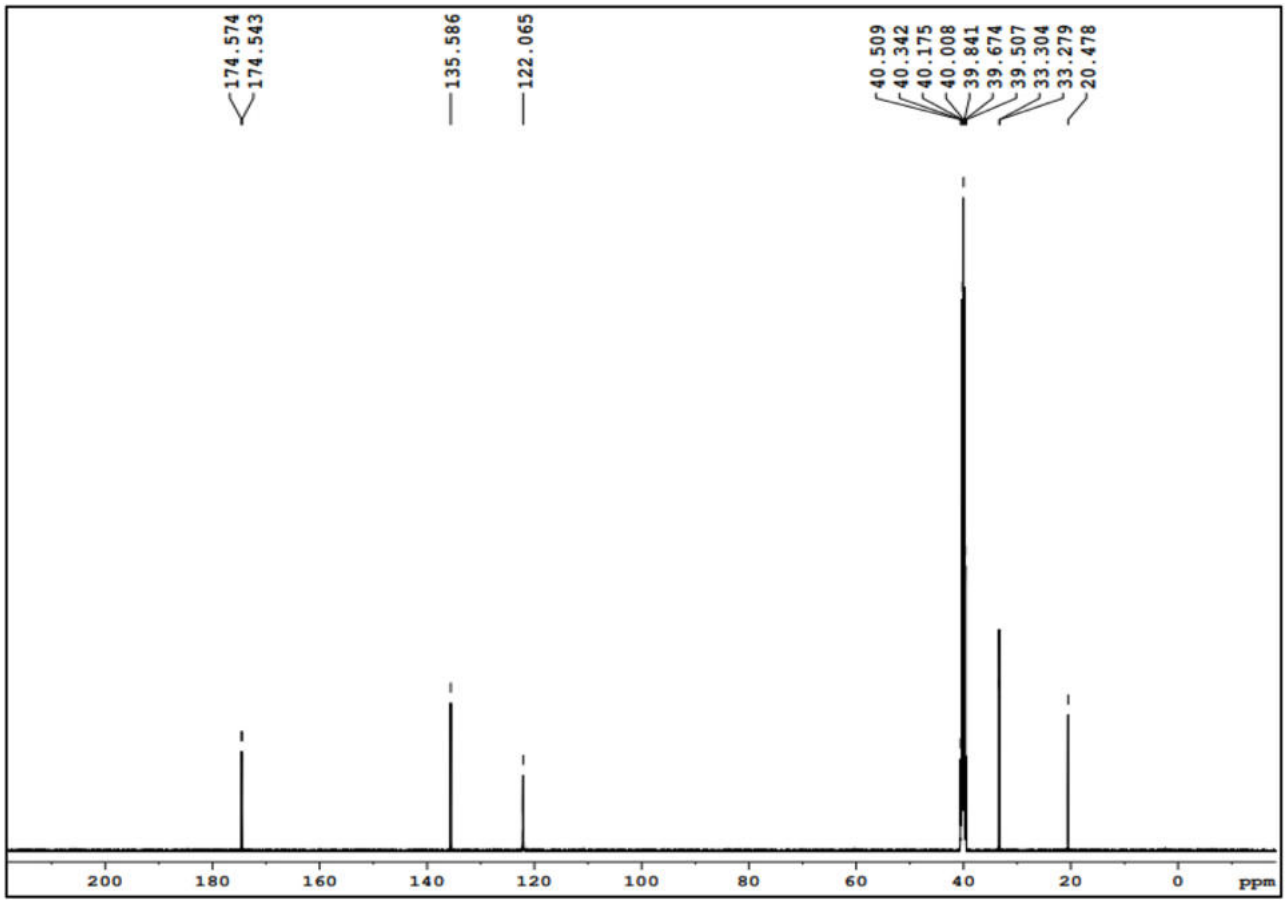

Fig. 5. ^{13}C NMR spectrum of IMGA crystal.

Table 2
Experimental ^{1}H & ^{13}C NMR chemical shift of IMGA crystal.

Atoms	^{13}C NMR (ppm)	Atoms	^{1}H NMR (ppm)
5C	20.478	10H	2.251
6C	33.279	11H	1.698
7C	174.543	12H	2.236
8C	20.478	13H	1.713
9C	33.304	14H	2.222
19C	135.586	15H	1.728
20C	122.065	16H	7.659
21C	122.065	22H	7.030
		23H	1.683
		24H	7.684
		25H	7.021
		26H	1.669

moiety, there is a peak for -CH carbon, which is what causes the peak at 135.58 ppm.

3.3. FTIR and FT-Raman studies

The recorded FTIR and FT-Raman spectrum of the IMGA compound are shown in Figs. 6 and 7, respectively. The standard organic spectroscopy literature is used to assign the observed vibrational modes [25,26]. Table 3 lists the IMGA compound's observed vibrational modes and assignments. The O – H bending modes (in the plane and out of the plane) of the carboxylic acid group [27] are observed at 1412 and 911 cm^{-1} in FTIR and 1420 and 910 cm^{-1} in FT-Raman, respectively. The aromatic C – H bending modes (in the plane and out of plane) of the imidazole ring are observed at 1095 and 775 cm^{-1} in FTIR and 1094 and 775 cm^{-1} in FT-Raman, respectively. The presence of the NH^{+} stretching mode of the tertiary amine salt is responsible for the peak at 2970 cm^{-1} in FTIR and 2930 cm^{-1} in FT-Raman. The presence of COO^{-} asymmetric and symmetric stretching modes of the carboxylate group are responsible for the peaks at 1680 and 1315 cm^{-1} in FTIR and 1685 and 1302 cm^{-1} in FT-Raman, respectively. The formation of the title compound's molecular structure reveals the existence of an amine salt (NH^{+}) and a carboxylate group (COO^{-}). Herewith the important vibrational modes are discussed, and the other vibrational modes are given in Table 3.

3.4. Hirshfeld surface (HS) analysis

The idea behind HS came from an effort to define the area a molecule takes up in a crystal to divide the crystal's electron density into molecular units of electron density. The two distances di, the distance from the HS to the closest nucleus inside the surface, and de, the distance from the HS to the closest nucleus outside the surface on HS, were compared to create fingerprint plots [28,29]. The d_{norm} surface exhibits either negative or positive values, when compared to the total of the van der Waals radii, depending on the length of intermolecular interaction. The SCXRD data (CIF file) were subjected to HS analysis using Crystal Explorer 3.1 [30]. Fig. 8**a** and **b** display the HS plotted over the d_i and d_e properties in the range of 0.569 Å (red) to 2.343 Å (blue) and 0.571 Å (red) to 2.380 (blue), respectively. Fig. 8**c** displays the HS plotted over the d_{norm} property in the range of −0.861 Å (red) to 1.063 Å (blue). Intermolecular interactions (IMIs) are shown through colour coding. Intermolecular interactions with distances

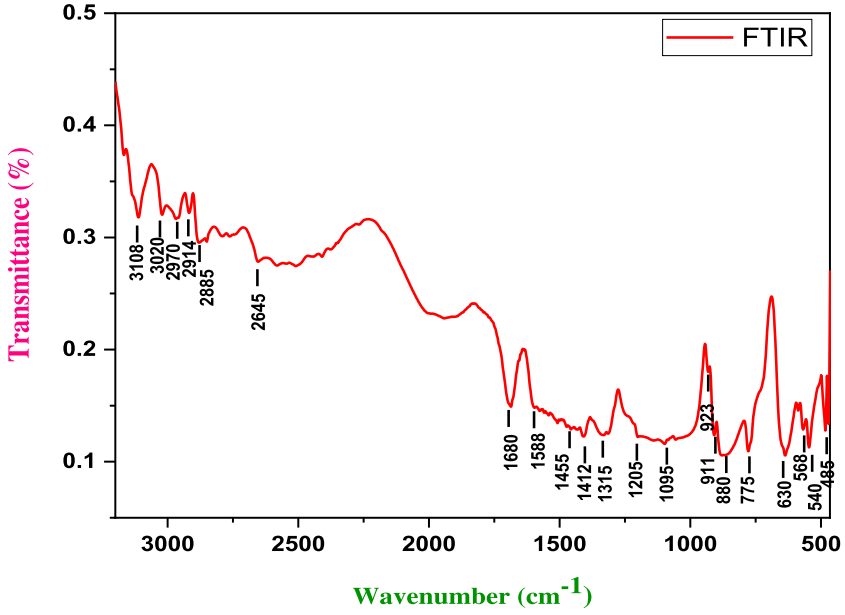

Fig. 6. FT-IR Spectrum of IMGA crystal.

Table 3
FTIR and FT-Raman vibrational assignment of IMGA crystal.

Wavenumber (cm^{-1})		Mode of vibrations	Assignments
FTIR	FT-Raman		
3108	–	N–H stretching	Presence of amine group
3020	–	Aromatic C–H stretching	Presence of imidazole ring
2970	2930	NH^{+}stretching	Presence of tertiary amine salt
2914	–	C–H stretching	Presence of tertiary C–H group
2885	2885	C = O stretching	Presence of carboxylic acid group
1680	1685	COO^{-} asymmetric stretching	Presence of carboxylate group
1588	1590	C–N stretching	Presence of imidazole ring
1455	1450	N–H in plane bending	Presence of amine group
1412	1420	C–O stretching and O–H in plane bending (coupled)	Presence of carboxylic acid group
1315	1302	COO^{-} symmetric stretching	Presence of carboxylate group
1205	1230	C–O stretching	Presence of hydroxyl group
1095	1094	Aromatic C–H in plane bending	Presence of imidazole group
911	910	O–H in plane bending	Presence of carboxylic acid group
775	775	Aromatic C–H out of plane bending	Presence of imidazole group
630	630	O–H out of plane bending	Presence of hydroxyl group

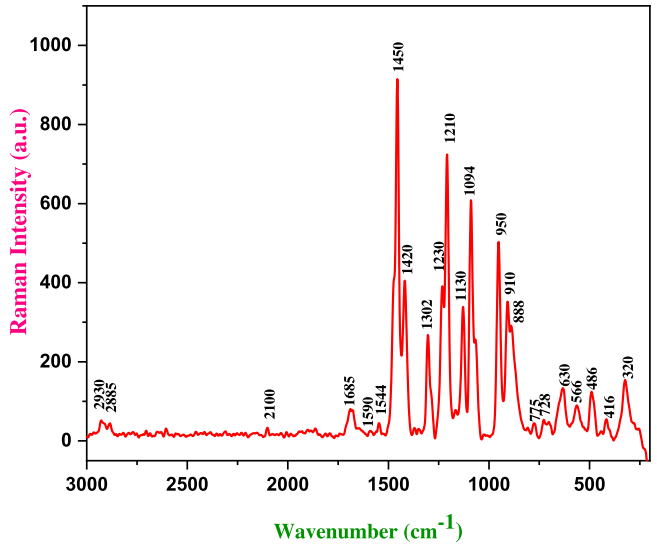

Fig. 7. FT-Raman Spectrum of IMGA crystal.

smaller than, equal to, and greater than van der Waal radii are indicated by the red, white, and blue marks, respectively [31,32]. Large circular depressions (deep red) that are suggestive of hydrogen bonding connections can be seen on the d_{norm} surfaces, while additional visible spots are caused by H···H contacts. HS plots of the hydroxyl O–H and carbonyl O atom in 1 may be seen as the bright red area in Fig. 8c indicating the dominant interactions between these two atoms. C–H···O interactions are the cause of the title compounds' light red spots. For each interatomic contact and all interactions, 2D fingerprint plots are generated. When calculating individual interatomic distances, contacts, as well as each interatomic contact's reciprocal contact.

The 2D fingerprint plot for overall interactions is shown in Fig. 9. The dominant IMIs of the total HS for IMGA molecule are H···H (36.6%) interactions. For each molecule, the proportions of O···H and H···O interactions contribute 52.1% of the total HS. The other IMIs are given in Fig. 9. Fig. 8**d** and **e** display the HS plotted over the shape index and curvedness surfaces. The curvedness surface clearly shows a flat zone toward the bottom of both sides of the molecules, indicating the presence of $\pi-\pi$ stacking [33]. On the surface, this feature looks like a rather flat green area with extremely comparable contact distances.

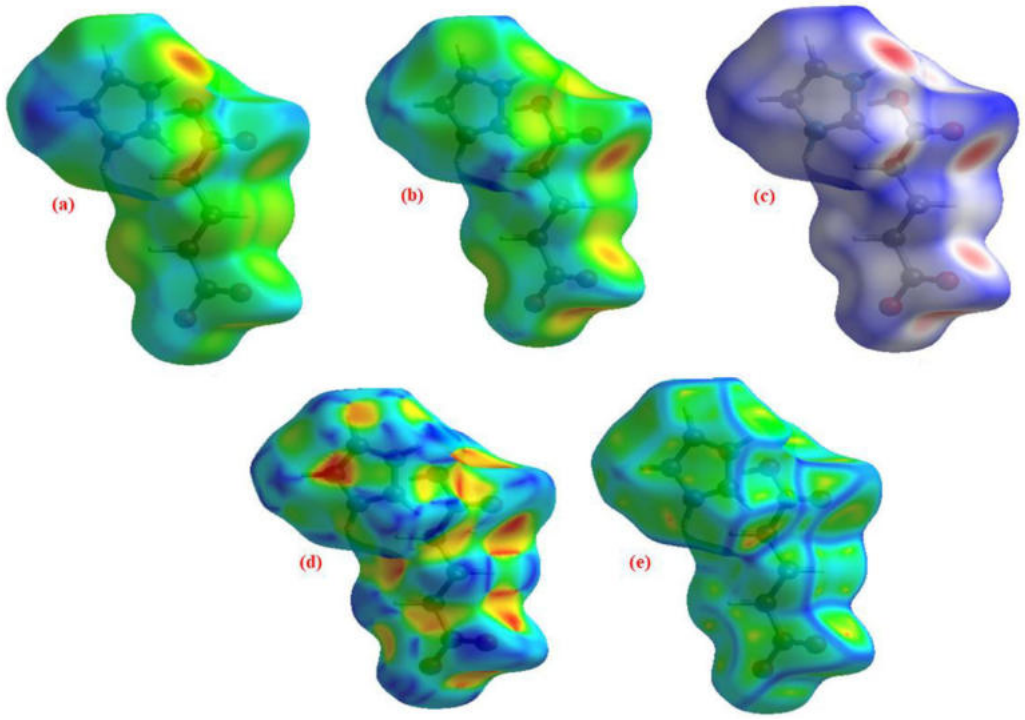

Fig. 8. 3D Hirshfeld surfaces of IMGA molecule (a) d_i (b) d_e (c) d_{norm} (d) Shape index and (e) Curvedness.

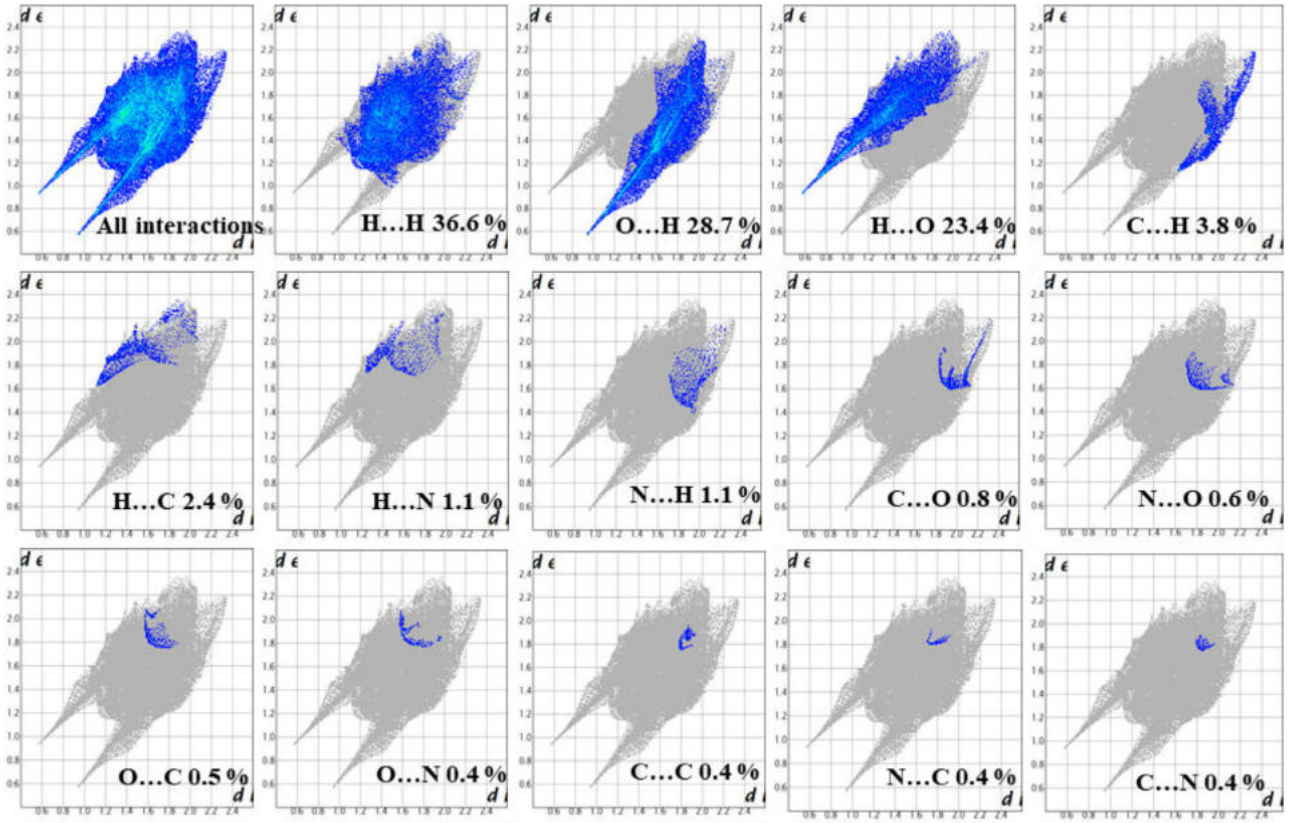

Fig. 9. 2d fingerprints plots of IMGA molecule.

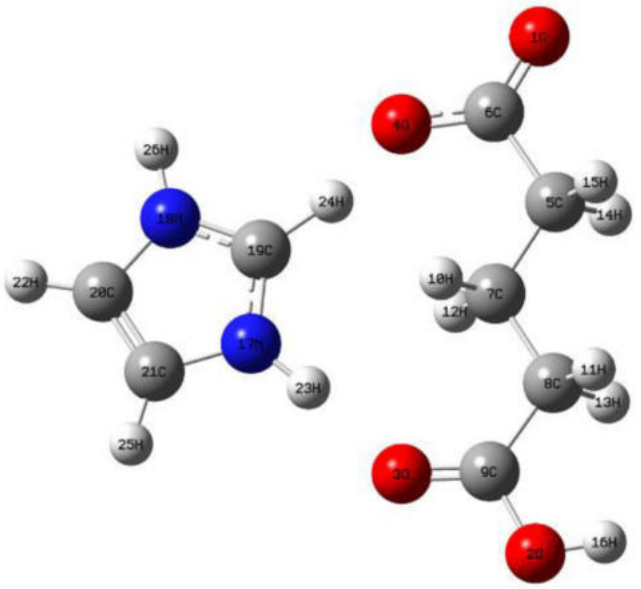

Fig. 10. Optimized structure of IMGA molecule.

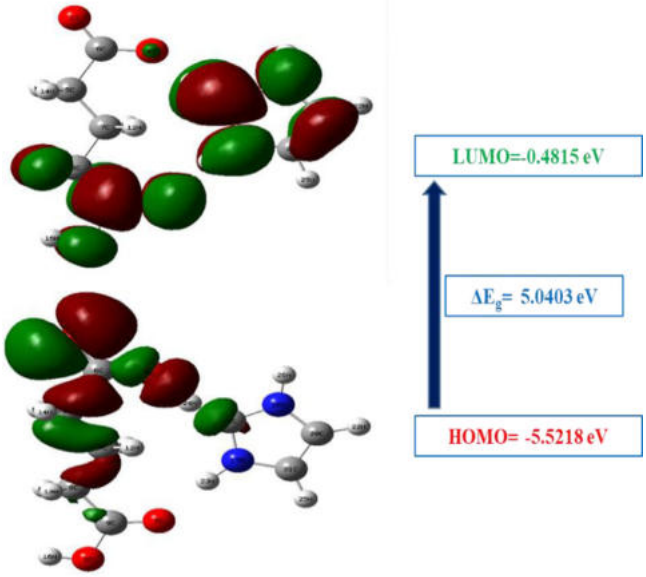

Fig. 11. HOMO-LUMO energy diagram of IMGA molecule.

3.5. Optimal geometry analysis

Fig. 10 displays the IMGA's optimal geometry as computed by the B3LYP approaches with atom numbering. Table 4 shows the optimized bond lengths and bond angles of the IMGA compound as determined using ab-initio DFT(B3LYP) technique using the 6–311++*G*(d,p) basis set. The majority of the optimal bond lengths in Table 4 are slightly longer than the experimental values. Because the actual results are based on molecules in the solid state and the theoretical calculations are based on isolated molecules in the solid phase [34].

The optimized C–C bond lengths for IMGA using DFT/B3LYP fall in the range of 1.362–1.532 Å, while the experimental C–C bond lengths fall in the range of 1.361–1.562 Å. The C_{19}–N_{17} and C_{21}–N_{17} bond lengths in the imidazole ring are found to be varied from 1.3408 to 1.3842 Å in B3LYP, demonstrating that the boundary between single and double bonds inside the ring is present due to electron conjugation. The C–H bond lengths determined from the theoretical values range between 1.097 and 1.099 Å, while the experimental value is between 0.955 and 0.990 Å. This greater variation in C–H bond lengths may be brought on by the X-ray diffraction studies' low scattering coefficients for hydrogen atoms, which are not taken into account in theoretical models [35]. All the C–C–C bond angles (C_7–C_8–C_9, C_5–C_7–C_8, and C_6–C_5–C_7) in glutarate are around 114° in the experimental and 115° in B3LYP. The angles of C_{19}–N_{18}–C_{20} and C_{19}–N_{17}–C_{21} are 111.082° and 110.755° in B3LYP and 109.15° and 109.28° in experimental, respectively. Herewith the important optimized structural parameters are discussed and other structural parameters are given in Table 4**.**

3.6. Frontier molecular orbitals

Understanding the electrical and optical properties of organic molecules depends heavily on the study of frontier molecular orbitals [36,37]. The stabilization of the bonding molecular orbital increases with an increase in the overlap of the two orbitals. In a similar vein, the antibonding's instability also increases [38]. The HOMO and LUMO orbitals, which combine to form one orbital, are two significant orbitals that are involved in molecule interaction. Using the B3LYP/6–311++*G*(d,p) level to determine the HOMO-LUMO energy gap of IMGA, it was found that the energy gap represents the chemical activity of the molecule. The ability to receive an electron is represented by LUMO as an electron acceptor, and the ability to give an electron is represented by HOMO. Fig. 11 depicts the distributions and energy levels of the HOMO and LUMO orbitals for the gas phase IMGA molecule. The imidazole ring and half of the glutarate portion are where the charge density is primarily accumulated. But in the case of the LUMO, in the case of LUMO, more charge density moves to the glutarate moiety. The computed HOMO-LUMO energy gap ΔE_g is 5.0403 eV. The GCRD properties such as electronegativity (χ), chemical potential (μ), global hardness (η), electrophilicity index (ω) formulas, and calculated values are given in Table 5**.** The quantitative structure-property, structure-activity/toxicity analysis uses the global chemical reactivity descriptor (GCRD) values to determine chemical reactivity and permanence [39].

3.7. Mulliken atomic charges

Applying DFT calculations to molecular systems, the determination of atomic charges is crucial [40]. The Mulliken atomic charges (MAC) of a single IMGA molecule are computed using the B3LYP level of theory and the 6–311++*G*(d,p) basis set. Table 6 displays the MAC on the constituent atoms of the IMGA molecule. The carbon atoms C19, C20, and C21 are positive within the imidazole ring due to the attraction of the electronegative nitrogen atom. In Fig. 12**,** the carbon atoms C6, and C9 are positive within the glutarate moiety, whereas other carbon atoms are negative. This is caused by the electronegative oxygen atom, which attracts the positive charge from the carbon atoms. All of the hydrogen atoms have a net positive charge, as seen in Table 6. Additionally, MACs indicate that the N–H group of hydrogen atoms, which is connected to an N atom, has a larger positive atomic charge than the other hydrogen atoms. This is caused by the electronegative nitrogen atom, which attracts the positive charge from the hydrogen atoms [41].

3.8. Molecular electrostatic potential (MEP) analysis

For studying and predicting molecular reactive behaviour, the electrostatic potential formed in the area around a molecule by its nuclei and electrons (considered as static distributions of charge)

Table 4
Optimized geometric parameters of IMGA molecule.

Bond Length	Cal. Values (Å)	Exp. Values (Å)	Bond Angle	Cal. Values (°)	Exp. Values (°)	Dihedral Angle	Cal. Values (°)	Exp. Values (°)
O_1-C_6	1.231	1.274	C_9-O2-H16	110.017	112.90	H_{16}-O_2-C_9-O_3	−179.994	179.52
O_2-C_9	1.349	1.295	C_9-O_3...H_{23}	135.590	135.39	H_{16}-O_2-C_9-C_8	0.0066	−0.47
O_2-H_{16}	0.968	1.042	C_6-O_4...H_{24}	138.063	135.44	H_{23}-O_3-C_9-O_2	180.029	176.70
O_3-C_9	1.217	1.229	C_6-C_5-C_7	115.197	114.12	H_{23}-O_3-C_9-C_8	0.028	−2.28
O_3...H_{23}	1.810	1.878	C_6-C_5-H_{14}	107.264	106.12	C_9-O_3-H_{23}-N_{17}	179.959	−161.28
O_4-C_6	1.288	1.247	C_6-C_5-H_{15}	107.264	105.40	H_2-O_4-C_6- O_1	−179.999	−178.70
O_4...H_{24}	1.442	2.250	C_7-C_5-H_{14}	110.891	111.74	H_{24}-O_4-C_6-C_5	0.0017	−1.34
C_5-C_6	1.562	1.510	C_7-C_5-H_{15}	110.894	109.83	C_6-O_4-H_{24}...C_{19}	179.998	169.55
C_5-C_7	1.525	1.531	H_{14}-C_5-H_{15}	105.901	107.31	C_7-C_5-C_6-O_1	179.984	−172.64
C_5-H_{17}	1.097	1.095	O_1-C_6-C_4	126.760	122.26	C_7-C_5-C_6-O_4	−0.0165	6.58
C_5-H_{15}	1.097	0.990	O_1-C_6-C_5	116.386	116.90	H_{14}-C_5-C_6-O_1	−56.713	−47.95
C_7-C_8	1.527	1.515	O_4-C_6-C_5	116.852	120.83	H_{14}-C_5-C_6-O_4	123.285	131.27
C_7-H_{10}	1.0951	0.993	C_5-C_7-C_8	115.451	114.73	H_{15}-C_5-C_6-O_1	56.679	65.69
C_7-H_{12}	1.0951	0.989	C_5-C_7-H_{10}	108.769	108.65	H_{15}-C_5-C_6-O_4	−123.322	−115.09
C8-C9	1.5189	1.511	C_5-C_7-H_{12}	108.765	113.02	C_6-C5-C_7-C_8	179.998	176.24
C_8-H_{11}	1.0997	0.954	C_8-C_7-H_{10}	108.352	108.55	C_6-C5-C_7-H_{10}	−57.994	−64.64
C_8-H_{13}	1.0997	1.008	C_8-C_7-H_{12}	108.349	109.27	C_6-C5-C_7-H_{12}	57.997	53.26
N_{17}-C_{19}	1.3408	1.324	H_{10}-C_7-H_{12}	106.821	106.44	H_{14}-C_5-C_7-C_8	58.680	58.683
N_{17}-C_{21}	1.3842	1.369	C_7-C_8-C_9	115.914	114.33	H_{14}-C_5-C_7-C_{10}	−179.313	173.61
N_{17}-H_{23}	1.0308	0.930	C_7-C_8-H_{11}	111.033	110.77	H_{14}-C_5-C_7-H_{12}	−63.32	−68.45
N_{18}-C_{19}	1.3445	1.305	C7-C_8-H_{13}	111.030	108.32	H_{15}-C_5-C_7-C_8	−58.682	−64.48
N_{18}-C_{20}	1.3862	1.362	C_9-C_8-H_{11}	107.854	108.35	H_{15}-C_5-C_7-H_{10}	63.324	54.64
N_{18}-H_{26}	1.0102	0.972	C_9-C_8-H_{13}	107.852	108.08	H_{15}-C_5-C_7-H_{12}	179.317	172.54
C_{19}-H_{24}	1.1859	0.986	H_{11}-C_8-H_{13}	105.831	105.51	C_5-C_7-C_8-C_9	180.002	173.16
C_{20}-C_{21}	1.3611	1.362	O_2-C_9-O_3	118.148	120.16	C_5-C_7-C_8-H_{11}	58.720	49.65
C_{20}-H_{22}	1.0775	0.916	O_2-C_9-C_8	116.475	115.85	C_5-C_7-C_8-H_{13}	−58.73	−65.61
C_{21}-H_{25}	1.0776	0.905	O_3-C_9-C_8	125.376	123.99	H_{10}-C_7-C_8-C_9	57.767	53.97
			C_{19}-N_{17}-C_{21}	110.755	109.28	H_{10}-C_7-C_8-H_{11}	−63.510	−69.53
			C_{19}-N_{17}-H_{23}	123.684	122.74	H_{10}-C_7-C_8-H_{13}	179.039	175.20
			C_{21}-N_{17}-H_23	125.560	127.97	H_{12}-C_7-C_8-C_9	−57.779	−61.72
			C_{19}-N_{18}-C_{20}	111.082	109.15	H_{12}-C_7-C_8-H_{11}	−179.057	174.78
			C_{19}-N_{18}-H_{26}	122.295	127.61	H_{12}-C_7-C_8-H_{13}	63.493	59.51
			C_{20}-N_{18}-H_{26}	126.622	123.24	C_7-C_8-C9-O_2	−179.992	−176.71
			N_{17}-C_{19}-N_{18}	105.569	108.06	C_7-C_8-C9-O_3	0.0083	2.30
			N_{17}-C_{19}-H_{24}	129.823	125.60	H_{11}-C_8-C_9-O_2	−56.930	−51.94
			N_{18}-C_{19}-H_{24}	124.607	126.04	H_{11}-C_8-C_9-O_3	123.070	127.07
			N_{18}-C_{20}-C_{21}	105.867	107.26	H_{13}-C_8-C_9-O_2	56.951	61.94
			N_{18}-C_{20}-H_{22}	122.898	126.21	H_{13}-C_8-C_9-O_3	−123.048	−119.05
			C_{21}-C_{20}-H_{22}	131.234	126.55	C_{21}-N_{17}-C_{19}-N_{18}	−0.003	−0.32
			N_{17}-C_{21}-C_{20}	106.725	106.24	C_{21}-N_{17}-C_{19}-H_{24}	−179.977	173.76
			N_{17}-C_{21}-H_{25}	122.409	117.87	H_{23}-N_{17}-C_{19}-N_{18}	180.008	179.01
			C_{20}-C_{21}-H_{25}	130.865	135.71	H_{23}-N_{17}-C_{19}-H_{24}	0.034	−6.92
			O_3...H_{23}-N_{17}	174.973	168.34	C_{19}-N_{17}-C_{21}-C_{20}	0.003	0.53
			O_4...H_{24}-C_{19}	166.077	173.27	C_{19}-N_{17}-C_{21}-H_{25}	179.999	176.46
						H_{23}-N_{17}-C_{21}-C_{20}	−180.009	−178.75
						H_{23}-N_{17}-C_{21}-H_{25}	−0.012	−2.82
						C_{19}-N_{17}-H_{23}...O_3	−180.019	167.39
						C_{21}-N_{17}-H_{23}...O_3	−0.005	−13.41
						C_{20}-N_{18}-C_{19}-N_{17}	0.002	−0.03
						C_{20}-N_{18}-C_{19}-H_{24}	179.977	174.07
						H_{26}-N_{18}-C_{19}-N_{17}	179.998	179.76
						H_{26}-N_{18}-C_{19}-H_{24}	−0.026	6.20
						C_{19}-N_{18}-C_{20}-C_{21}	−0.0009	0.36
						C_{19}-N_{18}-C_{20}-H_{22}	−180.004	179.94
						H_{26}-N_{18}-C_{20}-C_{21}	−179.996	−179.90
						H_{26}-N_{18}-C_{20}-H_{22}	0.0004	−0.31
						N_{17}-C_{19}-H_{24}...O_4	179.993	−168.86
						N_{18}-C_{19}-H_{24}...O_4	0.0243	4.37
						N_{18}-C_{20}-C_{21}-N_{17}	−0.0012	−0.53
						N_{18}-C_{20}-C_{21}-H_{25}	−179.998	−175.38
						H_{22}-C_{20}-C_{21}-N_{17}	180.002	179.88
						H_{22}-C_{20}-C_{21}-H_{25}	0.006	5.03

is a highly helpful property [42]. Fig. 13**,** shows that the MEP map of IMGA was obtained by DFT theory B3LYP/6–311++*G*(d,p) using Gaussian-09. The hydrophobic and hydrophilic components of the IMGA molecules are clearly visible in colour schemes. The hydrophilic sites, with negative carboxylate anions (red colour) and positively charged imidazolium cations (blue colour), may act as proton transport channels. Yellow colour depicts the region that is somewhat electron-rich and light blue depicts the region that is slightly electron-deficient [43]. The optimum location for an electrophilic attack is shown in the picture where the maximum electron density is localized near the nitrogen atom. The activation energy for imidazolium glutarate is reported to be the lowest (0.7 eV) [11]. The unique stacking of imidazolium rings amongst acid molecules may be the cause of such a low value. This makes it possible to construct a variety of N–H···O contacts, which are essential to the conducting mechanism.

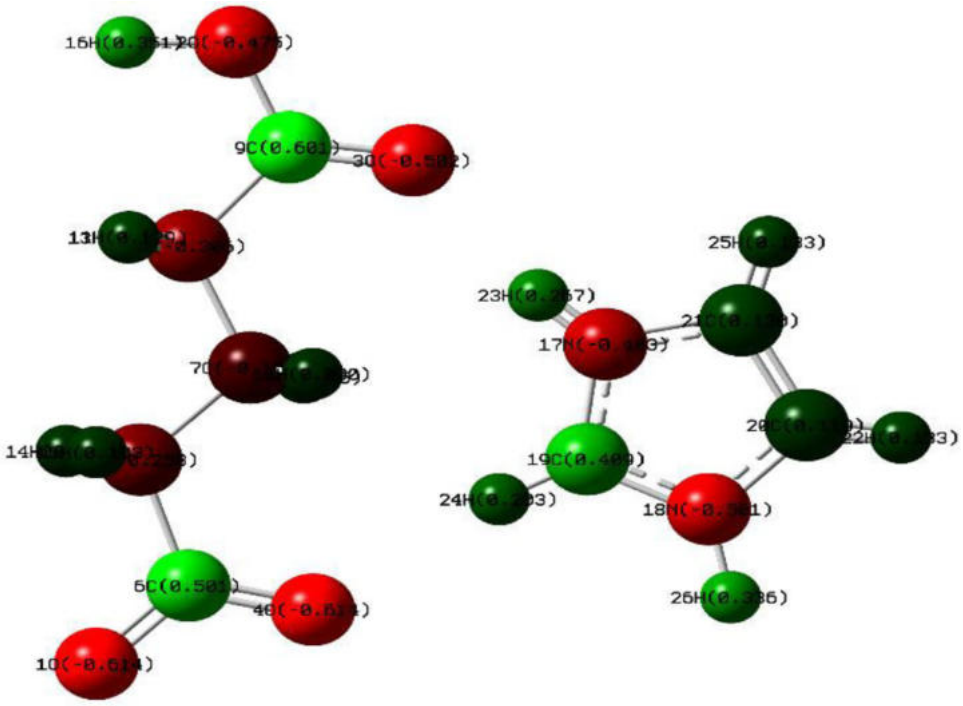

Fig. 12. Mulliken atomic charges of IMGA molecule.

Table 5
HOMO-LUMO and related global chemical reactivity descriptor properties of IMGA molecule.

Molecular properties	Mathematical description	Energy(eV)
E_{HOMO}	Energy of HOMO	−5.5218
E_{LUMO}	Energy of LUMO	−0.4815
Energy Gap	$\Delta E_g = E_{HOMO} - E_{LUMO}$	5.0403
IoniztionPotnetial(IP)	$IP = -E_{HOMO}$	5.5218
Electron Affinity (EA)	$EA = -E_{LUMO}$	0.4815
Electronegativity (χ)	$\chi = -1/2(E_{LUMO} + E_{HOMO})$	3.0016
Chemical potential (μ)	$\mu = 1/2(E_{LUMO} + E_{HOMO})$	−3.0016
Global Hardness(η)	$\eta = 1/2(E_{LUMO} - E_{HOMO})$	2.5201
Softness (S)	$S = 1/2\eta$	0.1984
Electrophilicity index (ω)	$\omega = \mu^2/2\eta$	1.7875

Table 6
Mulliken atomic charges of IMGA molecule.

Atomic number	Mulliken atomic charge (atomic unit)	Atomic number	Mulliken atomic charge (atomic unit)
1O	−0.613678	14H	0.099259
2O	−0.475008	15H	0.102988
3O	−0.501716	16H	0.351105
4O	−1.260807	17N	−0.402936
5C	−0.614360	18N	−0.501291
6C	0.500762	19C	0.409086
7C	−0.162160	20C	0.118553
8C	−0.306131	21C	0.130269
9C	0.600581	22H	0.132886
10H	0.090273	23H	0.266825
11H	0.129468	24H	0.202609
12H	0.095012	25H	0.132585
13H	0.137162	26H	0.335592

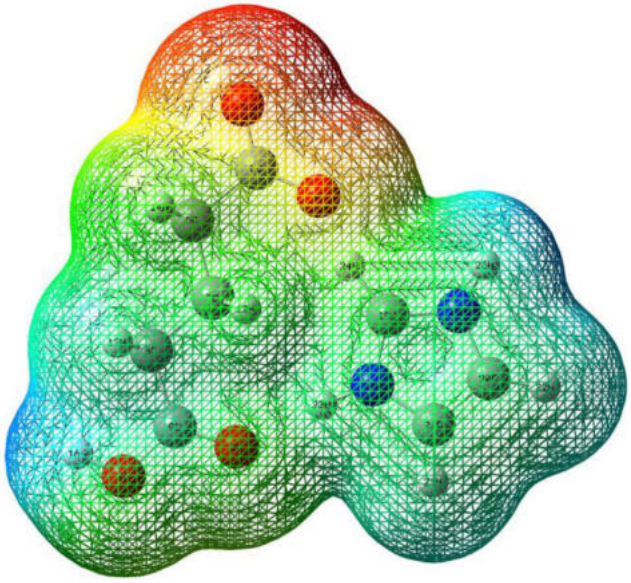

Fig. 13. MEP plot of IMGA molecule.

3.9. NBO analysis

Donor and acceptor orbitals, electron delocalization, intermolecular charge transfer (ICT), and the discovery of hydrogen bonding are all potential interactions that can be discovered via NBO analysis [44,45]. The NBO computation of the IMGA molecule was evaluated from the NBO 3.1 software program. To determine the stable structure, it is possible to calculate the energy contributions from several orbitals, including LP, π, π^*, σ, and σ^*, as a result of electron delocalization and conjugative interactions. It has with the NLO response [46], the system's overall conjugation is stronger and the electrical flow from electron D-A is more intense when the E(2) value is higher. The various Donor-Accepter (D-A) interactions present in IMGA are given in Table 7. The maximum stabilization energy (E(2)) of 87.88 Kcal/mol corresponds to the delocalization of IMGA with the transfer of LP to π^*(O–C) within a carboxylate group that is due to strong intermolecular charge transfers

Table 7
Donor–acceptor interactions of IMGA molecule.

Donor (i)	Occupancy (e)	Acceptor (j)	Occupancy (e)	E(2) kcal/mol	E(j)–E(i) (a.u)	F(i,j) (a.u)
σ(C5 – C6)	1.98599	σ^*(C8 – C9)	0.06308	2.92	0.93	0.047
π(O1 – C6)	1.99374	π^*(O1 – C6)	0.36456	2.87	0.40	0.034
σ(C5 – H15)	1.97310	π^*(O1 – C6)	0.36456	3.41	0.64	0.046
σ(C7 – C8)	1.97846	σ^*(O2 – C9)	0.08346	3.57	0.97	0.053
σ(C8 – H11)	1.96882	σ^*(O3 – C9)	0.03201	3.73	1.14	0.058
LP(2) O1	1.88271	σ^*(O4 – C6)	0.05773	20.31	0.78	0.114
LP(2) O1	1.88271	σ^*(C5 – C6)	0.09359	17.73	0.59	0.092
LP(2) O2	1.79589	π^*(O3 – C9)	0.23339	52.42	0.36	0.123
LP(2) O3	1.86094	σ^*(O2 – C9)	0.08346	29.90	0.68	0.130
LP(2) O3	1.86094	σ^*(C8 – C9)	0.06308	14.72	0.68	0.091
LP(2) O4	1.87292	σ^*(O1 – C6)	0.06903	20.59	0.78	0.115
LP(2) O4	1.87292	σ^*(C5 – C6)	0.09359	16.55	0.63	0.092
LP(3) O4	1.62152	π^*(O1 – C6)	0.36456	87.88	0.29	0.143
LP(1) O3	1.97010	σ^*(N17 – H23)	0.02719	4.57	1.49	0.074
LP(2) O3	1.97010	σ^*(N17 – H23)	0.02719	5.06	1.08	0.068
π(N17 – C19)	1.90007	π^*(C20 – C21)	0.25088	19.61	0.38	0.080
σ(N17 – C21)	1.98491	σ^*(C20 – H22)	0.00871	3.11	1.57	0.063
π(C20 – C21)	1.85271	π^*(N17 – C19)	0.46881	13.23	0.25	0.056
LP(1) N18	1.51994	π^*(N17 – C19)	0.46881	79.61	0.25	0.125
LP(1) N18	1.51994	π^*(C20 – C21)	0.25088	32.88	0.30	0.094
σ(C21 – H25)	1.98452	σ^*(N17 – C19)	0.01588	3.21	1.12	0.054
σ(C20 – C21)	1.98069	σ^*(N17 – H23)	0.02719	3.66	1.58	0.068
σ(C20 – C21)	1.98069	σ^*(N18 – H26)	0.01350	3.54	1.14	0.057

LP(3) O4 $\rightarrow$ π^*(O1-C6)). The delocalization of IMGA with the transfer of LP(1) N18 $\rightarrow$ π^*(N17-C19) and LP(2) O2 $\rightarrow$ π^*(O3-C9) possesses the E(2) of 79.61 and 52.42 Kcal/mol, respectively and showing that the formed crystal has a conjugative impact. The other strong delocalization of 32.88 and 29.90 Kcal/mol is produced by the conjugation with the lone pair of LP(1) N18 and LP(2) O3 when it is combined with π^*(C20 – C21) and O2 – C9), respectively. In IMGA, the D-A interactions are formed σ^*(by the orbital overlaps through $\pi \rightarrow \pi^*$ and $\sigma \rightarrow \sigma^*$ interactions such as π(C20 – C21) $\rightarrow$ π^*(N17 – C19) and σ(C20 – C21) $\rightarrow$ σ^*(N17 – H23) with the E(2) of 13.23 and 3.66 Kcal/mol, respectively. Herewith the important D-A interactions are discussed and the other D-A interactions are given in Table 7.

From the Table 7.

E(2) means stabilization energy.

E(j)-E(i) is the energy difference between donor and acceptor i and j NBO orbitals.

F(i,j) is the Fock matrix element between i and j NBO orbitals.

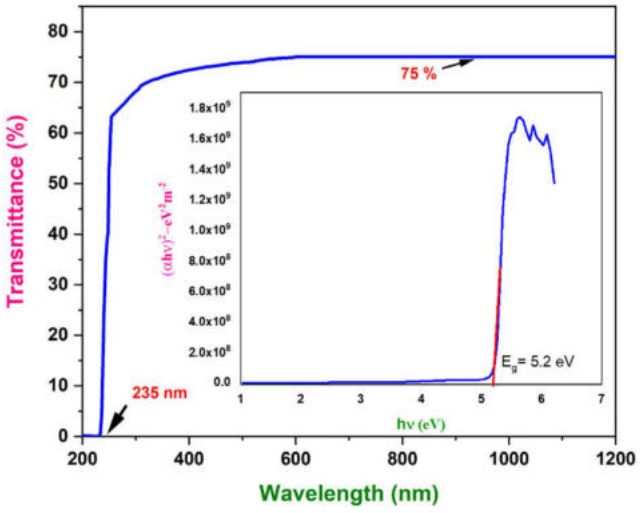

Fig. 14. UV–Vis–NIR transmission spectrum and Tauc plot of IMGA crystal.

3.10. Hyperpolarizability studies

The relationship between the molecular structure and NLO properties can be understood by using theoretical determinations of hyperpolarizability [47,48]. The dipole moment (μ), mean polarizability (α), and first-order hyperpolarizability (β) for IMGA in terms of x, y, and z components have been calculated using the density functional theory (B3LYP/6–311++G(d,p)). The formulas for computing μ, α, β are given by the following reference [24]. The calculated values of IMGA are given in Table 8. It shows the total molecule dipole moment and first-order hyperpolarizability, which are 10.3163 Debye and 0.96 $\times$ 10^{-30} esu, respectively. The dipole moment of the IMGA molecule is 7 times larger than urea, and its first-order hyperpolarizability is 2.5 times larger than urea's (the dipole moments of urea are 1.3732 Debye and 0.3728 $\times$ 10^{-30} esu, respectively, as determined using the B3LYP/6- 311++G(d,p) method). The intramolecular charge transfer caused by the migration of the electron cloud from an electron donor to acceptor groups through the conjugate framework is linked to the large value of hyperpolarizability [49,50], which is a measure of the NLO features of the molecular system.

3.11. UV–Vis-NIR studies

The optical transmittance range and cut-off wavelength are essential factors to customize the material for particular device applications. The majority of uses for single crystals are in optical technology. Using a UV–Vis-NIR spectrophotometer, the UV–Vis-NIR spectrum of IMGA was recorded from 200 to 1200 nm. For the optical transmittance studies, a high-quality, (101) plane cut-and-polished 1 mm thickness wafer was used. Fig. 14 displays the transmittance spectrum of IMGA crystal. It shows that grown crystal has ~75% transmittance from 350 to 1200 nm and this value is enough for blue-light applications and SHG Laser radiation at 1064 nm [51]. The lower cut-off wavelength of the grown crystal is 235 nm. The optical band gap Eg was calculated from Tauc's expression is

$$(\alpha h\upsilon)^2 = A(h\upsilon - E_g)$$

where α is the absorption coefficient, $n = 2$ for direct transition, A is a constant and h is a Plank constant. Fig. 14 the linear part of

Table 8
NLO properties of IMGA molecule.

Dipole moment		Polarizability		First order hyperpolarizability	
μ_x	3.0126	α_{xx}	−36.6050	β_{xxx}	38.4855
μ_y	−9.8666	α_{yy}	−122.9427	β_{yyy}	−156.9134
μ_z	0.0017	α_{zz}	−81.0054	β_{zzz}	−0.0024
μ_{total}	10.3163	α_{xy}	3.9975	β_{xyy}	43.3169
		α_{yz}	−0.0029	β_{xxy}	−36.6993
		α_{zx}	0.0018	β_{xxz}	0.0084
		α_{total}	-1.19×10^{-23} esu	β_{xzz}	−11.3439
		Δ_α	1.45×10^{-23} esu	β_{yzz}	1.2393
				β_{yyz}	0.0157
				β_{xyz}	0.0005
				β_{total}	0.96×10^{-30} esu

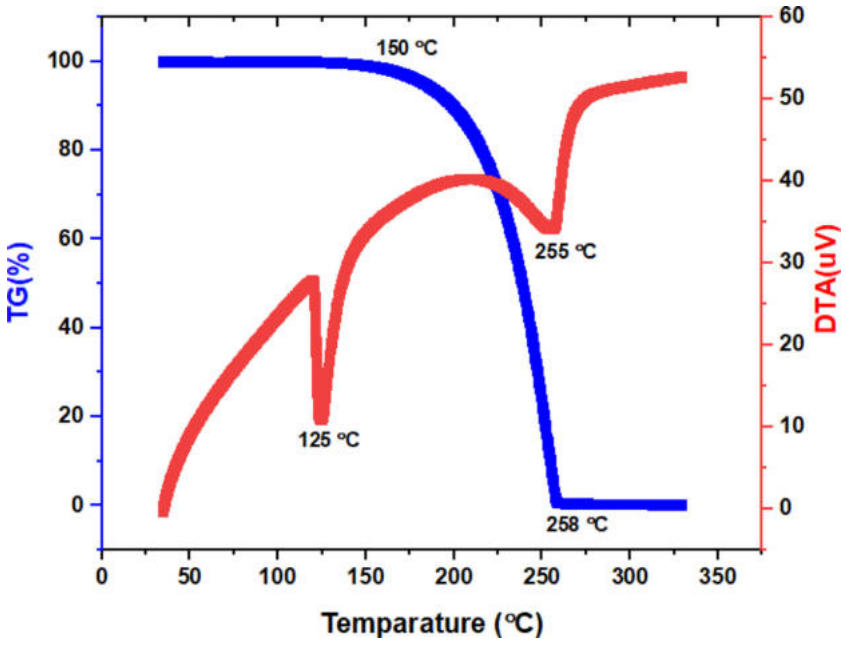

Fig. 15. TG–DTA curve of IMGA crystal.

the curve plotted by $(\alpha h\upsilon)^2$ vs photon energy $(h\upsilon)$ and gives the direct optical band gap energy (Eg) [13]. The estimated E_g value of IMGA crystal is 5.2 eV.

3.12. TG-DTA studies

Simultaneous TG-DTA was performed on the grown IMGA crystals using a PerkinElmer Diamond TG-DTA analyser and a nitrogen environment, the temperature range used was between 30 °C and 400 °C with a 10 °C/min heating rate. Fig. 15 shows the TG/DTA curves of the IMGA crystal. The IMGA crystal is stable up to 150 °C, according to the TG curve, and material weight loss occurs between 150 and 258 °C. The DTA curve clearly displays two endothermic peaks, with the first peak around 125 °C signifying the melting point of the title crystal and the second peak at 255 °C signifying the material's decomposition point. The grown crystal begins to disintegrate after 99% of its weight is eliminated as gaseous products, with the remaining 1% being made up of leftover carbons. The TG-DTA studies confirm that melt growth is also possible to grow the IMGA crystal.

3.13. Dielectric studies

The electrical response of the crystal, which is a key factor in the design of optoelectronic devices [52], can be examined using the dielectric properties of the materials. To measure dielectric properties of IMGA single crystal (2 0 2) plane parallel plates at room temperature using Agilent 4284A Precision LCR METRE in the frequency region 50 Hz - 1 MHz. For a good electrical connection, a silver paste was electrode on the surface of the relevant crystal sample. The dielectric constant and loss of the sample were calculated by the following reference [53]. Fig. 16 depicts how the dielectric constant and dielectric loss (**Inset** Fig. 16) varies with frequency. From 50 Hz to 10,000 Hz, the dielectric constant and loss is greater and rapidly decrease with increasing frequency, continuing up to 1 MHz. After this, it almost remains the same at higher frequencies. The crystal's good optical quality and lack of defects, which is a desirable property for NLO applications [53], is revealed by the low value of dielectric loss and good dielectric constant at high frequencies.

3.14. Z-Scan studies

One of the simplest techniques created by Eric Stryland to measure NLO constants, such as non-linear absorption (NLA) and refraction (NLR), is Z-scan [54]. This method was created for potential uses such as multi-photon polymerization and optical limiting and switching [55,56]. It can simultaneously measure the magnitude and sign of the NLR (n2) and the NLA (β) of the samples. The input parameters for the Z-scan experiment are given in Table 9. The (101) plane cut and polished 1 mm thickness sample was used for the Z-scan experiment. The Z-scan data for the closed aperture

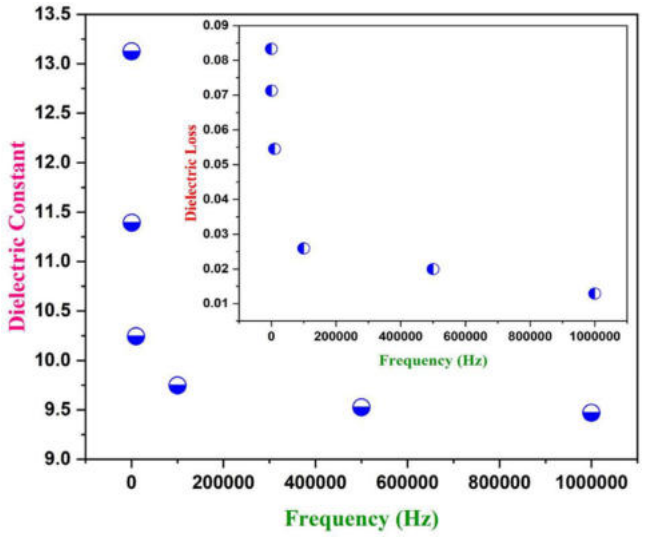

Fig. 16. Dielectric constant and dielectric loss of IMGA crystal at different frequency.

Table 9
Z–scan measurement parameters.

Test Parameters	
Sample thickness (L)	1 mm
Rayleigh length	1.29 mm
Laser beam wavelength (λ)	632.8 nm
Beam radius at the aperture (w_a)	9 mm
Aperture radius (r_a)	2 mm
Laser beam intensity (I_o)	15.31 MW/m^2

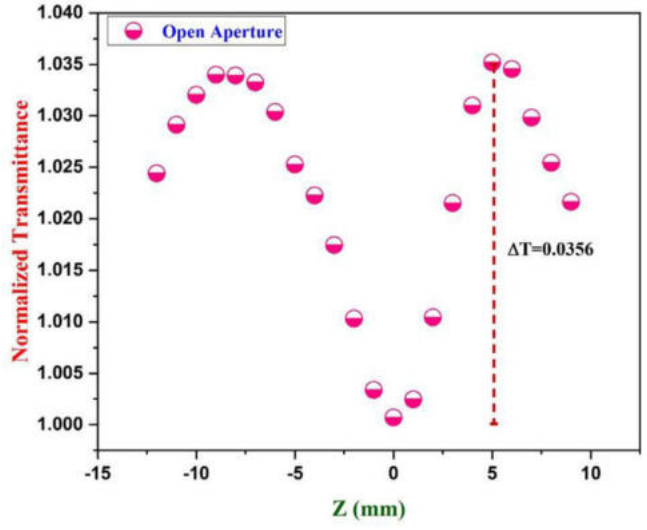

Fig. 17. Open aperture spectrum of IMGA single crystal.

configured for IMGA at the transmission of around 75% is shown in Fig. 17. The valley is followed by a peak-normalized transmittance which is the characteristic of positive nonlinearity. The calculated $\Delta T_{P\text{-}V}$ value is 1.1895. The NLA coefficient (β) is examined and calculated using the open aperture Z-scan spectrum. The open aperture spectrum of the IMGA sample is shown in Fig. 18. It demonstrates that the intensity of transmitted light decreases as the sample gets closer to the focus point, providing conclusive

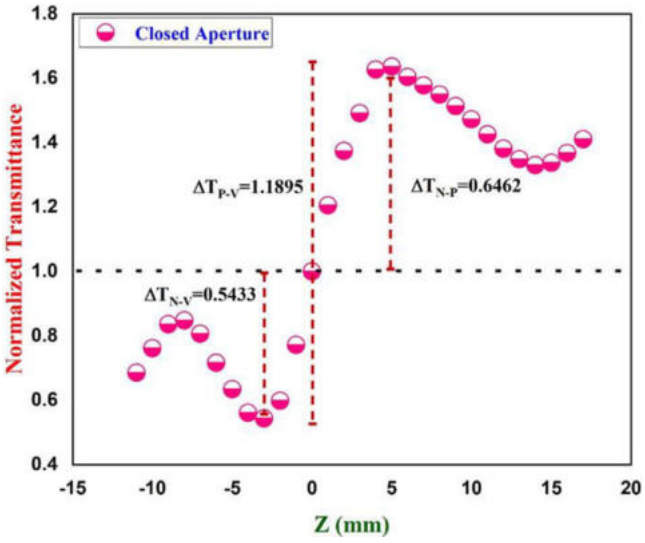

Fig. 18. Closed aperture spectrum of IMGA single crystal.

Table 10
Parameters measured in Z – scan experiment.

Parameters	Calculated values
$\Delta T_{P\text{-}V}$	1.1895
ΔT	0.0356
Linear refractive index at 632.8 nm	1.548
Linear absorption co-efficient (α)	3.07 cm^{-1}
Nonlinear refractive index (n_2)	2.30 × 10^{-12}m^2/W
Nonlinear absorption co-efficient (β)	7.64 × 10^{-6} m/W
Real part of the third-order susceptibility [$Re\ \chi^{(3)}$]	1.395 × 10^{-10}esu
Imaginary part of the third-order susceptibility [Im $\chi^{(3)}$]	2.274 × 10^{-7}esu
Third-order nonlinear optical susceptibility ($\chi^{(3)}$)	2.274 × 10^{-7}esu

proof of the reverse saturable absorption (RSA) phenomenon. The calculated $\Delta T_{P\text{-}V}$ value is 0.0356. Both the NLA coefficient and NLR contribute to the third-order NLO property of the crystal. The formulas for finding third-order NLO and related parameters are given detailed in Ref. [4] and calculated parameters in Z – the scanning experiment are given in Table 10**.** The relatively high value of third-order NLO susceptibility ($\chi^{(3)}$) suggests that grown crystal is suitable for optical limiting-related applications.

4. Conclusion

IMGA crystal has been synthesized and its crystal structure has been confirmed from SCXRD and PXRD studies. The optimized geometric parameters have been theoretically calculated and compared with the experimental data. The presence of proton and carbon was confirmed by ^{1}H and ^{13}CNMR spectra. The bandgap energy of the material is 5.2 eV. The dominant IMIs of the total HS for IMGA molecule are H…H (36.6%) interactions and the proportions of O…H and H…O interactions comprise 52.1% of the total Hirshfeld surface for each molecule. The calculated GCRD such as electronegativity (χ) and electrophilicity index (ω) values are 3.0016 and 1.7875 eV, respectively. The delocalization of IMGA with the transfer of LP(1) N18 → π^*(N17-C19) and LP(2) O2 → π^*(O3-C9) possesses the E(2) of 79.61 and 52.42 Kcal/mol, respectively. The dipole moment of the IMGA molecule is 2.5 times larger than urea, and its first-order hyperpolarizability is 7 times larger than urea. The values of nonlinear RI (n2 = 2.30 × 10^{-12}m^2/W) and 3rd order nonlinear susceptibility (χ3 = 2.274 × 10^{-7}esu) were estimated using Z-scan studies. The

wide bandgap, high dielectric constant, and $\chi 3$ values suggest that the grown crystal is suitable for optoelectronic applications.

Funding

The authors received no funding for this research.

Declaration of Competing Interest

The authors declared no potential conflicts of interest.

CRediT authorship contribution statement

Gino DJ: Formal analysis, Investigation, Data curation, Writing – original draft. **Chinnasami Sidden:** Investigation, Validation, Writing – review & editing. **Rajesh Paulraj:** Conceptualization, Project administration. **H. Marshan Robert:** Validation, Investigation. **S. Ajitha:** Funding acquisition, Supervision, Project administration.

Data availability

Data will be made available on request.

References

[1] C.B. Aakeroy, P.B. Hitchcock, Hydrogen-bonded layers of hydrogentartrate anions: two-dimensional building blocks for crystal engineering, J. Mater. Chem. 3 (1993) 1129–1135.
[2] C. Ji, T. Chen, Z. Sun, Y. Ge, W. Lin, J. Luo, Q. Shi, M. Hong, Bulk crystal growth and characterization of imidazolium L-tartrate (IMLT): a novel organic nonlinear optical material with a high laser-induced damage threshold, Cryst. Eng. Commun. 15 (2013) 2157–2162.
[3] S. Park, O.H. Kwon, S. Kim, S. Park, M.G. Choi, M. Cha, S.Y. Park, D.J. Jang, Imidazole-based excited-state intramolecular proton-transfer materials: synthesis and amplified spontaneous emission from a large single crystal, J. Am. Chem. Soc. 127 (2005) 10070–10074.
[4] S. Chinnasami, R. Paulraj, R. Bhatt, I. Bhaumik, P. Ramasamy, A.K. Karnal, Investigation on the growth rate, crystalline perfection, refractive index, Z-scan and electrical characteristics of Z-cut imidazolium L-tartrate single crystal, Opt. Mater. 108 (2020) 110380.
[5] Y. Sunairi, A. Ueda, J. Yoshida, K. Suzuki, H. Mori, Anisotropic proton conductivity arising from hydrogen-bond patterns in anhydrous organic single crystals, imidazolium carboxylates, J. Phys. Chem. C 122 (2018) 11623–11632.
[6] S.K. Callear, M.B. Hursthouse, T.L. Threlfall, A systematic study of the crystallisation products of a series of dicarboxylic acids with imidazole derivatives, Cryst. Eng. Comm. 12 (2010) 898–908.
[7] V. Krishnakumar, J. Jayaprakash, S. Boobas, M. Komathi, Synthesis, growth, optical and anisotropic mechanical behaviour of organic nonlinear optical imidazolium 2-chloro-4-nitrobenzoate single crystals, Eur. Phys. J. Plus 131 (2016) 1–11.
[8] S. Horike, D. Umeyama, S. Kitagawa, S. Ion, Conductivity and transport by porous coordination polymer and metal–organic frameworks, Acc. Chem. Res. 46 (2013) 2376–2384.
[9] J.C. MacDonald, P.C. Dorrestein, M.M. Pilley, Design of supramolecular layers via self-assembly of imidazole and carboxylic acids, Cryst. Growth. Des. 1 (2001) 29–38.
[10] J. Fuller, R.T. Carlin, L.J. Simpson, T.E. Furtak, Incorporation of imidazolium cations into an enantiomeric tartrate host lattice: designing new nonlinear optical materials, Chem. Mater. 7 (1995) 909–919.
[11] K. Pogorzelec-Glaser, Cz. Pawlaczyk, A. Pietraszko, E. Markiewicz, Electrical conductivity in new imidazolium salts of dicarboxylic acids, Mater. Sci. Poland 24 (2006) (2006) 1.
[12] M.J. Frisch, et al., Gaussian 09, Revision C. 02, Gaussian, Inc., Wallingford, CT, 2004.
[13] A.S. Raj, S. Chinnasami, R. Paulraj, Investigation on the growth, structural, vibrational, SHG behaviour and DFT studies of imidazolium hydrogen succinate single crystal, Chem. Pap. 76 (2022) 5429–5446.
[14] K. Meena, K. Muthu, V. Meenatchi, M. Rajasekar, G. Bhagavannarayana, S.P. Meenakshisundaram, Growth, crystalline perfection, spectral, thermal and theoretical studies on imidazolium L-tartrate crystals, Spectrochim. Acta, Part A 124 (2014) 663–669.
[15] R.M. Jauhar, P. Era, V. Viswanathan, P. Vivek, G. Vinitha, D. Velmurugan, P. Murugakoothan, Crystal structure, molecular packing, FMO, NBO, nonlinear optical and optical limiting properties of an organic imidazolium diphenylacetate diphenylacetic acid single crystal, New J. Chem. 42 (2018) 2439–2449.
[16] S. Chinnasami, R. Paulraj, P. Ramasamy, Bulk crystal growth, spectroscopic, Hirshfeld surface analysis, physicochemical and quantum chemical investigations on 2-ethylimidazolium D-tartrate single crystal, J. Mol. Struct. 1238 (2021) 130448.
[17] S.K. Wolff, D.J. Grimwood, J.J. McKinnon, M.J. Turner, D. Jayatilaka, M.A. Spackman, Crystal explorer, Version 3.1, University of Western Australia, 2012.
[18] M.J. Frisch, G.W. Trucks, H.B. Schlegel, G.E. Scuseria, M.A. Robb, J.R. Cheeseman, G. Scalmani, V. Barone, B. Mennucci, G.A. Petersson, H. Nakatsuji, M. Caricato, X. Li, H.P. Hratchian, A.F. Izmaylov, J. Bloino, G. Zheng, J.L. Sonnenberg, M. Hada, M. Ehara, K. Toyota, R. Fukuda, J. Hasegawa, M. Ishida, T. Nakajima, Y. Honda, O. Kitao, H. Nakai, T. Vreven, J.A. Montgomery, J.E. Peralta, F. Ogliaro, M. Bearpark, J.J. Heyd, E. Brothers, K.N. Kudin, V.N. Staroverov, R. Kobayashi, J. Normand, K. Raghavachari, A. Rendell, J.C. Burant, S.S. Iyengar, J. Tomasi, M. Cossi, N. Rega, J.M. Millam, M. Klene, J.E. Knox, J.B. Cross, V. Bakken, C. Adamo, J. Jaramillo, R. Gomperts, R.E. Stratmann, O. Yazyev, A.J. Austin, R. Cammi, C. Pomelli, J.W. Ochterski, R.L. Martin, K. Morokuma, V.G. Zakrzewski, G.A. Voth, P. Salvador, J.J. Dannenberg, S. Dapprich, A.D. Daniels, O. Farkas, J.B. Foresman, J.V. Ortiz, J. Cioslowski, D.J. Fox, Gaussian 09, Gaussian, Inc., Wallingford CT, 2009.
[19] K.B. Wiberg, Basis set effects on calculated geometries: 6-311++ G** vs. aug-cc-pVDZ, J. Comput. Chem. 25 (2004) 1342–1346.
[20] M. Appell, J.L. Willett, F.A. Momany, DFT study of α-and β-D-mannopyranose at the B3LYP/6-311++ G** level, Carbohydr. Res. 340 (2005) 459–468.
[21] A. Frisch, A.B. Nielson, A.J. Holder, GAUSS VIEW User's Manual, Gaussian Inc., Pittsburgh PA, 2000.
[22] E.D. Glendening, A.E. Reed, J.E. Carpenter, F. Weinhold, in: Nbo Version 3, 1, TCI (University of Wisconsin, Madison, 1998, p. 65.
[23] SpectraBase; SpectraBase Compound ID=2hThxt1mJSH Spectra Base Spectrum ID=JPMbdh6eNNY, John Wiley & Sons, Inc, 2021. https://spectrabase.com/spectrum/JPMbdh6eNNY.
[24] S. Chinnasami, S. Chandran, R. Paulraj, P. Ramasamy, Structural, vibrational, Hirshfeld surfaces and optical studies of nonlinear optical organic imidazolium L-tartrate single crystal, J. Mol. Struct. 1179 (2019) 506–513.
[25] J. Mohan, Organic Spectroscopy: Principles and Applications, Alpha Science Int'l Ltd., United Kingdom, 2004.
[26] B.H. Stuard, Infrared Spectroscopy: Fundamentals and Applications, Spectroscopy, Wiley online library, 2004.
[27] M. Ibrahim, A. Nada, D.E. Kamal, Density functional theory and FTIR spectroscopic study of the carboxyl group, Indian J. Pure Appl. Phys. 43 (2005) 911–917.
[28] P.R. Spackman, M.J. Turner, J.J. McKinnon, S.K. Wolff, D.J. Grimwood, D. Jayatilaka, M.A. Spackman, CrystalExplorer: a program for Hirshfeld surface analysis, visualization and quantitative analysis of molecular crystals, J. Appl. Crystallogr. 54 (2021) 1006–1011.
[29] S. Chinnasami, M. Manikandan, S. Chandran, R. Paulraj, P. Ramasamy, Growth, Hirshfeld surfaces, spectral, quantum chemical calculations, photoconductivity and chemical etching analyses of nonlinear optical p-toluidine p-toluenesulfonate single crystal, Spectrochim. Acta A Mol. Biomol. Spectrosc. 206 (2019) 340–349.
[30] J.J. McKinnon, M.A. Spackman, A.S. Mitchell, Hirshfeld surfaces: a new tool for visualizing and exploring molecular crystals, Chem. Eur. J. 4 (1998) 2136–2141.
[31] D.J. Gino, C. Sidden, R. Paulraj, S. Ajitha, H.H. Somaily, Investigation on the crystal growth, physicochemical, quantum chemical, and third harmonic generation properties of diisopropylammonium hydrogen phthalate single crystal, J. Mater. Sci. Mater. Electron. 33 (2022) 1–19.
[32] D. Douche, Y. Sert, S.A. Brandán, A.A. Kawther, B. Bilmez, N. Dege, A. El Louzi, K. Bougrin, K. Karrouchi, B. Himmi, 5-((1H-imidazol-1-yl) methyl) quinolin-8-ol as potential antiviral SARS-CoV-2 candidate: synthesis, crystal structure, Hirshfeld surface analysis, DFT and molecular docking studies, J. Mol. Struct. 1232 (2021) 130005.
[33] S.K. Seth, D. Sarkar, A. Roy, T. Kar, Insight into supramolecular self-assembly directed by weak interactions in acetophenone derivatives: crystal structures and Hirshfeld surface analyses, Cryst. Eng. Comm. 13 (2011) 6728–6741.
[34] K. Sambathkumar, S. Jeyavijayan, M. Arivazhagan, Electronic structure investigations of 4-aminophthal hydrazide by UV–visible, NMR spectral studies and HOMO–LUMO analysis by ab initio and DFT calculations, Spectrochim. Acta A Mol. Biomol. Spectrosc. 147 (2015) 124–138.
[35] P.B. Nagabalasubramanian, M. Karabacak, S. Periandy, FT-Raman FT-IR, ab initio, D.F.T. structural, vibrational frequency and HOMO–LUMO analysis of 1-naphthaleneacetic acid methyl ester, Spectrochim. Acta A Mol. Biomol. Spectrosc. 82 (2011) 169–180.
[36] V. Balachandran, A. Janaki, A. Nataraj, Theoretical investigations on molecular structure, vibrational spectra, HOMO, LUMO, NBO analysis and hyperpolarizability calculations of thiophene-2-carbohydrazide, Spectrochim. Acta A Mol. Biomol. Spectrosc. 118 (2014) 321–330.
[37] N. Dege, O. Tamer, M. Yaman, A. Bas¸oglu, ˘.D. Avcı, Y. Atalay, Crystallographic, spectroscopic, thermal, optical investigations and density functional theory calculations for novel Co (II) and Mn (II) complexes, Appl. Phys. A 127 (2021) 1–17.
[38] L. Li, T. Cai, Z. Wang, Z. Zhou, Y. Geng, T. Sun, Study on molecular structure, spectroscopic investigation (IR, Raman, and NMR), vibrational assignments and HOMO–LUMO analysis of L-sodium folinate using DFT: a combined experimental and quantum chemical approach, Spectrochim. Acta A: Mol. Biomol. Spectrosc. 120 (2014) 106–118.
[39] S. Omar, M. Shkir, M.A. Khan, Z. Ahmad, S. AlFaify, A comprehensive study on molecular geometry, optical, HOMO-LUMO, and nonlinear properties of 1, 3-diphenyl-2-propen-1-ones chalcone and its derivatives for optoelectronic applications: a computational approach, Optik (Stuttg) 204 (2020) 164172.

[40] S. Ramalingam, S. Periandy, M. Karabacak, N. Karthikeyan, Spectroscopic (FT-IR/FT-Raman) and computational (HF/DFT) investigation and HOMO/LUMO/MEP analysis on 2-amino-4-chlorophenol, Spectrochim. Acta A Mol. Biomol. Spectrosc. 104 (2013) 337–351.
[41] K. Carthigayan, S. Xavier, S. Periandy, HOMO–LUMO, UV, NLO, NMR and vibrational analysis of 3-methyl-1-phenylpyrazole using FT-IR, FT-RAMAN FT-NMR spectra and HF-DFT computational methods, Spectrochim. Acta A Mol. Biomol. Spectrosc. 142 (2015) 350–363.
[42] P. Politzer, P.R. Laurence, K. Jayasuriya, Molecular electrostatic potentials: an effective tool for the elucidation of biochemical phenomena, Environ. Health Perspect 61 (1985) 191–202.
[43] M. Prasath, M. Govindammal, B. Sathya, Spectroscopic investigations (FT-IR & FT-Raman) and molecular docking analysis of 6-[1-methyl-4-nitro-1H-imidazol-5-yl) sulfonyl]-7H-purine, J. Mol. Struct. 1146 (2017) 292–300.
[44] S. Madhankumar, P. Muthuraja, M. Dhandapani, Molecular properties, crystal structure, Hirshfeld surface analysis and computational calculations of a new third-order NLO organic crystal, 2-aminopyridinium benzilate, J. Mol. Struct. 1181 (2019) 118–130.
[45] M. Manikandan, P. Rajesh, P. Ramasamy, Crystal growth, structural, optical, vibrational analysis, Hirshfeld surface, and quantum chemical calculations of 1, 3, 5-triphenylbenzene single crystal, J. Mol. Struct. 1195 (2019) 659–669.
[46] J. Ye, L. Wang, X.Pan H.Wang, H. Xie, Y. Qiu, Efficient enhancement of second-order nonlinear optical response by complexing metal cations in conjugated 7-substituted coumarin, J. Orgel. 47 (2017) 152–161.
[47] N. Dege, O. Tamer, M. Şimşek, D. Avcı, M. Yaman, A. Başoğlu, Y. Atalay, Experimental and theoretical approaches on structural, spectroscopic (FT-IR and UV–Vis), nonlinear optical, and molecular docking analyses for Zn (II) and Cu (II) complexes of 6-chloropyridine-2-carboxylic acid, Appl. Organomet. Chem. 36 (2022) e6678.
[48] O. Tamer, N. Dege, D. Avcı, Y. Atalay, I.O. İlhan, M. Çadır, Synthesis, structural and spectroscopic evaluations and nonlinear optical properties of 3, 5-bis (4 methoxyphenyl)-4, 5-dihydro-1H-pyrazole-1-carbothioic O-acid, Spectrochim. Acta A Mol. Biomol. Spectrosc. 137 (2015) 1387–1396.
[49] P. Agarwal, N. Choudhary, A. Gupta, P. Tandon, Density functional theory studies on the structure, spectra (FT-IR, FT-Raman, and UV) and first order molecular hyperpolarizability of 2-hydroxy-3-methoxy-N-(2-chloro-benzyl)-benzaldehyde-imine: comparison to experimental data, Vib. Spectrosc. 64 (2013) 134–147.
[50] M.R. Albayati, S. Kansız, N. Dege, S. Kaya, R. Marzouki, H. Lgaz, R. Salghi, I.H. Ali, M.M. Alghamdi, I.M. Chung, Synthesis, crystal structure, Hirshfeld surface analysis and DFT calculations of 2-[(2, 3-dimethylphenyl) amino]-N'-[(E)-thiophen-2-ylmethylidene] benzohydrazide, J. Mol. Struct. 1205 (2020) 127654.
[51] S. Anbarasu, G. Bhagavannarayana, N. Vijayan, P.A. Devarajan, Growth and characterization of a new organic nonlinear optical crystal: vanillylideneaniline, Optik (Stuttg) 125 (2014) 4295–4301.
[52] S. Kang, D. Lee, J. Kim, A. Capasso, H.S. Kang, J.W. Park, C.H. Lee, G.H. Lee, 2D semiconducting materials for electronic and optoelectronic applications: potential and challenge, 2D Mater. 7 (2020) 022003.
[53] M.L. Caroline, R. Sankar, R.M. Indirani, S. Vasudevan, Growth, optical, thermal and dielectric studies of an amino acid organic nonlinear optical material: L-Alanine, Mater. Chem. Phys. 114 (2009) 490–494.
[54] M. Sheik-Bahae, A.A.A. Said, T.H. Wei, D.J. Hagan, E.W. Van Stryland, Sensitive measurement of optical nonlinearities using a single beam, IEEE J. Quant. Electron. 26 (1990) 760–769.
[55] C.R. Mendonca, T. Baldacchini, P. Tayalia, E. Mazur, Reversible birefringence in microstructures fabricated by two-photon absorption polymerization, J. Appl. Phys. 102 (2007) 013109–013113.
[56] K.W. DeLong, K.B. Rochford, G.I. Stegeman, Effect of two-photon absorption on all-optical guided-wave devices, Appl. Phys. Lett. 55 (1989) 1823–1825.

Biological Forum – An International Journal **15(4): 590-597(2023)**

ISSN No. (Print): 0975-1130
ISSN No. (Online): 2249-3239

Studies on the Investigation of Anti-Oxidant and Cellular Toxicity on L929 Cell Line of *Andrographis paniculata* and its Derivative of Silver and Gold Nanoparticles

M. Shirley Navis[1]* and Ragel Mabel Saroja[2]
[1]Ph.D. Research Scholar,
Scott Christian College (Autonomous), Nagercoil-04, (Tamilnadu), India.
[2]Associate Professor, Department of Chemistry,
Scott Christian College (Autonomous), Nagercoil-04, (Tamilnadu), India.

(Corresponding author: M. Shirley Navis)*
(Received: 08 February 2023; Revised: 13 March 2023; Accepted: 18 March 2023; Published: 20 April 2023)
(Published by Research Trend)

ABSTRACT: The current pharmaceutical industry is increasingly turning to plant-based multi-potential bioactive compounds to combat a variety of diseases and pathological conditions due to the consequences of administrating synthetic drugs. To Avoid back reflection of synthetic drugs, researchers are focusing on natural derivatives guided from traditional medical practices. Plants are playing vital role in nutritional and disease control aspects in traditional era. Terrestrial resources contain a vast array of medicinally valuable plants that have traditionally been used to treat a wide range of diseases, including hepatoprotective, anti-inflammatory, antibacterial, anti-cancer, and antidiabetic properties. Similarly, the study plant *Andrographis paniculata* demonstrated significant medicinal properties; thus, the potential activity of a leaf ethanolic extract of *A. paniculata*, diethyl phthalate purified from the crude ethanolic extract, and their modified metal (Silver and Gold) nanoparticles against free radicals, namely DPPH and phosphomolebdenum assays. In addition, the study samples were subjected to an MTT assay to assess cellular toxicity in comparison to the L929 cell line. The results showed that the promising drug carrier system of diethyl phthalate silver nanoparticles (DPAgNPs) exhibited lower toxicity and higher anti-oxidant activity.

Keywords: *Andrographis paniculata,* Diethyl phthalate, Silver and gold nanoparticles, DPPH, Phospohomolebdenum and Cytotoxicity.

INTRODUCTION

Countless plant-based products, such as herbal teas, nutritional supplements, health meals, and other goods, are readily available today (Phillips and Meilleur 1998). Distinct medical traditions are practised by various cultural and ethnic groups (Leslie and Young 1992). In underdeveloped nations, where 65 to 80 percent of the world's population resides, plant products are their primary source of healthcare (Farnsworth *et al*., 1985; Awoyemi *et al*., 2012). Ayurveda has been demonstrated to be one of the oldest medical systems that is still in use today, both in India and around the world. Many individuals think natural treatments are safer than synthetic medications. Individualized therapies may incorporate nutritional, physical activity, and lifestyle factors as well as proprietary molecules or plant components (Sharma and Mujundar 2003). There has been a remarkable return of interest in medicine and classical pharmacopoeia despite substantial advancements in contemporary medicine. Perumal and Gopalakrishnakone (2008) explored plant-based medications, which significantly improved on already available therapies. Plants continue to play a key role in the control of diabetes, particularly in much less developed countries where the bulk of the population has little resources and no access to contemporary therapy. Alternative diabetes therapies, such as those based on plants, are becoming more and more popular in industrialised nations due to the drawbacks of taking insulin and oral hypoglycemic medications (Marles and Farnsworth 1994). In India, where more than 30 million individuals have the condition, diabetes is on the increase. Numerous members of society are impacted by undiagnosed diabetes. Both diabetes screening and the streamlining of diagnostic processes have become crucial. The two most prevalent kinds of diabetes are Type-1 and Type-2 (Gupta *et al*., 2014; Wang *et al.,* 2001). Phenolic compounds are a significant category of the plant secondary metabolites that have been found to have antioxidant properties. There are several findings on how phenolic chemicals affect the antioxidant capacity of various plant species (Cai *et al*., 2004). Diverse pharmacological effects of *Andrographis paniculata* exist, some of which include anti-cancer, anti-diarrheal, and anti-hepatitis (Md. Sanower Hossain *et al*. (2014). *A. paniculata* extracts show hepatoprotective qualities, antihypertensive

effects, and lower plasma angiotensin converting enzyme (ACE) activity and renal lipid peroxidation (Akbar, 2011). Besides, they have antimicrobial, anti-inflammatory, antioxidant, and hypoglycemic effects (Zhang and Tan 2000). In an effort to discover a treatment for conditions like rheumatoid arthritis and ulcerative colitis that are brought on by oxidative stress and infections, Umadevi and Kamalam (2014) at the University of Bristol investigated *A. paniculata*. They are looking at the phytochemical composition and antioxidant capacities of the plant. Similar to this, 10% methanolic SLE showed enhanced antioxidant activity, which was responsible for 53.94 g/ml DPPH activity and 44.94% suppression of nitric oxide activity (Uthirapandi *et al*., (2021). Penicillin has a wide range of possible uses, including as an anti-microbial, cytotoxic, anti-protozoan, and immunostimulant, according to a review by Okhuarobo *et al*. (2014). Andrographolide, the primary active ingredient, has a variety of biological effects, including hepatoprotective, anti-inflammatory, antibacterial, anti-cancer, and antidiabetic ones (Jarukamjorn and Nemoto 2008). Researchers suggest that andrographolide be structurally modified in order to acquire diverse leads due to the outstanding diversity of these biological functions. Numerous andrographolide compounds have surfaced in recent decades, and their pharmacological properties have also been examined. There haven't been many researches that thoroughly summaries or analyze *A. paniculata* and its derivatives, nevertheless. As a result, this study gives comprehensive information about the pharmacological activity of *A. paniculata* and its main ingredient andrographolide in an effort to advance the trends of research on andrographolide (Jayakumar *et al*., 2013). Antioxidant defences are strengthened by andrographolide. By scavenging free radicals, it exerts direct action. It further causes indirect interference by preserving mitochondrial integrity, preventing pro-oxidant enzyme activity, and/or activating antioxidant enzymes. Keep in mind that the control of the antioxidant defense system involves the transcription factor Nrf2. As a result, andrographolide's regulation of Nrf2 is important for controlling the redox system (Li *et al*., 2018; Tan *et al*., 2018; Yan *et al*., 2018).

MATERIAL AND METHODS

Sample Preparation. Around 50 g of powdered *Andrographis paniculata* was taken into fresh extract cloth and bagged into extraction apparatus. The system was placed on the heating mantle at 40°C and the sample with reflux condenser tube was placed over the solvent collector with air tightly. The extraction system was started with 500 ml ethanol as extraction solvent for 24 hours. After extraction the solvent was transferred to fresh 500 ml conical flask, filter the extract and stored at 4 °C for further analysis. Diethyl phthalate was partially purified from the crude extract of *A. paniculata* using column chromatography and has been characterised spectrally. From the diethyl phthalate chromatographic fraction, silver and gold nanoparticles were synthesised using ascorbic acid as a reducing agent and subjected to spectral and morphological characterization.

Anti-Oxidant Property

DPPH radical scavenging activity. The free radical scavenging activity of the fractions was measured in vitro by the 2, 2-diphenyl-1-picrylhydrazyl (DPPH) assay according to the standard method (Brand-Williams *et al.,* 1995). The stock solution was prepared by dissolving 24 mg of DPPH in 100 ml of methanol stored at 4–20 °C. About 4 ml of various concentrations of samples (20, 40, 60, 80, and 100 g/mL) were mixed with 1 ml of methanolic solution containing DPPH radicals, resulting in a final concentration of DPPH of 0.2 mM. The mixture was shaken vigorously and left to stand for 30 minutes, and the absorbance was measured at 517 nm. Ascorbic acid was used as a control. The percentage of DPPH decolorization in the sample was calculated according to the equation. The control was prepared without any sample, and scavenging activity was estimated based on the percentage of DPPH radicals scavenged using the following equation:

% of inhibition = [(control OD–sample OD)/(control OD)]×100

Total antioxidant activity. Each test tube contained 3 mL of distilled water and 1 mL of Molybdate reagent solution, as well as 20-100 µg/mL of *Andrographis paniculata* extract, Diethyl phthalate (DP), DP silver nanoparticles (DPAgNPs), and DP gold nanoparticles (DPAuNPs). These tubes were kept incubating at 95 ºC for 90 min. After incubation, these tubes were normalized to room temperature for 20–30 min, and the absorbance of the reaction mixture was measured at 695 nm. The percentage of inhibition values from samples was calculated for each extract. Ascorbic acid was used as a positive reference standard. The PM assay is based on the reduction of phosphate-Mo (VI) to phosphate-Mo (V) by the sample and the subsequent formation of a bluish-green phosphate/Mo (V) complex at an acidic pH. The phosphomolybdenum method is routinely applied in the laboratory to evaluate the total antioxidant capacity of plant extracts (Prieto *et al*., 1999).

Cellular Cytotoxicity on L929 Cell line by MTT assay. This assay was performed based on the assessment of reduction of the yellow colored water soluble tetrazolium dye MTT to formazan crystals (MTT Cell Proliferation Assay Instruction Guide). Mitochondrial lactate dehydrogenase produced by live cells reduces MTT to insoluble formazan crystals formed in assay mixture. Seed 200µl cell suspension in a 96-well plate at required cell density (20,000 cells per well), without the test agent. Allow the cells to grow for about 24 hours. Add appropriate concentrations of the test samples (Diethyl phthalate, DPAgNPs and DPAuNPs) incubate the plate for 24hrs at 37°C in a 5% CO_2 atmosphere. After the incubation period, takeout the plates from incubator and remove spent media and add MTT reagent to a final concentration of 0.5mg/mL of total volume. Wrap the plate with aluminium foil to avoid exposure to light. Return the plates to the incubator and incubate for 3 hours. (Note: Incubation time varies for different cell lines. Within one

experiment, incubation time should be kept constant while making comparisons). Remove the MTT reagent and then add 100µl of solubilisation solution (DMSO). Gentle stirring in a gyratory shaker will enhance dissolution. Occasionally, pipetting up and down may be required to completely dissolve the MTT formazan crystals especially in dense cultures. Read the absorbance on a spectrophotometer or an ELISA reader at 570 nm wavelength. % Cell viability is calculated using below formula:

% cell viability=[Mean abs of treated cells/Mean abs of Untreated cells] × 100

Statistical Analysis. The obtained data were interpreted and calculated as Mean, Standard deviation and ANOVA using IBM SPSS Statistical Software and represented the data in tables as well as graphs.

RESULT AND DISCUSSION

Phytochemical Screening

Anti-Oxidant Activity

DPPH Scavenging Assay. The study samples (*A. paniculata*, Diethyl phthalate, DPAgNPs and DPAgNps) were subjected to investigate the scavenging activity against 2-diphenyl-1-picrylhydrazyl (DPPH) and the scavenging effects were analyzed and calculated statistically. Among the sample Diethyl phthalate silver nanoparticles (DPAgNPs) were described in Table and Figure: 1 as higher scavenging activity 60.36 % at 100 µg/mL concentration while *A.paniculata* showed 44.94 % at 100 µg/mL. However, Diethyl phthalate and DP gold nanoparticles exhibited quite lower scavenging effect as 16.42 % and 20.83 % at 100 µg/mL concentration. The one-tailed ANOVA was performed and showed insignificance of activity among the sample at p-value equals 1.738 (1.738 > p 0.005) greater than α value of 0.005 (Table and Fig. 2).

Total Anti-oxidant Activity. Total anti-oxidant property can be determined by analyzing the reducing activity of phosphate-Mo (VI) to phosphate Mo (V) was measured at 695 nm. In table and Figure: 3 Higher reducing property was shown in Diethyl phthalate silver nanoparticle (DPAgNPs) as 83.64 % at the concentration of 100 µg/mL while, DP gold nanoparticle exhibited lesser activity 14.29 % at 100 µg/mL. In other hand, Diethyl phthalate revealed 57.56 % and *A.paniculata* has 34.78 % of reducing activity at 100 µg/mL. The data of total anti-oxidant property was far away to significant at 0.005 level (1.088 > p 0.005) showed in Table and Fig. 4.

Assessment of Cellular Cytotoxicity by MTT Assay. MTT assay is a colorimetric assessment based on the reduction of the yellow colored water soluble tetrazolium dye MTT to formazan crystals by mitochondrial lactate dehydrogenase produced by live cells which in turn represented the percentage of cellular cytotoxicity of L929 cell line. Among the sample group, DP gold nanoparticle showed 87.9 % cytotoxicity to the cell line at the concentration of 100 µg/mL. While, diethyl phthalate and DPAgNPs exhibited 90.13 and 89.68 % of toxicity at 100 µg/mL in Table 5 and Fig. 7 and 8. This revealed the content of concentration depending cellular toxicity against L929 cell line. The toxicity of study samples were analyzed through one-tailed ANOVA and the value showed the significance at p 0.005 and there is no significant difference between the means of any pair (Table 6 and Fig. 5 and 6).

DISCUSSION

The activities of catalase, superoxide dismutase, and glutathione S transferase are significantly increased when the aqueous extract of *A. paniculata* is administered orally at a variety of dosages. It highlights the antioxidant properties of the aqueous extract of AP, which may contribute to the anticarcinogenic effect by lowering oxidative stress (Verma and Vinayak 2008). According to a study, the antioxidant activity of an *Andrographis paniculata* aqueous extract was higher than that of an ethanol extract. The aqueous extract has a radical scavenging activity of 66.8% at 50 µg/mL compared to 57.8% in the ethanol extract (Mussard *et al*., 2019). Methanolic plant extracts were most effective in scavenging DPPH free radicals and H_2O_2 radicals, with 50% inhibition at concentrations of 333.34 µg/ml and 398.12 µg/ml, respectively (Sinha and Raghuwanshi 2020). The aqueous stem extract (4.42 µg/mL) and ethanolic stem extract (6.84 µg/mL) had the lowest IC50 values, respectively. As a result, the aqueous extract of stem is the most effective in neutralising free radicals produced by the oxidation of lipids, proteins, and nucleic acids (Polash *et al*., 2017). The results of the present research conducted by Khan *et al.* (2020) showed that andrographolide decreased DLD1 cells ability to divide in a concentration- and time-dependent way. Through nuclear condensation, phosphatidylserine externalisation, and caspase-3 activation, andrographolide triggered apoptosis. Additionally, it increased the levels of cellular ROS, which were linked to the activation of apoptosis in DLD1 cells. Additionally, andrographolide showed synergistic efficacy against DLD1 cells when combined with 5-FU and PTX. According to methodology, plant component, and type of dietary supplement, antioxidant activity ranged from 503.36 to 6164.09 µmol TE/100 g d.m. when tested using the FRAP, CUPRAC, and DPPH procedures (Marzanna Kurzawa *et al.,* 2015). According to research on the anti-oxidant properties of *A. paniculata* ethanolic leaf extract, diethyl phthalate, DPAgNPs, and DPAuNPs against DPPH radicals and phosphomolebdenum, DPAgNPs has shown remarkable anti-oxidant activity at 100 µg/mL concentration, and the IC 50 value was 8.93 µg/mL for DPPH scavenging and 35.13 µg/mL for reducing phosphomolebdenum. Diethyl phthalate is an oily, colourless liquid with no odour or flavour. It can be found in toothbrushes, car components, toys, tools, cosmetics, aspirin, plastics, pesticides, and food packaging (World Health Organization, 2003). These findings imply that DEP exposure may cause sperm effects, hepatic effects, developmental effects, and androgen-independent male reproductive toxicity, with some indications of female reproductive toxicity. To thoroughly analyse these results and boost trust in this database, more study is required (Weaver *et al*., 2020). The growth of human

HaCaT keratinocytes in cell culture was significantly inhibited by andrographolide at 31.25 g/mL (90 M). To the best of our knowledge, this is the first time andrographolide from *A. paniculata* has been documented to have anti-proliferative effects. According to OECD test guideline No. 420, *A. paniculata* was evaluated. The standardised FTLEE of *A. paniculata* was given orally to mice in four groups, two of each sex (0, 300, 2000, or 5000 mg/kg BW). Body weight, poisoning symptoms, and/or death were tracked for 14 days after therapy. Animals were put to death at day 15, their internal organs were severely examined, and blood samples were taken for haematological and clinical biochemistry tests. The findings demonstrated that all of the treated animals lived, and no obvious side effects were noticed over the course of the trial. Extensive necropsy examination of all the standardised FTLEE-treated animals showed no lesions in any organs. Despite the fact that substantial changes in BUN, lymphocytes, neutrophils, hematocrit, and haemoglobin were seen, these changes were not harmful side effects of the therapy. Therefore, we came to the conclusion that there are no significant acute toxicological effects from a single oral administration of the standardised FTLEE of *A. paniculata* with an upper fixed dosage of 5000 mg/kg BW (Worasuttayangkurn *et al.*, 2019). Assessment of cellular toxicity of study samples such as *A. paniculata*, diethyl phthalate, DPAgNPs, and DPAuNPs showed minimal toxicity, while a DP gold nanoparticle showed 87.9% cytotoxicity to the cell line at a concentration of 100 µg/mL. While diethyl phthalate and DPAgNPs exhibited 90.13 and 89.68% of their toxicity at 100 µg/mL in L929 (mouse fibroblast cell line).

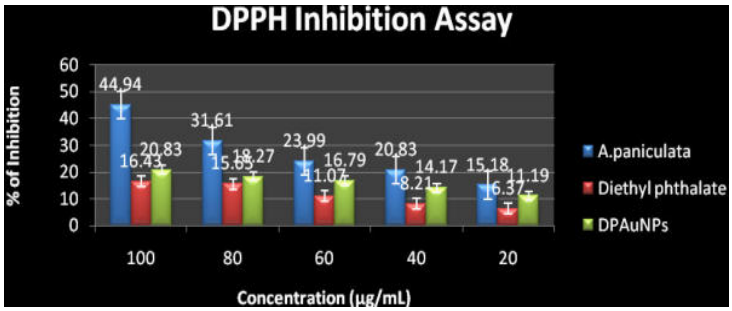

Fig. 1. Inhibitory percentage of study samples against DPPH radicals.

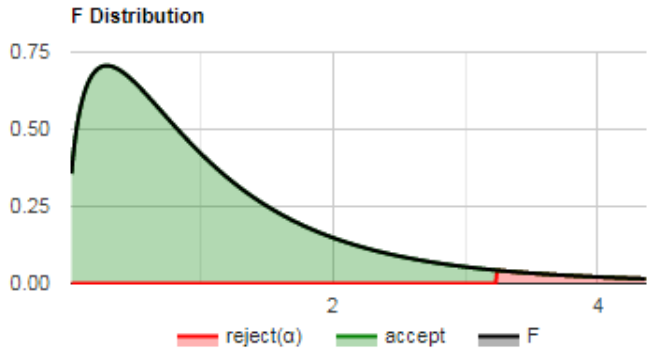

Fig. 2. One-tailed ANOVA of F-distribution of Sample groups

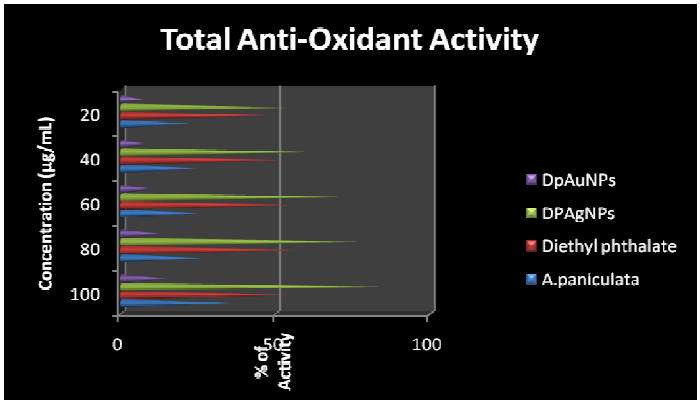

Fig. 3. Total Anti-oxidant activity by Reduction of Phosphomolebdenum

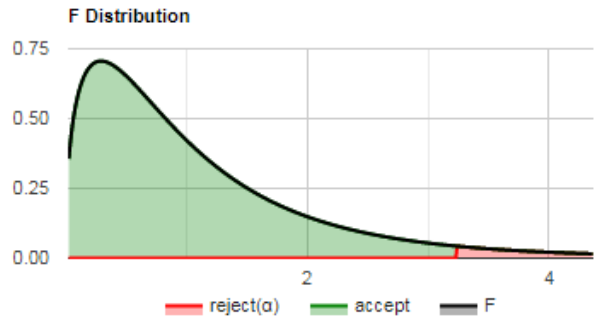

Fig. 4. One-tailed ANOVA of F-distribution of Sample groups.

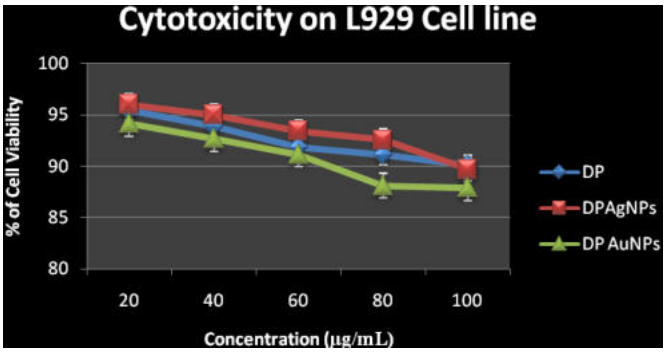

Fig. 5. Cellular toxicity effect of study samples on L929 cell line by MTT assay.

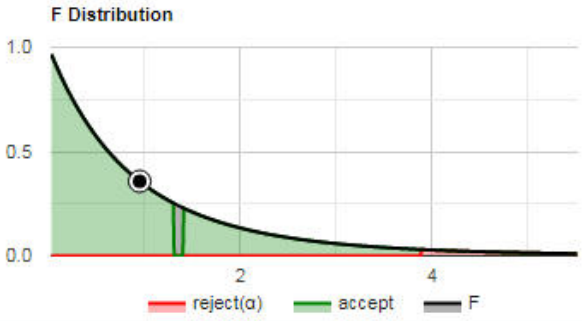

Fig. 6. One-tailed ANOVA of F-distribution of Sample groups for Cytotoxicity effects on L929 cell line.

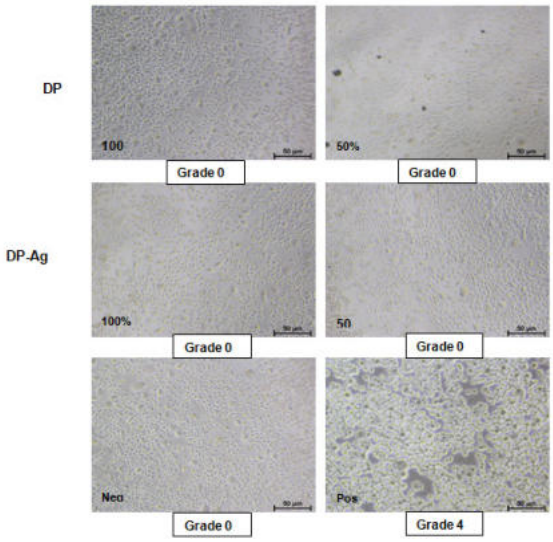

Fig. 7. Microscopic examination of cellular Anti-proliferation (Cytotoxity) on L929 cell line of Diethyl phthalate and Diethyl phthalate Silver nanoparticles.

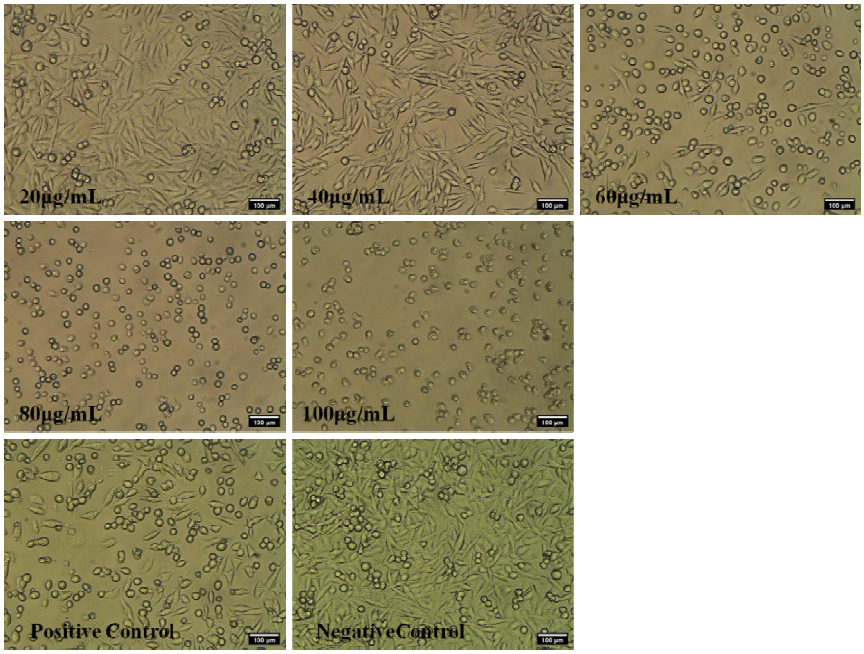

Fig. 8. Microscopic examination of cellular Anti-proliferation (Cytotoxity) on L929 cell line of Diethyl phthalate Gold nanoparticles

Table 1: Inhibitory percentage of study samples against DPPH radicals.

Concentration (µg/mL)	*A. paniculata*	Diethyl phthalate	DPAgNPs	DPAuNPs
100	44.94 ± 0.001	16.43 ± 0.001	60.36 ± 0.003	20.83 ± 0.001
80	31.61 ± 0.002	15.65 ± 0.001	56.9 ± 0.001	18.27 ± 0.001
60	23.99 ± 0.004	11.07 ± 0.001	53.51 ± 0.001	16.79 ± 0.001
40	20.83 ± 0.001	8.21 ± 0.002	51.13 ± 0.001	14.17 ± 0.001
20	15.18 ± 0.004	6.37 ± 0.001	47.62 ± 0.001	11.19 ± 0.001
IC 50	124.73	341.04	35.13	351.41

Table 2: One-tailed ANOVA of Sample groups for DPPH scavenging activity.

Source	DF	Sum of Square	Mean Square	F Statistic	P-value
Groups (between groups)	3	5390.2231	1796.741	37.7456	1.738e-7
Error (within groups)	16	761.6213	47.6013		
Total	19	6151.8444	323.7813		

Table 3: Total Anti-oxidant activity by Reduction of Phosphomolebdenum.

Concentration (µg/mL)	*A.paniculata*	Diethyl phthalate	DPAgNPs	DpAuNPs
100	34.78 ± 0.01	57.56 ± 0.011	83.64 ± 0.040	14.29 ± 0.1
80	26.17 ± 0.001	56.85 ± 0.002	76.6 ± 0.015	12.42 ± 0.1
60	25.49 ± 0.001	55.57 ± 0.003	71.01 ± 0.015	10.56 ± 0.1
40	24.55 ± 0.003	51.86 ± 0.003	60.04 ± 0.015	8.7 ± 0.1
20	22.75 ± 0.003	49.88 ± 0.002	54.45 ± 0.015	6.83± 0.1
IC 50	539.38	17.52	8.93	591.01

Table 4: One-tailed ANOVA of Sample groups for Total anti-oxidant activity.

Source	DF	Sum of Square	Mean Square	F Statistic	P-value
Groups (between groups)	3	10488.5862	3496.1954	76.176	1.089e-9
Error (within groups)	16	734.341	45.8963		
Total	19	11222.9271	590.6804		

Table 5: Cellular toxicity effect of study samples on L929 cell line by MTT assay.

Concentration (µg/mL)	DP	DPAgNPs	DP AuNPs
20	95.42 ± 0.011	95.98 ± 0.008	94.15 ± 0.011
40	93.85 ± 0.011	94.97 ± 0.002	92.67 ± 0.002
60	91.84 ± 0.005	93.41 ± 0.013	91.15 ± 0.002
80	91.13 ± 0.005	92.51 ± 0.009	88.12 ± 0.003
100	90.13 ± 0.008	89.68 ± 0.004	87.9 ± 0.002

Table 6: One-tailed ANOVA of Sample groups for Cytotoxicity effects on L929 cell line.

Source	DF	Sum of Square	Mean Square	F Statistic	P-value
Groups (between groups)	2	16.3634	8.1817	1.3557	0.2946
Error (within groups)	12	72.4206	6.0351		
Total	14	88.784	6.3417		

CONCLUSIONS

Nowadays, modern pharmacologists have turned to traditional and classic medicinal approaches for deriving multi-potential bioactive compounds to encounter a wide range of diseases and physiological disorders. In this research, the anti-oxidant potential and cytotoxic effects of a crude ethanolic extract of *Andrographis paniculata*, diethyl phthalate, silver, and gold nanoparticles synthesised using diethyl phthalate were evaluated, and the outcome revealed the improved anti-oxidant activity achieved from DPAgNPs compared with other test samples against both radicals (DPPH and phosphomolebdenum). It was also demonstrated that DPAgNPs had a less toxic effect on the L929 cell line among the study samples. The data show that using DPAgNPs for developing drug carrier systems is far superior to using *A. paniculata*, diethyl phthalate, and DPAuNPs alone, resulting in safe and fine activities.

FUTURE SCOPE

In future, in vivo toxicology studies can be performed to further investigate its toxicity. Further investigations to analyse its biocompatibility of Diethylphthalate with silver nanoparticle as drug carrier system and clinical trials are necessary for discovery of new drugs formulations.

Acknowledgement. First of all, I express my gratitude to God Almighty, for his abundant grace and his presence in all my endeavors. I am thankful to my Research Centre, Scott Christian College (Autonomous), Nagercoil for their constant support and encouragement. The authors are grateful for the technical support rendered by BioHub Research Consultancy, Kanniyakumari District, Tamilnadu, India for the analysis and interpretation of biological studies.
Conflict of Interest. None.

REFERENCES

Akbar, S. (2011). *Andrographis paniculata*: A Review of Pharmacological Activities and Clinical Effects. *Alternative Medicine Review, 16,* 66-77.

Awoyemi, O. K., Ewa, E. E., Abdulkarim, Ishaq and Aduloju, A. R. (2012). Ethnobotanical assessment of herbal plants in southwestern Nigeria. *Acad Res Int., 2,* 50-57.

Brand-Williams, W., Cuvelier, M. E. and Berset, C. L. W. T. (1995). Use of a free radical method to evaluate antioxidant activity. *LWT-Food science and Technology, 28*(1), 25-30.

Cai, Y, Luo, Q, Sun, M. and Corke, H. (2004). Antioxidant activity and phenolic compounds of 112 traditional Chinese medicinal plants associated with anticancer. *Life Sci., 74,* 2157-2184.

Farnsworth, N. R., Akerele, O., Bingel, A. S., Soejarto, D. D. and Guo, Z. (1985). Medicinal plants in therapy. *Bulletin of the World Health Organization, 63*(6), 965–981.

Gupta, A., Gupta, R., Sharma, K. K., Lodha, S., Achari, V., Asirvatham, A. J. and Deedwania, P. C. (2014). Prevalence of diabetes and cardiovascular risk factors in middle-class urban participants in India. *BMJ Open Diabetes Research and Care, 2*(1), e000048.

Jarukamjorn, K. and Nemoto, N. (2008.) Pharmacological aspects of *Andrographis paniculata* on health and its major diterpenoid constituent andrographolide. *Journal of Health Science*, *54*(4), 370–381.

Jayakumar, T., Hsieh, C. Y., Lee, J. J. and Sheu, J. R. (2013). Experimental and Clinical Pharmacology of *Andrographis paniculata* and Its Major Bioactive Phytoconstituent Andrographolide. Evidence-based complementary and alternative medicine: eCAM, 2013, 846740.

Khan, I., Mahfooz, S. and Ansari, I. A. (2020). Antiproliferative and Apoptotic Properties of Andrographolide Against Human Colon Cancer DLD1 Cell Line. *Endocr Metab Immune Disord Drug Targets., 20*(6), 930-942.

Leslie and Young (1992), Paths to Asian Medical Knowledge, first edition, ISBN: 9780520073180.

Li, B., Jiang, T., Liu, H., Miao, Z., Fang, D., Zheng, L. and Zhao, J. (2018). Andrographolide protects chondrocytes from oxidative stress injury by activation of the Keap1-Nrf2-Are signaling pathway. *J. Cell. Physiol. 234,* 561–571.

Marles, R. J. and Farnsworth, N. R. (1994). Plants as Sources of Anti-Diabetic Agents. In: Wagner, H. and Farnsworth, N.R., Eds., Economic and Medicinal Plant Research, Academic Press Ltd., London, 149-187.

Marzanna Kurzawa, Anna Filipiak-Szok, Ewa Kłodzińska, Edward Szłyk (2015). Determination of phytochemicals, antioxidant activity and total phenolic content in *Andrographis paniculata* using chromatographic methods, Journal of Chromatography B, Volumes 995–996, 2015, Pages 101-106.

Md. Sanower Hossain, Zannat Urbi, Abubakar Sule, K. M. and Hafizur Rahman (2014). *Andrographis paniculata* (Burm. f.) Wall. ex Nees: A Review of Ethnobotany, Phytochemistry, and Pharmacology. *The Scientific World Journal.*

MTT Cell Proliferation Assay Instruction Guide – ATCC, VA, USA www.atcc.org

Mussard, E., Cesaro, A., Lespessailles, E., Legrain, B., Berteina-Raboin, S. and Toumi, H. (2019). Andrographolide, a Natural Antioxidant: An Update. Antioxidants (Basel, Switzerland), *8*(12), 571.

Okhuarobo, A., Falodun, J. E., Erharuyi, O., Imieje, V., Falodun, A. and Langer, P. (2014). Harnessing the medicinal properties of *Andrographis paniculata* for diseases and beyond: a review of its phytochemistry and pharmacology. *Asian Pacific Journal of Tropical Disease*, *4*(3), 213–222.

Perumal and Gopalakrishnakone (2008). Therapeutic Potential of Plants as Anti-Microbials for Drug Discovery. Evidence-based complementary and alternative medicine : *eCAM, 7,* 283-294.

Phillips, O. L. and Meilleur, B. A. (1998). Usefulness and Economic Potential of the Rare Plants of the United

States: A Statistical Survey. *Economic Botany*, *52*(1), 57–67.

Polash, S., Saha, T., Hossain, M. and Sarker, S. (2017). Investigation of the Phytochemicals, Antioxidant, and Antimicrobial Activity of the *Andrographis paniculata* Leaf and Stem Extracts. *Advances in Bioscience and Biotechnology, 8*, 149-162.

Prieto, P., Pineda, M. and Aguilar, M. (1999). Spectrophotometric Quantitation of Antioxidant Capacity through the Formation of a Phosphomolybdenum Complex: Specific Application to the Determination of Vitamin E. *Anal Biochem, 269*, 337-341.

Shai, L. J., Masoko, P., Mokgotho, M. P., Magano, S. R., Mogale, A. M., Boaduo, N. and Eloff, J. N. (2010). Yeast alpha glucosidase inhibitory and antioxidant activities of six medicinal plants collected in Phalaborwa, South Africa. *South African Journal of Botany, 76*(3), 465-470.

Sharma, P. P. and Mujumdar, A.M. (2003). Traditional knowledge on plants from Toranmal plateau of Maharashtra.

Sinha S, Raghuwanshi R (2020). Evaluation of Phytochemical, Antioxidant and Reducing Activity in Whole Plant Extract of *Andrographis paniculata* (Burm.f.) Wall. ex Nees. Biosc. *Biotech.Res.Comm, 13*(4).

Tan, W. S. D., Liao, W., Peh, H.Y., Vila, M., Dong, J., Shen, H. M. and Wong, W. S. F. (2018). Andrographolide simultaneously augments Nrf2 antioxidant defense and facilitates autophagic flux blockade in cigarette smoke-exposed human bronchial epithelial cells. *Toxicol. Appl. Pharmacol., 360,* 120–130.

Umadevi, U. and Kamalam, M. (2014). Phytochemical and antioxidant studies on an important indigenous medicinal plant-*Andrographis paniculata* (burm.f) nees. *IJPSR , 5*(12), 5240-5244.

Uthirapandi, V., Subramanian, S. R. and Ponnerulan, B. (2021). Andrographolide production and enhanced antioxidant activity in *Andrographis paniculata* (Burm f.) Nees. promoted by seaweed liquid extracts. Braz. J. *Bot., 44*, 317–330.

Verma, N. and Vinayak, M. (2008). Antioxidant action of *Andrographis paniculata* on lymphoma. *Mol Biol Rep. Dec., 35*(4), 535-40.

Wang, T., Shankar, K., Bucci, T. J., Warbritton, A. and Mehendale, H. M. (2001). Diallyl sulfide inhibition of CYP2E1 does not rescue diabetic rats from thioacetamide-induced mortality. *Toxicology and applied pharmacology, 173*(1), 27-37.

Weaver, J. A., Beverly, B. E. J., Keshava, N., Mudipalli, A., Arzuaga, X., Cai, C., Hotchkiss, A. K., Makris, S. L. and Yost, E. E. (2020). Hazards of diethyl phthalate (DEP) exposure: A systematic review of animal toxicology studies. *Environment international, 145,* 105848.

Worasuttayangkurn, L., Nakareangrit, W., Kwangjai, J., Sritangos, P., Pholphana, N., Watcharasit, P., Rangkadilok, N., Thiantanawat, A. and Satayavivad, J. (2019). Acute oral toxicity evaluation of *Andrographis paniculata*-standardized first true leaf ethanolic extract. *Toxicology reports, 6*, 426–430.

World Health Organization, (2003). Concise international chemical assessment document 52: Diethyl phthalate. RISKLINE/2003120009 Geneva.

Yan, H., Huang, Z., Bai, Q., Sheng, Y., Hao, Z., Wang, Z., Ji, L (2018). Natural product andrographolide alleviated APAP-induced liver fibrosis by activating Nrf2 antioxidant pathway. *Toxicology*, 396–397, 1–12.

Zhang, X. F. and Tan, B. K. (2000). Antidiabetic Property of Ethanolic Extract of *Andrographis paniculata* in Streptozotocin-Diabetic Rats. *Acta Pharmacologica Sinica, 21,* 1157-1164.

How to cite this article: M. Shirley Navis and Ragel Mabel Saroja (2023). Studies on the Investigation of Anti-Oxidant and Cellular Toxicity on L929 Cell Line of *Andrographis Paniculata* and its Derivative of Silver and Gold Nanoparticles. *Biological Forum – An International Journal, 15*(4): 590-597.

IJNRD.ORG ISSN : 2456-4184
INTERNATIONAL JOURNAL OF NOVEL RESEARCH AND DEVELOPMENT (IJNRD) | IJNRD.ORG
An International Open Access, Peer-reviewed, Refereed Journal

TREATMENT OF HISTORY IN HILARY MANTEL'S WOLF HALL

RESHMA RAJU

PH.D SCHOLAR,

Dr.BHAGYALAKSHMI.A, ASSOCIATE PROFESSOR OF ENGLISH

TIRUPPUR KUMARAN COLLEGE FOR WOMEN

ABSTRACT:

The British writer, Hilary Mantel, earns both critical acclaim and bestseller status for her Cromwell trilogy. She is two-time Booker Prize winner for the first two books of this trilogy. This paper highlights the ways in which Mantel handles the historical characters in a lively and interesting manner in her first Booker Prize winning novel *Wolf Hall.*

FULL PAPER:

Hilary Mantel is Hilary Mary Thompson, born in July 6, 1952 in Hadfield, Derbyshire, England. She has been composing novels for really a long time before her scholarly fame. Her novels showcases her dull mind and complex expertise. She is known especially for her depressingly funny, socially examining books set in an extensive variety of contemporary and historical fiction. The most famous of her all novels, *Wolf Hall* (2009) portrays the growth of Thomas Cromwell, former Lord Great Chamberlain of the United Kingdom. It is praised for its great degree and complex depiction of its characters. It turned out to be a worldwide smash hit and won the Booker Prize. Its sequel, *Bring up the Bodies* (2012), centers all the more barely around Cromwell's part in the defeat of Anne Boleyn, and it too won the prestigious Booker Prize as well as the top honor of the Costa Book Awards. Both of these novels are adopted for stage play by Royal Shakespeare Company in 2013 and it is also made into television miniseries in 2015. In 2020, mantel released her last part of her Trilogy, *The Mirror and the Light*, which accounts Cromwell's tumble from power and his execution. Hilary Mantel had her sad demise on 22nd September, 2022 because of stroke.

Hilary Mantel is viewed as the representative of the Post-World War II English fiction writer. Her twelve novels range from the obscurely creative thrill to historically fictitious work. She is thus, the post-modern novelist. Her books though mirrors the comic components, yet she is a serious writer expressing the ethical vision. Her

books depicts her perspective towards life in a hopeful and in most part in a negative way. Her liking for history and historical events enable her to generate praiseworthy works like *A Place of Greater Safety* (1992), *A Change of Climate* (1994), *An Experiment in Love* (1995), *Beyond Black* (2005) and the Thomas Cromwell series.

Wolf Hall firmly follows the true history of Tudor Court. The Tudor reign begin with the King Henry VII, who believes firmly that to maintain the power one must keep a strong allies. So he marries his first son Arthur, to the Spanish princess Katherine of Aragon. Arthur passes just four months after his marriage and the second son, Henry VIII is made the King. Henry VIII is strong-willed to marry Katherine, and for that he gains a special ecclesiastical order which would permit him to wed his sibling's widow. Unfortunately, Katherine fails to give him a son and the only child left for them is Mary Tudor.

Wolf hall is set up in the England of 16th century. King Henry VIII is trying hard to divorce his wife Katherine and wed Anne Boleyn, but as Catholic Church believes marriage to be long-lasting and permanent, it does not support him for his divorce. Thus, he breaks away from the clutches of Roman Catholic rules and declares himself as the supreme head of the church and the country. He did this with the assistance of his self-determined and skillful minister, Thomas Cromwell, who is the protagonist of this historical novel. *Wolf Hall* begins with his humble, poor life as a child of blacksmith to his prosperity to rise as a lawyer and a legal adviser to the king himself.

Mantel has been evaluated as a hazily fanciful narrator. Her books range from confusing thriller to dark humor and to historical novels. She focuses mainly on family life, seclusion, the idea of time, feminism, religion, the outcome of the political and social framework. In this way she manages a variety of themes throughout her novel.

The *Wolf Hall* begins with the scene of Thomas Cromwell as a child being beaten mercilessly by his father, Walter. The scene makes it clear about father's brutality towards his only son. Everyone sympathize over the future of Cromwell and the thing that it is better for him to leave the house than to tolerate beatings. Thomas, too feel it as the proper solution and leaves the house. In France, he learns three card game and helps the lowlanders, where he learns good and miserable side of life. His only longing is to get enlisted in the military to be an officer: "he walks around the docks saying to people, do you know where there's a war just now?" (Mantel 14). Cromwell from the very young age dreams of achieving a great height.

Wolf Hall cherishes, recollection of childhood memories which plays an essential part in the evolution of the characters as well as the plot of the novel. Thomas Cromwell, is seen recalling his sad miserable life, which caused him to leave his house and achieve on his own. *Wolf Hall* also has the description of King Henry VIII thinking of his lost blissful childhood: "I lived at the palace at Eltham, I had a fool called Goose" (Mantel 618). Queen Katherine too recalls her childhood multiple times.

The novel portrays that, people of Tudor court are exceptionally ambition to snatch power, even if it is through their double dealing or through defilement. When King Henry VIII realizes that the church won't give him a divorce, he nullifies the power of the church and declares himself as the supreme head over all the churches. Anne Boleyn with her timid diplomacy, secures the favor of the King and earns high posts for her brothers and father. She also remains strict on the notion that before beginning the relationship, King Henry VIII must legally marry her.

Cromwell is an intellectual man. He is fully aware that men wear mask to hide their own identity. One must be very careful and always find out what people wear under their clothes. That is, one must be careful towards others motifs. Thus, he keeps a close eye on people's defiance and reservations to execute his plans at the right moment. To earn the favor of the king, Cromwell disregards his own principles and satisfies all the cravings of the King. Cromwell knows that Cardinal Wolsey is powerful only till he satisfies King's desire. Wolsey's power and nobility disappears at the King's dismay, which teaches Cromwell that he should have the King's aid to rise in court. As needs be Cromwell is ready to continuously oblige to the King even when he is ethically against to what King is doing. When Henry request the King to prosecute Thomas More for a wrong doing which he didn't carry out; Cromwell shows no opposition. Thus, Cromwell's ambition combined with his important skill assists him to climb to the high position in the King's court.

King Henry VIII is an ardent devotee of Roman Catholic Church. He, thus wants to nullify his marriage with the papal support. He waits for twenty years to get a male heir. If Henry VIII fails to produce a male heir then there is a chance of Civil War. It is because of this that he marries six women; namely Katherine of Aragon, the mother of future Queen Mary I; Anne Boleyn, the mother of Future Queen Elizabeth I; Jane Seymour, the mother of future King Edward VI; Anne of Cleves; Catherine Howard and Catherine Parr.

Marriage, thus plays a major role in *Wolf Hall* as the story revolve around the dissolution of one marriage and legitimization of another marriage of Henry VIII. Katherine who doesn't want to divorce the King, plays all her cards till Cromwell persuades her advantages saying that, her daughter Mary will be made the Princess and she will get a decent sum of wealth for her living.

Anne Boleyn who the King needs to marry, likewise is been anxious to become the Queen of England, which is impossible unless she legally marry the King. She feels the vulnerability and uneasiness about her marriage. As their secret marriage is fixed, there fosters another problem, one Harry Percy claims that he has covertly married Anne and she is his lawful wedded wife and the King can't marry her. It is Cromwell again who decides to dispose of this case. In a public gathering where King needs to get the public consent to his marriage, a nun, Elizabeth Barton, shows up and predicts the destruction of the Kingdom if he marries Anne. Anne at this time keep a close watch on the individuals who support her and individual who go against the marriage. The people assisting their marriage were heavily rewarded and the rivals where tormented after she legally became the Queen.

In the beginning of the novel, the castle of Cardinal Wolsey is being vacated and he is being ordered to return back the great seal of England, which is his power of authority. He is shifted to Tower, which is a place of torment. This embarrassment of Wolsey gives Thomas Cromwell a tricky idea of revenge. He, thus intentionally draws near to the King so that he can do the things all the more without any problem. He sends Cardinal Wolsey to north and instead of going with him, he sends Rafe and Richard to accompany Wolsey. Meanwhile he is working to become more close to the King. Cromwell plots vengeance against all who are responsible for Wolsey's condition. Among them he needs to diminish the significance of Stephen Gardiner, Henry Norris, Harry Percy, Duke of Norfolk and Duke of Suffolk and some others. At a certain point of time, after becoming the counselor of the King, he puts before the House of Commons a bill to suspend the money to be deposited to Rome. This is a plan of Cromwell to show the King, his true supporters. Thus, King finds out who all are for him and who all are against him. He does it cunningly. At this point he forces to desert the Stephen Gardiner from his house in the name of Anne Boleyn. He thus, outsmart every individual in plotting revenge. He works cunningly like a wolf. King Henry has praised him saying that he is as clever as a bag of serpents.

The theme of childhood, ambition, religion, marriage etc. in *Wolf Hall* leads to a major theme, transformation. The protagonist, Thomas Cromwell, a son of Blacksmith transforms into a strong and powerful man. He elopes at the age of nine to escape his father's beating and comes back only twelve years later with a wife, Liz. He gets an opportunity to work with Cardinal Wolsey which paves him a way to become close to king and he with his talent emerges as a Counselor to the King, then becomes a keeper to the jewel house. He later replaces Stephan Gardinar and becomes a master Secretary. Then, becomes King's deputy in church affairs too. *Wolf hall* thus, is the story of transformation of Cromwell, which Hilary mantel showcase in an amazing and trustworthy way.

Hilary Mantel is noted for her thematic diversity:

> Diversity of theme is the main characteristic of novels of Hilary mantel. There is no one connection in Hilary Mantel's two novels, in respect of theme. Even the sequel of Thomas Cromwell's trilogy novels has different themes *Wolf Hall* deals with rise of Thomas Cromwell from a son of a poor blacksmith to King Henry's right hand. The sequel of this novel *Bring Up The Bodies* is about beheading of Anne Boleyn and Cromwell's avenge on his enemies. (Deokar 18)

She has uniqueness and writes each novel with the unique theme.

> Hilary Mantel makes clear her 'novelistic vision'. She states life itself is unstable and so we are. If one tried to be stable then he or she would be finished. Therefore, Hilary mantel hates monotonousness in writing and wants choice. (Deokar 201)

The theme of *Wolf Hall* is vastly distinct. When Thomas Cromwell and Thurston, his cook, discuss Cardinal Wolsey and Norfolk, they discuss the historical concept that "man is wolf to man". This is the central theme of

this novel. The main characters in this novel are trying their hardest to stay in power in the English court by any means necessary. Man has transformed into a wolf in this circumstance.

Although *Wolf Hall* is a historical novel, as a piece of fiction it offers a relatively accurate insight into the lives of people living in the Tudor period. Through this novel Hilary Mantel paints a picture of people in Tudor England. She does not provide a historical factual record that fits stereotypes; but also describes how English people used to think and act during that time. During this time, aristocrats, kings, queens, and even priest has a tendency to say that man is wolf to man. Characters and incidents in the current novel demonstrate the same trend. The saying, man is a wolf to man means, the man acts like a wolf towards another man for his own benefits. King Henry wants to marry Anne Boleyn and divorce his first wife in order to produce a male heir. Yet, Pope of Rome doesn't permit him to do as such. The idea of a male heir is the King's obsession. He captures Cardinal Wolsey and imprisons him for treason, where he dies. By punishing Cardinal Wolsey, the King hope to instruct the Pope. Thomas More, who disagree with the King's status as head of the Church of England, and he too is beheaded by him. King Henry thus, transforms into a wolf and kills his enemies to fulfill his wish. Anne Boleyn needs to wed King Henry and she too becomes like wolf and is ready to kill anyone who gets in the way of her in becoming the Queen of England. The theme of man is wolf to man oozes throughout the novel revealing the Tudor's tendency.

The characters portrayed by Hilary Mantel have not been depicted in historical context. She has however reinvented them. She has shown the readers what goes on inside these characters' heads. The phrase "man is wolf to man" serves as the novel's overarching historical theme. The main characters in the novel use both good and foul tactics to gain or maintain power in English court. The current novel has a very straightforward plot, in order to make it easier for readers to comprehend the serious historical novel and keep them interested in reading. *Wolf Hall* thus is definitely a work that bought fame and recognition to our late writer Hilary Mantel.

REFERENCE:

1. Mantel, Hilary. *Wolf Hall*. 4th Estate, 2019.
2. Deokar Hemant Ramesh, 2018, *Experimentalism in the novels of Hilary Mantel*, Kavayitri Bahinabai Chaudhari North Maharashtra University, Jalgaon.
3. Farlex Dictionary of Idioms. 2015. Farlex, Inc 26 Nov.
4. Morrill, John S. and Elton, Geoffrey R.. "Henry VIII". Encyclopedia Britannica, 17 Aug. 2022,

ISSN 2348-8425

SATRAACHEE

An International Registered Peer Reviewed Bilingual Research Journal

सत्राची

A UGC-CARE Enlisted
Peer Reviewed Research Journal

Year 11, Issue 26,
Vol 38, No. 2.
Jan.-March, 2023

Editors

Kamlesh Verma ❁ Anand Bihari

ISSN : 2348-8425

SATRAACHEE

UGC Care Enlisted, Peer Reviewed research Journal

Issue 26, Vol. 38, No. 2, Jan-March, 2023

सत्राची

मानविकी एवं सामाजिक विज्ञान की पूर्व समीक्षित त्रैमासिक शोध पत्रिका
Pre-Reviewed Quarterly Research Journal of the Humanities and Social Sciences

Price : ₹ 250

Subscription:

Five Year : Rs. 5000/- (Personal)
: Rs. 10000/- (Institutional)
Life Time : Rs. 12000/- (Personal)
: Rs. 25000/- (Institutional)

The Draft/Cheque may please be made in favour of
'SATRAACHEE FOUNDATION'
C/A No. 40034072172. IFSC : SBIN0006551,
State Bank of India, Boring Canal Rd.-Rajapool,
East Boring Canal Road, Patna, Bihar, Pin: 800001

Editing/Publishing: Unpaid/ Unprofessional
Publisher: *Satraachee Foundation, Patna*
Cover Photo: *Soumya Swarnim*

Editorial Contact:
Anand Bihari
Kala Kunj, Besdide Canara Bank
Bazar Samiti Road, Bahadurpur
Patna-800016

Website : http://satraachee.org.in
E-mail : satraachee@gmail.com
Mob. : 9661792414, 9470738162 (A.Bihari.)
: 9415256226 (Kamlesh Verma.)

❖❖❖

In this Issue

❖❖❖

Importance of Marriage Ideals in Premchand's *Gaban*

Amala Thomas[1], Dr. D. Joen Joselin[2]

[1] Reg No:18213014012015 , Research Scholar, Annai Velankanni College, Tholayavattam. (Affiliated to Manonmaniam Sundaranar University, Abishekapatti, Tirunelveli-627012, Tamil Nadu, India.)

[2] Associate professor and Research Supervisor, Department of English, Annai Velankanni College, Tholayavattam. (Affiliated to Manonmaniam Sundaranar University, Abishekapatti, Tirunelveli-627012, Tamil Nadu, India.)

Abstract

In Indian society marriage is considered as the most important relationship. Mutual understanding, love and care are some of the important factors, which are necessary to keep the marital life strong. In **Gaban,** Premchand has depicted the problems in the marital life of the couples, which can destroy marriages.

Keywords : Family, Marriage, Middle class society, Jewels.

Marriage is considered the most important sacred bond, between husband and wife since ancient times in India, which brings together a man and a woman, and connects them together for life time through sacred rituals. Family is an important link between a human being and society. Marriage is all about husband and wife living together with mutual understanding to create a family. But for the achievement of this understanding there should be compatibility among husband and wife.

Indian culture is very rigid about its age old norms. Premchand felt deeply that the age-old social norms of marriage are rotting the society.He criticized mismatch in marriage, dowry system and child marriage. These issues led to disparity among the husband and wife, which in further destroyed the peace and serenity of marital life of couples and led to unhappiness in the families. Premchand in his stories and novels has portrayed all the anomalies present in marital life. Thereby, people will save themselves from these malpractices. Premchand who was against all these malpractices had joined Arya Samaj which was rebelling against all these problems.

Premchand in his writings eulogized the marriage ideals. If husband and wife are not able to follow the ideals of marriage, then their marital life suffer, which in further leads to

discord in the family. He wrote about the problems, which degraded the sacredness of marriage, with an aim of readers becoming aware of it.

Gaban looks upon the problems prevalent in the middle-class society; people of this class always suffer from a sense of low self-esteem, as they are not able to afford what they want. They aspire to be like upper class society people. The problem with the people is that they are not able to work out their life with what little they earn. There is a want among them to have more than what they can afford.

The story of the novel begins in Allahabad. The story revolves around the life of young couple Jalpa and Ramanath. It tells about the plight of middle class couples who are entrapped inside the vicious circle of vanity. Instead of being satisfied with what they have, they destroy their own peace, in their greed for more. Ramanath and Jalpa are best example of it.

Dindayal and Dayanath belong to middle class families. Dindayal as an agent of a landlordhas a meagre income of five rupees per month, which was not enough for running a family. He had other sources of income, from where he got money, which are never mentioned. His daughter Jalpa, at an early age develops a craze for jewellery, and is assured by her elders that during her marriage she will get her favourite piece of jewel (Chandrahar) from her groom. Dayanath, a father of three sons, worked in the court, he was an honest man, and he somehow managed to take care of his family with his income of fifty rupees per month. His eldest son Ramanath is a carefree person. Dayanath was not able to send him for further studies due to lack of money. That didn't matter to Ramanath, because he never took life too seriously. His life is totally built up on the foundation of lies. Dayanath hesitates in getting Ramanath married, because " to marry off someone who doesn't even concern himself about where his next meal is coming from" felt wrong to him (*Gaban*5).

He wants to live a life of extravagance. He enjoys himself by moving around extravagantly through help of his friends. Ramanath represents weakness of the middle class society. He runs away from his responsibilities and thinks illusions created through lies are good. He is morally a weak person. He wavers in taking decisions till the end.

Jalpa and Ramanath's marriage takes place without any problem of dowry unlike in the case of most of the marriages. But Dayanath spends too much on marriage celebrations, much more than the money he had. He buys jewellery on loan, for which he is not being able to pay back. Therefore Ramanath steals Jalpa's jewels and gives it to the jeweller. He lies about his family's true conditions to his wife. After he gets a job in the municipality office through his friend Ramesh, he lies about the income to his wife. He starts getting decent salary but is not able to save any, even though he took bribes from the office. Because, he boasts in front of his wife and to make her happy he spends extravagantly. He buys jewellery for her on loan, thereby, gets in high debt. He lies to Jalpa's friend Ratan, about the price of Jalpa's bracelet and by mistake ends up spending her money also. To escape from problems he tries to use office money (with no intention of embezzling it). Which, Jalpa unknowingly gives to Ratan. Thereafter, Ramanath feeling unable to put back the office money gets a fear of embezzlement case against him, therefore he runs away to Calcutta.

In Calcutta, police arrests Ramanath on suspicion of another case, scare him with

false charges (since no actual embezzlement had happened) and forces him to become a false witness by bribing him with money and job. He being a morally weak man falls for it. Thereby after getting trapped in devious games of police, he gives false testimony. Jalpa when gets to know about it, is furious with Ramanath's cowardliness.

When Ramanath used to buy jewellery for her, she in her obsession of jewellery used to become more devoted to him. But that doesn't mean her character is limited to the typical image of a middle-class woman with love of jewellery. She has self-respect and moral strength also, as she returns her mother's jewellery, which is sent to her when Jalpa's jewellery gets stolen, she vehemently says, "I won't take charity from anyone, even my own mother" (*Gaban* 39).

When Jalpagets to know the truth about the actual financial condition of Ramanath, she regrets her own behaviour, a new change comes within her and her true devotion towards her husband comes to the fore as she happily sells off her favourite jewels to return the office money and pay off the debt. Jalpa likes jewellery but that doesn't mean she doesn't love her husband. When she learns about the true condition of her husband, she sacrifices her attachment to all the splendour and luxury and comes out as a devoted wife. It is Jalpa who puts a lot of effort to bring her husband out of his erroneous path.

There is marital love between Jalpa and Ramanath, but it lacks trust and devotion. In marriage happiness can be achieved only through understanding and truth. He gets in trouble because of the lies he thought would protect his conjugal life. Jalpa in her cravings for jewellery never tried to analyse the financial condition of her husband. Situation wouldn't have taken a wrong turn "[if]Jalpa had been able to hold herself steady through the stormy blasts of her cravings, if Rama had not yielded to his embarrassment" (*Gaban*68).

He hesitates in making decisions and behaves like a coward. He himself creates troubles for himself, and then feels incapable of facing them. Apart from all these negative traits, he has some redeeming qualities also. Hisson like affection towards Devidin, and his wife Jaggo(without paying attention to the fact that they, belong to a lower caste). And most importantly his unending love for Jalpa.

Ramanath is a morally weak person, and Jalpa is infatuated with jewellery, which she is able to overcome because of inner strength, her pure love and concern for her husband. This is something which Ramanath lacks. In the end after all the trials and tribulations, when both reject show off and love of luxury, they are able to enjoy the true bliss of married life. Trial was necessary to cleanse them of all the faults so they are truly prepared for a true bond.

Another problem is of incompatible marriages prevalent in the society. Premchand had critiqued unmatched marriages in his other works like *Nirmala* and *Sevasadan* also. As he had to go through one in his own life as Amrit Rai points, "His own father remarried at an old age and left behind a widow and a little son" (38). Not only that "he himself had been married off at a tender age, and had to bear at first the responsibility of making a go of an utterly incompatible and awkward match, and later the guilt of failing to do so"(38).

Ratan has a mismatch marriage with a much older widower Vakil Sahib.After the death of her parents, Ratan's uncle gets her married to Advocate of Allahabad's High Court, Indra Bhushan. Ratan respects Vakil Sahib and he treats her with fatherly affection.

He buys for her everything she wants .But there is no husband and wife love between them. They respect each other's feelings. But somehow it lacks mutual understanding. He is not able to foreshadow the troubles; she will have in future, if he doesn't give her, her share of property. Even when he is very sick, he also like Ramanath wavers in taking decision. Towards the end of his life, Vakil Sahib with a full knowledge of legal system didn't settle anything for his wife for her secure future.

Shehad sacrificed her youth for him, as she herself tells Jalpa"I never even thought that I'm a young woman and he's an old man"(*Gaban*137). She also liked jewellery likeJalpa. She had everything in terms of luxurious life, she enjoyed herself in roaming, buying things and parties. Herluxurious life quelled her anxiety related to marriage. But everything is destroyed when her husband's nephew Manibhushan through his deviousness usurps everything, after his death. Ratan thinks that she will be able to survive, without her husband. But as a widow she has no place in the society, no identity without her husband, and no place in her husband's family, because after husband's death as she says in anguish, husband's family "is not a bed of flowers for you, but a bed of thorns"(*Gaban* 245).

The other couples whose marriage the novel gives us glimpse of is Devidin and Jaggo and Dayanath and Jageshwari. Dayanath is an honest man, in his many years of government job he never took bribe, his wife Jageshwari is not enthusiastic about this behaviour of his, since she acutely feels the poverty they are in. she is remorseful of the fact that even after all the struggles she has faced in bringing up the family, her little desires also never got fulfilled.

Then there is Devidin and Jaggo, who also have different temperaments, except for the love of their dead sons and their affection for Ramanath. Devidin is a man who believes in simple living unlike his wife who has a craze for jewellery.

Like Devidin and Jaggo, both Dayanath and Jageshwari also have different opinions on matters. But these old couples have a strong relationship as they stand out for each other in times of need. For a successful marriage Premchand through this novel has represented that, there should be understanding and compatibility

Works Cited :

- Premchand.*Gaban: The Stolen Jewels.* Trans. Christopher. R. King. Delhi: Oxford University Press, 2000.
- Rai, Amrit. *Premchand: His Life and Times.* Trans. Harish Trivedi. Delhi: Oxford University Press, 2002.

***

ISSN 2582-5356
RNI-UPBIL/2018/78084
Volume 6/Issue 8 ❖ January - June, 2023
Bilingual (English & Hindi)

UGC CARE Enlisted Journal

KUTAP

AN ENSEMBLE OF MUSICIANS

कुतप

A Peer Reviewed Refereed International Journal

संगीत एवं अन्तर-विषयक विधाओं पर केन्द्रित

Special issue - Seminar Proceedings

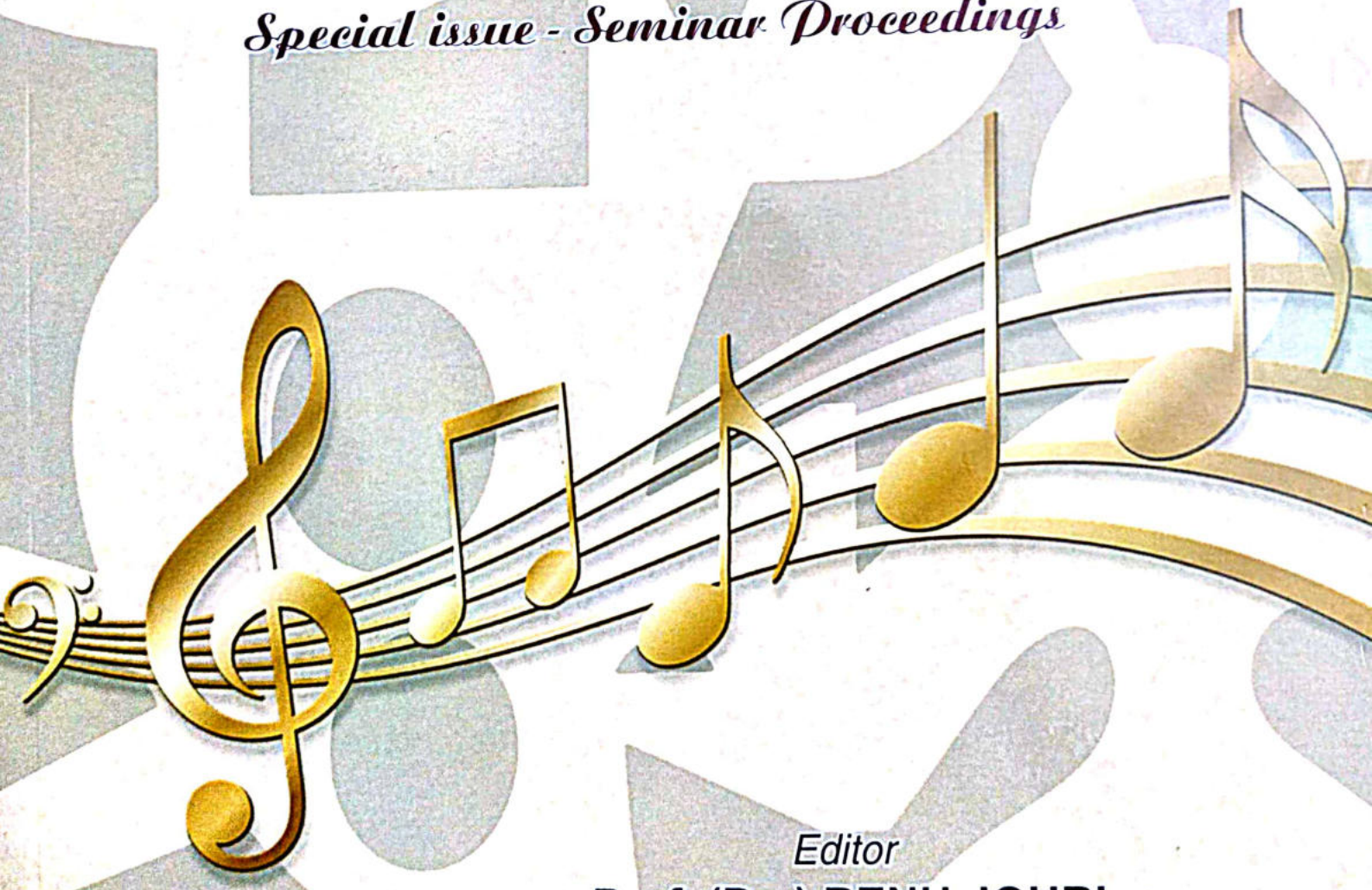

Editor
Prof. (Dr.) RENU JOHRI

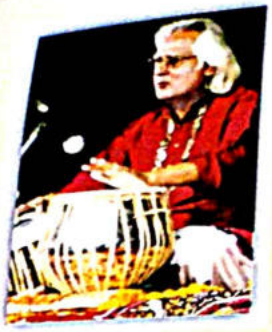

ETERNAL PATRON
Late Pt Kumar Lal Mishra
Renowned Tabla Artist,
Banaras School of Tabla

PATRON
Dr. Shashi Bhardwaj
Ex Head & Associate Prof. Music Dept
Ex Principal Sahu Ram Swaroop
Mahila Maha Vidyalaya Bareilly

EDITOR
Prof. (Dr.) Renu Johri
Professor (Tabla) Department of Music &
Performing Arts, University of Allahabad
Founder of Padma Bhushan Pt. Samta Prasad
Trust of Tabla

ADVISORY BOARD

Prof. Mukesh Garg
Ex Associate Professor (Hindi)
Delhi University, Famous Music critic
Former Editor of the Oldest Journal 'Hathras'
Owner of world wide organization Sankalp

Prof. Ajay Jaitly
Professor and Head,
Visual Arts Department
University of Allahabad

Prof. H S Upadhyay
Ex. controller of Examination
Head Philosophy Department
University of Allahabad

Glenn Califas
Composer/Author
Music Composer
at freelance Musician
Address : 1299 La pintoresca drive
No. 1, Pasadena California 91103 (U.S.)

Pepe Flore
Practioner/Tutor Percussion
Instruments, Roverto Italy
pepeflore@libero.it

EDITORAL BOARD

Dr. K Sashi Kumar
Professor and Dean
Faculty of Performing Arts
Banaras Hindu University, Varanasi

Prof Gunjan Sushil
Department of English
University of Allahabad,
Prayagraj

Dr. Rajesh Garg
Associate Professor
Hindi Department, Coordinator NSS
University of Allahabad, Prayagraj

Pt. Sanju Shahai
Tabla Player/Musician
London United Kingdom
www.sanjusahai.com

Dr. Seema Johri
Asst. Prof. Music Department
Kurukshetra University
Kurukshetra Haryana

PEER REVIEW COMMITTEE

Prof. Swatantra Sharma
Former Vice Chancellor,
R.M.T. University Gwalior
Ex Head, Department of Music &
Performing Arts, University of Allahabad

Prof. Pankaj Mala Sharma
Ex Head, Music Department of
Punjab University, Chandigarh

Prof. Ajay Ashtaputre
Former Head and Dean
Faculty of Performing arts the
M.S. University of Baroda

ISSN : 2582–5356
UGC CARE Enlisted Journal
RNI No. UPBIL/2018/78084

कुतप

वर्ष : 6 अंक : 8 जनवरी-जून, 2023

संगीत एवं अन्तर-विषयक विधाओं पर केन्द्रित

Special issue Seminar Proceedings

सम्पादक
प्रो. (डॉ.) रेनू जौहरी

प्रकाशक
पाठक पब्लिकेशन
35, महाजनी टोला, जीरो रोड
इलाहाबाद-211003 (उ.प्र.)

Instruction for Contributors and Subscribers

Authors are requested to send their papers based on *Music and interdisciplinary Branches*. The length of a paper including tables, diagrams, illustrations, etc., should not exceed 20 double spaced pages. Manuscripts sent for publication in this journal should not have been published or sent for publication elsewhere and authors will submit a certificate in this regard. All correspondence will be held with the senior (first author only).

Two copies of the manuscript typed in double space size 12, in "Times Roman" font and in hindi Krutidev-10 on A4 size bond paper should be submitted. The same will be submitted through email. All contributions submitted will be subjected to peer review. The decision of Editorial Committee will be the final.

The authors are responsible for copyright clearance for any part of the contents of their articles. The opinions expressed in the articles of this journal are those of the authors and do not reflect the objectives or opinion of the journal.

Authors are requested to send their manuscripts to :

Prof. (Dr.) Renu Johri

Editor
Prof. (Dr.) Renu Johri
Professor. Music & Performing Arts Deptt,
University of Allahabad-211002
renujohri2@gmail.com

SUBSCRIPTIONS

In Other Countries (Rs.)			In India (Rs.)		
Print	:	Rs. 3000.00	Print	:	Rs. 500.00
Online	:	Rs. 2000.00	Online	:	Rs. 250.00
Print+Online	:	Rs. 7000.00	Print + Online	:	Rs. 700.00

Published by : RATNAKAR PATHAK
Printed by : ROBIN DIXIT on behalf of RENU JOHRI.
Printed at : CHANDRAKALA UNIVERSAL PVT. LTD. 42/7 JAWAHAR LAL NEHRU ROAD, PRAYAGRAJ
Published from : PATHAK PUBLICATION, 35 MAHAJANI TOLA ZERO ROAD, PRAYAGRAJ-211003
Editor : **Prof (Dr.) Renu Johri**, A-6, University Flats Chaitham Lines, Prayagraj

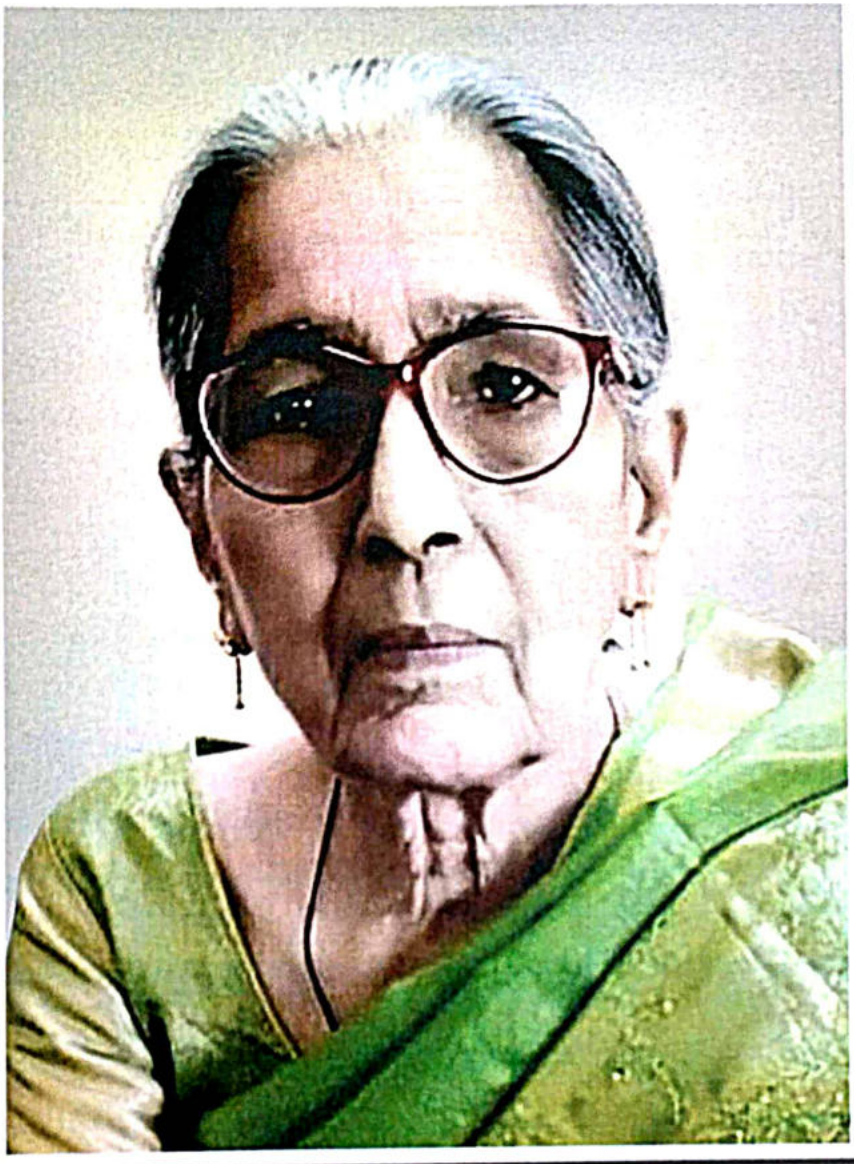

श्रीमती शकुन्तला जौहरी

जन्म तिथि 01.01.1946
पुण्य तिथि 25.03.2023

पद्म भूषण पंडित सामता प्रसाद ट्रस्ट ऑफ तबला की अध्यक्ष व मेरी परम श्रद्धेय माँ श्रीमती शकुन्तला जौहरी ने दिनांक 25/03/2023 को अपना पार्थिव शरीर त्यागकर परलोक गमन किया। 'कुतप' शोध पत्रिका का शुभारंभ उक्त ट्रस्ट के आधार पर ही हुआ है। अतः ट्रस्ट व कुतप परिवार की ओर से माँ को भावभीनी श्रद्धांजलि प्रेषित है व पूर्ण विश्वास है कि सूक्ष्म जगत से आपका आशीर्वाद व प्रेरणा सतत मिलती रहेगी। इहलोक व परलोक का सम्बन्ध जुड़ा रहेगा। आपको नम आँखों से कोटिशः नमन वंदन करती हूँ।

Editorial

This is VIIIth issue of 'Kutap' Journal. This is a special issue in terms of variety of readings. There are three chapters in this particular issue. First one is based on music & interdisciplinary. From an International Seminar titled 'Promotion of Indian Language, art and culture regarding' National Education policy 2020; which was held on February 10th and 11th 2023, organized by Music and Performing Arts Department, University of Allahabad, 10 best research papers have been selected for this issue of Kutap and placed in chapter IInd. chapter IIIrd has included research paper of Arts & humanities from Arunachala College of Engineering for Women, Kanyakumari, disrict Tamilnadu. Communion of North, East, West & South through vast ocean of knowledge is the first & foremost aim of the formation of the Journal Kutap. For readers, there is an adequate amount of material to nourish their brain. This special issue is dedicated to my beloved, great mother Smt. Shakuntla Johri, who inspired me to start Kutap Jounal. She left us for her heavenly abode on March 25th 2023. My heartfelt Naman to her.

I tender my Heartfelt wishes & congratulations to all authors for their valuable contribution.

Thanks and Regards

Prof. Renu Johri
Head
Dept. of Music and Performing Arts
University fo Allahabad

अनुक्रमणिका / Index

अन्तर राष्ट्रीय संगोष्ठी के कार्यवाही आधारित शोध-प्रपत्र

बहुविषयक प्रपत्र

Depiction of Oppressed Peasants in Premchand's *Godaan*

Amala Thomas* **& Dr. D .Joen Joselin†**

Abstract–*Munshi Premchand was always at his best when it came to writing about the village life. The present study deals with Premchand's portrayal of suffering of peasants in the village through his work* ***Godaan****. Through the character of Hori, Premchand explores the various factors which lead to peasants' deplorable condition. Is it external or internal? This work tries to analyze the problem.*

Keywords: Peasants, Gandhian ideology, Progressive, Village, Rural, Urban, Colonialism

Dhanpat Rai Srivastava (13 July 1880 - 8 October 1936), known by the penname Munshi Premchand, is the most acclaimed writer of Hindi-Urdu literature. Premchand was also a prominent member of "All India Progressive Writers' Association", which was formed in India in 1936.*Godaan*, which is considered a masterpiece among his writings, was published in 1936, it was also the last novel he wrote.

Godaan was written around at the time when, in India, national movements for independence were running in full swing. He never took active part in national movements, but he believed that, as a writer he could bring about change through his works. Premchand was a writer of the people. He was very sympathetic towards the down trodden people of the society. He believed in the writer's role as a social reformer. He was a firm believer in literature as a tool in bringing change by projecting the reality of the society to the readers.

This novel epitomizes his ideas and shows the stark reality of struggling peasant class.The novel looks upon the lives of the people living in the city of Lucknow which was Awadh's capital, and Belari and Semari, the two villages in the province of Awadh. Hori the tragic hero of the novel, symbolizes the peasant class of India, and, their never ending battle against poverty as they are constantly subjugated by the ruling class. Hori a poor, hard working peasant from the village Belari, has only one simple dream in his life, which is to own a cow. Even though, Hori and his wife Dhaniya work hard, day and night, it is never enough to even provide a proper meal in the family. Hori, like other peasants in his village is always in debt, because of family commitments, and especially moneylenders' callousness. He never questions or resist, against the cruel traditions and customs which he knows are the cause of his misery. He easily gives in to the words of the exploiting moneylenders. He has blind faith in destiny. In the end Hori dies, without having his dreams fulfilled.

Premchand in his works focuses upon the social and economic conditions of people of that time, especially in *Godaan, the* peasant class. As many critics have also pointed out Premchand is at his best when he depicts the rural society. As Prem kumar has pointed out, "Premchand was born and raised in a village and he best understood life in rural surroundings. Although he spent a considerable portion of life in various cities, he had recognized early in his career that India was essentially a rural society, and that any attempt at reforming India must focus on the village" (67).

Both city and village are presented in a stark contrast with each other in his writings. Peasants in colonial India are shown to be doubly subjugated because of the colonial and feudal system, who with their capitalistic interests, had broken the spirit of peasant people. The main center of this exploitative culture, was epitomized as being the city with its decadent urban culture. As we see especially in *Godaan*. City people as seen in the novel, are corrupt and selfish, as showcased in the characters like Khanna (the industrialist) and Rai Sahib (the feudal landlord), who are the epitome of moral decay, as their only motive in the entire novel is to squeeze money out of poor working class people. Even some characters like Professor Mehta, Miss Malti, Mirza Khurshed and Pandit Onkarnath, with their high talk are not shown to

* Reg No:18213014012015, Research Scholar, Annai Velankanni College,Tholayavattam. Affiliated to Manonmaniam Sundaranar University, Abishekapatti, Tirunelveli-627012

† Associate professor and Research Supervisor, Department of English, Annai Velankanni College,Tholayavattam. Affiliated to Manonmaniam Sundaranar University, Abishekapatti, Tirunelveli-627012

be doing anything fruitful for the poor people.

This depiction coincides with the Gandhian philosophy of rural-urban dichotomy. During his lifetime apart from socialist ideology, Premchand was also influenced by Gandhi's social outlook .Premchand, for a time, was a follower of Gandhian ideology of thought, according to which, he also felt that elite classes of urban areas had a parasitic nature towards the poor peasants, and city culture was an extension of British imperialistic ideology. As P.C. Joshi points out "Gandhi saw in the town-village confrontation a major expression of the irreconcilable cleavage between Indian nationalism and British colonialism" (46), not only that, Gandhi also believed in as Joshi further says in the "non-class concepts of 'change of heart on the part of propertied classes and of 'reformed' and 'good landlords' as trustees of peasants" (45). Premchand incorporated these ideas in his earlier novels. For e.g. in *Karmabhumi*, city comes across as a place only for rich people. Selfish and arrogant; these elite city people exploit the working people for their own gain. But in the end there is change of heart in many of these wealthy people. In *Gaban* , as Kumar points, the main characters at the end fed up with their city life "go and establish a utopian community by the river Ganges away from the corruptions and degradations of city life" (71). In *Sevasadan* too we come to see moral decaying in the city of Benaras, where the main protagonist Suman, falls prey to false enchantment of the life of prostitution.

In the novel *Godaan,* rural and urban society with its characters, are kept apart, with Rai Sahib and Hori's son Gobar being the connecting links. City's evil influence can be seen through changes in Gobar's behavior. Gobar was always rebellious, but he always used to respect his parents. His stay in the city changes him a lot, which is seen after he returns the village. He becomes disrespectful towards his parents and elders in the village, and having acquired some money in the city, he becomes very proud. When he returns to city with his wife Jhuniya, their lonely existence is quite visible, unlike in the village, where close ones are always there to support.

Even if Premchand had adhered to the Gandhian philosophy in the earlier writings, he goes beyond that in *Godaan*. As Joshi points "Premchand, did not allow himself to become a prisoner of Gandhi's backward looking idealization of the village and denigration of the town" (43).

Premchand has taken a more critical stance in his outlook to the peasant suffering, and as Joshi says "Premchand no longer focus on the 'enemy outside' the village" (53). A deeper look gives us an understanding that there is more about the problems of peasants' suffering. It is true that the city dwellers have shallow outlook towards the peasants. But the peasants are to be blamed themselves for their situation as they are not willing to stand up for themselves and are ready to be victimized by the backward traditions and social ideologies which help the corrupt people like village superiors (the moneylenders) to victimize the peasants, by using their gullibility.

Premchand in *Godaan* moves away from the Gandhian ideology of villages being the idealistic place, and the idea that, change in social order is possible through change of heart among elite class. Premchand shows problem in Hori's fatalistic behavior and his meek adherence to the prevalent social order and norms, along with that, village elite with their unquestioned power, strangle the dreams of the peasants. Hori is too meek and submissive and never questions the traditions. In a way he can be blamed for his own tragedy.

It is true that the rural society has taken the whole sympathy of Premchand, in terms of its suffering peasant class and city does not. He also believed in the village community's sanctity. Especially, the fact that their harmonious life is being crushed by the elite class living in the city. We also feel pity for a poor peasant like Hori who dies miserably. But he doesn't idealize the village society; also he wants to show the stark reality of that time, in which he has been writing.

It's only Gobar who stands for himself, even though his future is not clear in the end. But it's for sure that he won't follow the suffocating ideas of the society. Hori's sad death in the end of the book fills the readers with a sense of hopelessness, through Hori's plight, the writer questions the social system, and wants to make the people realize, the dilapidating conditions peasants are living in, and how much

necessary it is to bring change in the society.

The writer's intention is focused on understanding and criticizing the problems prevalent in the society. This can be eradicated, only if the people understood it in full gravity. The book questions the degrading conditions of the poor peasants, which is still prevalent in the society. Premchand emphasizes a total change in the society.

Works Cited

- Joshi, Dr. P.C. "Munshi Premchand and the Indian Village". *Premchand Our Contemporary*. Ed.
- Shiv Kumar Misra, New Delhi: National Publishing House, 1986. 39-55. Print.
- Kumar, Prem. "The City in Premchand's Novels". *Journal of South Asian Literature*, vol. 25.
- No.1, 1990, p.p. 67-75. *JSTOR,* www.jstor.org/stable/40873111
- Premchand. *Gaban: The Stolen Jewels.* Trans. Christopher. R. King. Delhi: Oxford University
- Press, 2000.
- Premchand. *Godaan: The Gift of a Cow*. Trans. Gordon C. Roadarmel. Delhi: Orient Longman,
- 2007.
- Premchand. *Karmabhumi.* Trans. Lalit Srivastava. Delhi: Oxford University Press, 2006.
- Premchand. *Sevasadan*. Trans. Snehal Shingavi. Delhi: Oxford University Press, 2005.

Relationship of Selected Anthropometric Measurements Physical Fitness Components and Physiological Parameters Highly Correlated with Sprinting Ability of Inter-Collegiate Sprinters

V. Viju, Ph.d -Scholar, Department of Physical Education, Annamalai University.
***Dr. P. Sivakumar,** (Research Guide) Assistant Professor, Department of Physical Education, Annamalai University.*
Dr. Y. Wise Blessed Singh, Associate Professor, Department of Physical Education, Annamalai University.

Abstract

The intension of the study was to investigate the selected anthropometric measurements, physical, physiological parameters highly correlated with sprinting ability of inter-collegiate level sprinters. To attain this aim, the investigator selected 330 male inter-collegiate level sprinters as subjects. Random group design was used for this investigation, as it is most suitable. The age of the selected subjects was from eighteen to twenty five years. In this study one criterion (sprinting ability) and sixteen determinant variables were included. Pearson product moment correlation was utilized to verify the association between criterion (sprinting ability) and determinant variables. The relationship between criterion and determinant variables as well as inter-correlations among determinant variables was calculated by using Pearson product-moment correlation formula. To test the hypothesis 0.05 level of confidence was fixed. The sprinting ability (SA) is significantly correlated with height, arm length, leg length, thigh girth, calf girth, speed, explosive power, muscular strength endurance, dynamic balance, breath holding time, VO_2max and anaerobic power of the sprinters.

Keywords: *Anthropometric, physical, physiological parameters and sprinters*

INTRODUCTION

The superior performance of today's athletes is the result of a complex blend of many factors (MacDougall et al., 1991). These factors include genetic endowment, physiology, biomechanics, training, health status, and experience. Champion athletes, depending on their specific sports, vary considerably in their physiological attributes (Daniels, 1974). It is therefore necessary to gain an understanding of the essential performance characteristics of a specific sport, in order to develop optimal training strategies for the athlete.

Sprinting is running over a short distance at the top-most speed of the body in a limited period of time. It is used in many sports that incorporate running, typically as a

way of quickly reaching a target or goal, or avoiding or catching an opponent. Sprint running races are short distances races in which athletes try to run at their maximum speed throughout the entire distance of the race. Sprint races are part of the track and field discipline and are included in all events that feature track and field competitions. Three sprints are currently held at the modern Summer Olympics and outdoor World Championships: the 100 metres, 200 metres, and 400 metres.

As compared to other sprinting events, the relative simplicity of the 100 m sprint makes it ideal for studying the elements of sprint running. Unlike other track-and-field sprints, such as the 200 m or 400 m event, the 100 m sprint does not involve a curve of the track. Thus, running technique involves purely linear movement, and no centrifugal or centripetal (outward and inward radial) forces. Given recent world record accomplishments in the male 100 m sprint event, it is assumed that a review of this event, and the multiple determinants to 100 m sprint performance would be a timely addition to the scientific and coaching literature within athletics. Consequently, the purpose of this study was to identify the features of the 100 m sprint that make it such an iconic event, and summarize the multi-faceted determinants to sprint running performance so that understanding and commentary on performance can be based on science rather than speculation or personal bias. Taking this into consideration the research scholar has decided to conduct his research on the same and find the solution of the problem. This research will be useful for both sprinters as well as coaches to improve sprint performance.

METHODOLOGY

Selection of Subjects

To determine the association between the criterion and determinant variables, three hundred and thirty male inter-collegiate level sprinters from various arts and science colleges affiliated to Manonmaniam Sundaranar University, Tirunelveli and also from Madurai Kamaraj University, Madurai, Tamilnadu were chosen. Random group design was used, as it is most appropriate. The age of the subjects was from 18 to 25 years.

Selection of Variables

Criterion Variable: The 100m sprinting performance of the selected sprinters were considered as criterion variable.

Anthropometric Measurements: The following anthropometric variables namely Height, arm length, leg length, thigh girth and calf girth were selected.

Physical fitness components: The physical fitness components such as maximum speed, explosive power, muscular strength, flexibility and dynamic balance were selected.

Physiological parameters: The physiological parameters such as resting heart rate, breath holding time, anaerobic power, forced vital capacity and Vo_2max were selected.

Collection of Data

The sprinting ability of the subjects was assessed by conducting 100m race and the selected anthropometric measurements, physical fitness components and physiological parameters were measured through standard test and measurements.

Statistical Techniques

In this study one criterion (sprinting ability) and sixteen determinant variables are included. Pearson product moment correlation was utilized to verify the association between criterion (sprinting ability) and determinant variables. The relationship between criterion and determinant variables as well as inter-correlations among determinant variables was calculated by using Pearson product-moment correlation formula. To test the hypothesis 0.05 level of confidence was fixed.

Result

The descriptive statistics– range, minimum, maximum, mean and standard deviation of anthropometric, physical, physiological parameters and sprinting ability of sprinters have been presented in table-I.

Table – I
Descriptive Statistics Results of Chosen Anthropometric, Physical, Physiological Parameters and Sprinting Ability among Sprinters

	N	Range	Minimum	Maximum	Mean	Std. Deviation
Height	330	15.00	154.00	169.00	1.6099E2	4.18311
Arm length	330	15.00	54.00	69.00	60.9939	4.18202
Leg length	330	10.00	69.00	79.00	75.0636	2.82287
Thigh girth	330	9.00	39.00	48.00	43.2333	2.72723
Calf girth	330	7.00	25.00	32.00	28.5030	1.56762
Speed	330	0.84	4.14	4.98	4.5257	.14345
Power	330	50.00	2.00	52.00	45.2030	4.16141
Strength	330	10.00	59.00	69.00	64.9455	2.77035
Flexibility	330	6.00	12.00	18.00	15.2576	1.82777
Balance	330	8.00	35.00	43.00	39.0636	1.96138
RHR	330	3.00	65.00	68.00	66.4758	1.19816
BHT	330	31.00	37.00	68.00	40.33	2.55
Anaerobic	330	26.00	260.00	286.00	2.7523E2	5.53767
FVC	330	0.54	3.05	3.59	3.3423	0.15795
Vo_2max	330	0.31	2.64	2.95	2.8035	0.09017
Sprinting	330	2.20	11.10	13.30	12.0795	0.61959

Correlation Analysis

The Inter-relationships between chosen anthropometric, physical, physiological parameters with sprinting ability of sprinters were computed using Pearson Product Moment Correlation and results are given in Table – II.

Table –II: Inter-Correlation Results on Selected Anthropometric, Physical, Physiological Parameters with Sprinting Ability of Male Sprinters

	SA	Ht	AL	LL	TG	CG	SP	EP	MSE	Flex	DB	RHR	BHT	AP	FVC	VO2
SA	1	0.301*	0.287*	0.318*	0.163*	0.161*	0.229*	0.285*	0.284*	0.053	0.200*	0.006	0.112*	0.619*	0.018	0.394*
Ht		1	0.998*	0.975*	0.599*	0.243*	0.144*	0.736*	0.707*	0.006	0.325*	0.029	0.086	0.394*	0.347*	0.707*
AL			1	0.976*	0.578*	0.250*	0.131*	0.724*	0.691*	0.003	0.331*	0.013	0.098	0.390*	0.341*	0.698*
LL				1	0.467*	0.231*	0.156*	0.688*	0.706*	0.010	0.337*	0.090	0.028	0.383*	0.360*	0.703*
TG					1	0.088	0.217*	0.659*	0.479*	0.060	0.228*	0.275*	0.236*	0.134*	0.133*	0.465*
CG						1	0.308*	0.031	0.108	0.133*	0.265*	0.139*	0.073	0.086	0.141*	0.365*
MS							1	0.155*	0.245*	0.317*	0.106	0.231*	0.178*	0.310*	0.254*	0.185*
EP								1	0.646*	0.071	0.130*	0.149*	0.131*	0.273*	0.309*	0.343*
MSE									1	0.097	0.243*	0.046	0.101	0.117*	0.369*	0.445*
Flex										1	0.183*	0.106	0.076	0.144*	0.282*	0.087
DB											1	0.082	0.160*	0.014	0.050	0.369*
RHR												1	0.912*	0.132*	0.002	0.185*
BHT													1	0.014	0.044	0.053
AP														1	0.328*	0.134
FVC															1	0.261*
Vo_2																1

**The required table 'r' value is 0.109 at 0.05 level of confidence.*

SA	Sprinting Ability	CG	Calf girth	DB	Dynamic balance
Ht	Height	SP	Speed	RHR	Resting heart rate
AL	Arm Length	EP	Explosive power	BHT	Breath holding time
LL	Leg Length	MSE	Muscular strength endurance	AP	Anaerobic power
TG	Thigh Girth	Flex	Flexibility	FVC	Forced vital capacity
				Vo_2	Vo_2 max

The following anthropometrical variables; height (0.301), arm length (0.287), leg length (0.318) thigh girth (0.163), calf girth (0.161) were significantly correlated with the sprinting ability. High correlation also existed between sprinting ability versus selected physical fitness components namely speed (0.229), explosive power (0.285), muscular strength endurance (0.284) and dynamic balance (0.200). The chosen physiological components; breath holding time (0.112), VO_2max (0.394) and anaerobic power (0.619) was significantly correlated with the sprinting ability. As the obtained 'r' values was found at 0.05 level of confidence was higher than required table 'r' value 0.109. The obtained and required 'r' values of selected anthropometric measurements with sprinting ability is displayed in table-III.

Table – III: Correlation between Criterion and Anthropometric Measurements

S.No	Variables Correlated	Obtained 'r'
1.	Sprinting and Standing Height	0.301*
2.	Sprinting Ability and Arm Length	0.287*
3.	Sprinting Ability and Leg Length	0.318*
4.	Sprinting Ability and Thigh Girth	0.163*
5.	Sprinting Ability and Calf Girth	0.161*

**The required table 'r' value is 0.109 (0.05 level)*

The sprinting ability was significantly correlated with the selected anthropometric measurements such as height, arm length, leg length, thigh girth and calf girth of the sprinters since the obtained correlation coefficient values 0.301, 0.287, 0.318, 0.163 and 0.161 are greater than the required table value (0.109). The obtained correlation coefficient values between sprinting ability and the selected anthropometric measurements are graphically represented in figure-I.

Figure-I: Diagram Showing the Correlation Coefficient Values between Sprinting Ability and the Selected Anthropometric Measurements

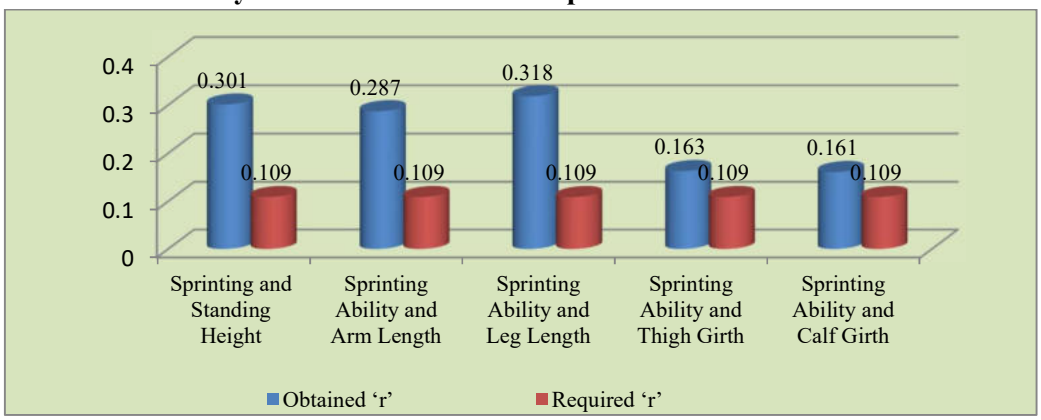

The obtained and required 'r' values of selected physical fitness components with sprinting ability is displayed in table-IV.

Table – IV: Correlation between Criterion and Physical Fitness Components

S.No	Variables Correlated	Obtained 'r'
1.	Sprinting Ability and speed	0.229*
2.	Sprinting Ability and explosive power	0.285*
3.	Sprinting Ability and muscular strength endurance	0.284*
4.	Sprinting Ability and flexibility	0.053
5.	Sprinting Ability and dynamic balance	0.200*

**The required table 'r' value is 0.109 (0.05 level)*

The sprinting ability was significantly correlated with the selected physical fitness components namely speed (0.229), explosive power (0.285), muscular strength endurance

(0.284) and dynamic balance (0.200), as the required table 'r' value was 0.109 found at 0.05 level of confidence was higher than obtained 'r' values. However sprinting ability were not significantly correlated with flexibility (0.053) of the sprinters. The obtained correlation coefficient values between sprinting ability and the selected physical fitness components are graphically represented in figure-II.

Figure-II: Diagram Showing the Correlation Coefficient Values between Sprinting Ability and the Selected Physical Fitness Components

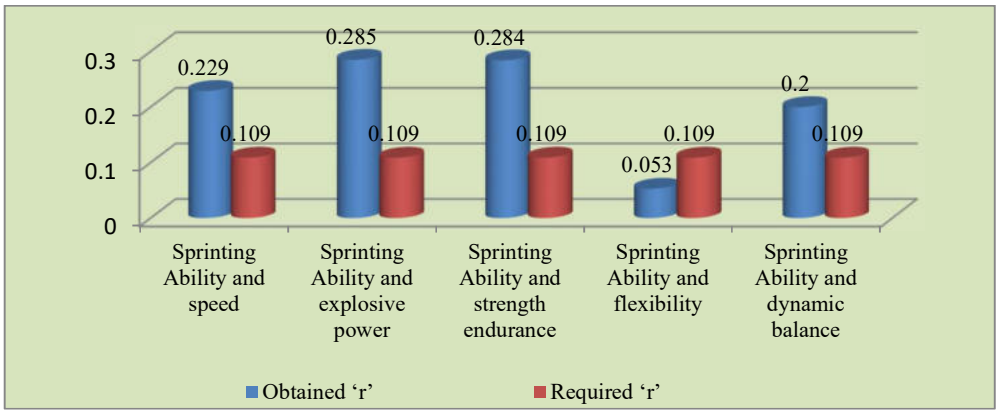

The obtained and required 'r' values of chosen physiological parameters with sprinting ability is displayed in table-V

Table – V: Correlation Co-Efficient between Criterion and Selected Physiological Parameters

S.No	Variables Correlated	Obtained 'r'
1.	Sprinting Ability and resting heart rate	0.006
2.	Sprinting Ability and breath holding time	0.112*
3.	Sprinting Ability and Anaerobic power	0.619*
4.	Sprinting Ability and Forced vital capacity	0.018
5.	Sprinting Ability and VO_2max	0.394*

**The required table 'r' value is 0.28 (0.05 level)*

The sprinting ability was significantly correlated with the chosen physiological parameters breath holding time (0.112), anaerobic power (0.619) and VO_2max (0.394) as the required table 'r' value 0.109 found at 0.05 level of confidence is higher than obtained 'r' values. However sprinting ability was not significantly correlated with resting heart rate (0.006) and Forced vital capacity (0.018) of the sprinters.

Figure-III: Diagram Showing the Correlation Coefficient Values between Sprinting Ability and the Selected Physiological Parameters

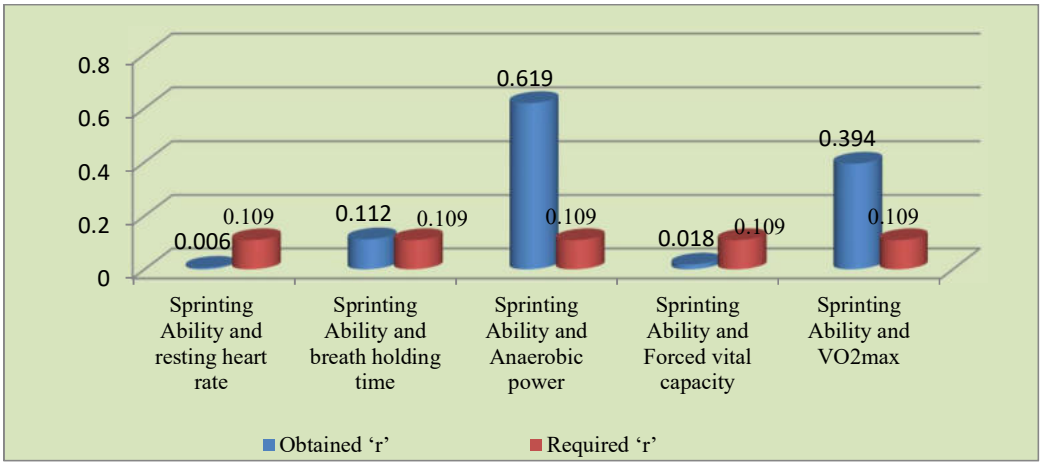

Discussion

Ramachandra and Shelvam (2017) identified the predominance of anthropometric variables between the sprinters. The variables in order of priority were standing height, foot breadth, chest breadth, upper leg length, thigh girth, wrist girth, calf girth, weight, ankle girth and foot length. Niels-Uth (2005) compared the anthropometry of sprinters and people belonging to the normal population. Both male and female sprinters had lower body mass index (BMI) than the normal populations. It has been suggested that particular anthropometric measures are pre-requisites for good athletic performance in various sports (Kukolj et al., 1999). The anthropometric dimensions measured in this study revealed significant relationships with sprint performance. Hunter and coworkers (2004) reported that height and leg length to be good predictors of acceleration phase velocity.

High performance sprint running from a block start requires the production of both high level forces and angular velocities (Harland & Steele, 1997; Mero et al., 1983; Mero et al., 1992). Specifically, large forces generated by the leg musculature whilst in the starting blocks can lead to a performance edge over the other competitors in the race (Harland & Steele, 1997). An explosive sprint start requires a powerful angular drive of the arms, hips and legs (Hoster & May, 1979; Korchemny, 1992). An athlete's relative explosive ability of their hip and knee extensors is critical to sprint performance. In fact the stored elastic energy has been suggested to be necessary to sprint performance (Mero et al., 1992).

Human physiology and physique combine to be the most influential determinants of improved sprint performance (Majumdar & Robergs, 2011). Physiological profiling is

used within team sports to assess both the demands of the sport and provide evidence of position specific requirements (Geithner et al., 2006). Differences in positional demands have been found between playing positions, the centre positions being the most active (McManus & Stevenson, 2007). For all athletes involved in high professional competitive sports the body is required to perform at optimum capacity in terms of biomechanics and physiology (Zaccagni, 2012).

Conclusion

The sprinting ability was significantly correlated with height, arm length, leg length, thigh girth, calf girth, speed, explosive power, muscular strength endurance, dynamic balance, breath holding time, VO_2max and anaerobic power was significantly correlated with the sprinting ability. Present day science is very much interested in estimating the optimum anthropometric, physical, physiological make-up of sprinters. So the scanning and selection of sprinters may be achieved successfully to a great extent by measuring anthropometric, physical, physiological parameters.

References

Geithner, C.A., Lee, A.M., Braco, M.R., (2006). Physical and Performance Differences among Forwards, Defensemen and Goalies in Elite Women's Hockey, *J. Stren Cond Res.,* 20(3): 500-505.

Harland M.J., Steele J.R. (1997). Biomechanics of the sprint start, *Sports Medicine,* 23: 11-20.

Hoster M. & May E. (1979). Notes on the biomechanics of the sprint start, *Athletics Coach,* 13: 2-7.

Hunter J.P., Marshall R.N., McNair P.J. (2004). Interaction of step length and step rate during sprint running, *Medicine and Science in Sports and Exercise,* 36: 261-271.

Korchemny, R. (1992). A new concept for sprint start and acceleration training, *New Studies in Athletics*, 7: 65-72.

Kukolj, M., Ropret, R., Ugarkovic, D., Jaric, S. (1999). Anthropometric, strength, and power predictors of sprinting performance, *J Sports Med Phys Fitness*, 39(2): 120-122.

Majumdar, Aditi S. and Robergs, Robert A. (2011). The Science of Speed: Determinants of Performance in the 100 m Sprint, *International Journal of Sports Science & Coaching,* 6(3): 2011 479.

McManus, A., and Stevenson, M., (2007). Quantifying the physical demands in netball to develop training guidelines that assess player preparation and reduce injury, *J. Sci Med Spo*., 10(1): 85.

Mero A., Luhtanen P., Komi P.V. (1983). A biomechanical study of the sprint start, *Scandinavian Journal of Sports Science*, 5: 20-28.

Mero A., Komi P.V., Gregor R.J. (1992). Biomechanics of sprint running, A review, *Sports Medicine,* 13: 376-392.

Niels-Uth (2005). Anthropometric Comparison of World-Class Sprinters and Normal Populations, *J Sports Sci Med*., 4(4): 608–616.

Ramachandra, K. and Shelvam, P. V. (2017). Anthropometric Variables and Performance to Predict among College Sprinters, *International Journal of Engineering Technology Science and Research*, 4(10).

Zaccagni, L. (2012). Anthropometric characteristics and body composition of Italian national wrestlers, *Eur. J. Sport Sci.,* 12(2):145-51.

GIS SCIENCE JOURNAL

An UGC-CARE Approved Group II Journal

ISSN NO : 1869-9391 / Website : www.gisscience.net /
Email : editorgsjournal@gmail.com

Certificate of Publication

Paper ID : GSJ/8974

This is to certify that the paper titled

Relationship of Selected Anthropometric Measurements Physical Fitness Components and Physiological Parameters Highly Correlated with Sprinting Ability of Inter-Collegiate Sprinters

Authored by

V. Viju

From

Annamalai University

Has been published in

GIS SCIENCE JOURNAL Volume 9, Issue 11, November 2022.

UGC APPROVED JOURNAL

DOI: 20.18001.GSJ

crossref member

CROSSREF.ORG THE CITATION LINKING BACKBONE

M Palaniswami
Editor-in-chief
GISSCIENCE

6.1 IMPACT FACTOR

PREDICTION OF THE FACTORS PREDOMINANT TO SPRINTING ABILITY OF INTER-COLLEGIATE LEVEL SPRINTERS

V. Viju, Ph.d -Scholar, Department of Physical Education, Annamalai University.
***Dr. P. Sivakumar,** (Research Guide) Assistant Professor, Department of Physical Education, Annamalai University.*
Dr. M. John, Assistant Professor, Department of Physical Education, Annamalai University.

Abstract

The aim of this investigation was to determine the factors predominant to sprinting ability of university level sprinters. To attain this aim, the investigator selected 330 male inter-collegiate level sprinters as subjects. Random group design was used for this investigation, as it is most suitable. The age of the selected subjects was from eighteen to twenty five years. In this study one criterion (sprinting ability) and twenty determinant variables (anthropometric measurements, physical fitness components, physiological parameters and speed related parameters) were included. The relationship between criterion and determinant variables as well as inter-correlations among determinant variables was calculated by using Pearson product-moment correlation formula. The computation of multiple regressions was also used. Multiple regressions analysis was used to find out the predictor variable that has the highest correlation with the criterion variables and it is entered into the equation first. The rest of the variables are entered into the equation depending on the contribution of each predictor. To test the hypothesis 0.05 level of significance was fixed. The regression equation for the sprinting ability includes acceleration speed, stride frequency and anaerobic power.

Keywords: *Anthropometric, Physical, Physiological, Speed parameters and Sprinters*

INTRODUCTION

100m sprint event is a spectacular event in track and field, it is a most dominant event compare with all other events. In the short distance running there is a purpose to overcome the gifted distance in the shortest possible time. The decisive factors of the sports performance structure are maximal running speed and the ability to keep it as longer as possible (speed endurance). Even in many different sports and events the maximal running speed participates either directly or not on the level of sports performance and sportsman's successfulness. That is why the development of speed abilities is very topical problem of the sports theory and practice. The great deal of genetic determination and limited possibilities of the speed abilities' development turn attention for the selection of talented youth and look for new, more effective means and methods of development.

Performance is the ability to achieve the high score in sprinting competitive event. Athletes are always in search of more speed. Running speed is an essential component of most major sports, and can be the determining factor in the outcome of a sporting event. It

is for this reason that athletes undertake training programs to improve their individual speeds. In order to gain a performance advantage, athletes are always in search of newer methods. While team court sports have been widely researched, few studies have been conducted comparing predominant characteristics of sprinters. Hence, this kind of analysis will allow the identification of the different components of performance and how they interact to influence performance in sprint.

Running speed is an essential component of most of the major sports. Often, it is the determining factor in the outcome of a sporting event. Thus, the ability to enhance running speed is of prime importance to coaches and athletes. Since the researcher is a sprinter, the investigator feels that there is a need for an analytical study in order to discriminate the dominant factors associated with the sprinting performance of inter-collegiate level sprinters. Moreover, limited number of researches had been done among inter-collegiate level sprinters, and also there is a lack of descriptive data on the sprinting ability of inter-collegiate level sprinters. This has motivated to take up the study to predict the factors predominant to the sprinting ability of inter-collegiate level sprinters.

METHODOLOGY

Selection of Subjects

To determine the association between the criterion and determinant variables, three hundred and thirty male inter-collegiate level sprinters from various arts and science colleges affiliated to Manonmaniam Sundaranar University, Tirunelveli and also from Madurai Kamaraj University, Madurai, Tamilnadu were chosen. Random group design was used, as it is most appropriate. The age of the subjects was from 18 to 25 years.

Selection of Variables

Criterion Variable: The 100m sprinting performance of the selected sprinters were considered as criterion variable.

Anthropometric Measurements: The following anthropometric variables namely Height, arm length, leg length, thigh girth and calf girth were selected.

Physical fitness components: The physical fitness components such as maximum speed, explosive power, muscular strength, flexibility and dynamic balance were selected.

Physiological parameters: The physiological parameters such as resting heart rate, breath holding time, anaerobic power, forced vital capacity and Vo_2max were selected.

Speed Parameters: Reaction time, acceleration speed, stride length, stride frequency and speed endurance were selected.

Collection of Data

The sprinting ability of the inter-collegiate level sprinters was assessed by conducting 100m race and the selected anthropometric measurements, physical fitness components and physiological parameters were measured through standard test and measurements.

Statistical Techniques

In this study one criterion (sprinting ability) and twenty determinant variables are included. The relationship between criterion and determinant variables as well as inter-correlations among determinant variables was calculated by using Pearson product-moment correlation formula. The computation of multiple regressions was also used. In multiple regressions, a criterion variable was predicted from a set of predictors. Multiple regressions analysis was used to find out the predictor variable that has the highest correlation with the criterion variables and it is entered into the equation first. The rest of the variables are entered into the equation depending on the contribution of each predictor. To test the hypothesis 0.05 level of significance was fixed.

Result

The descriptive statistics– range, minimum, maximum, mean and standard deviation of anthropometric, physical, physiological, speed parameters and playing ability of sprinters have been presented in table-I.

Table – I: Descriptive Statistics Results of Chosen Anthropometric, Physical, Physiological, Speed Parameters and Sprinting Ability among Sprinters

	N	Range	Minimum	Maximum	Mean	SD
Height	330	15.00	154.00	169.00	1.6099E2	4.18311
Arm length	330	15.00	54.00	69.00	60.9939	4.18202
Leg length	330	10.00	69.00	79.00	75.0636	2.82287
Thigh girth	330	9.00	39.00	48.00	43.2333	2.72723
Calf girth	330	7.00	25.00	32.00	28.5030	1.56762
Speed	330	0.84	4.14	4.98	4.5257	0.14345
Power	330	50.00	2.00	52.00	45.2030	4.16141
Strength	330	10.00	59.00	69.00	64.9455	2.77035
Flexibility	330	6.00	12.00	18.00	15.2576	1.82777
Balance	330	8.00	35.00	43.00	39.0636	1.96138
RHR	330	3.00	65.00	68.00	66.4758	1.19816
BHT	330	31.00	37.00	68.00	40.33	2.55
Anaerobic	330	26.00	260.00	286.00	2.7523E2	5.53767
FVC	330	0.54	3.05	3.59	3.3423	0.15795
Vo_2max	330	0.31	2.64	2.95	2.8035	0.09017
Reaction	330	0.10	0.17	0.27	0.2239	0.02521
Acceleration	330	2.10	4.20	6.30	5.1763	0.51255
Stride length	330	0.22	1.63	1.85	1.7479	0.06054

Frequency	330	1.09	4.11	5.20	4.6064	0.29366
Endurance	330	2.13	17.12	19.25	18.0963	0.58069
Sprinting	330	2.20	11.10	13.30	12.0795	0.61959

Correlation Analysis

The inter-relationships between chosen anthropometric, physical, physiological and speed parameters with playing ability of sprinters were computed using Pearson Product Moment Correlation. It was evident from the Pearson Product Moment Correlation results that sprinting ability (SA) is significantly correlated with are height, arm length, leg length, thigh girth, explosive power, muscular strength, anaerobic power, VO_2max, reaction time, stride frequency and speed endurance of sprinters.

The following anthropometrical variables; height (0.301), arm length (0.287), leg length (0.318) thigh girth (0.163), calf girth (0.161) were significantly correlated with the sprinting ability. High correlation also existed between sprinting ability versus selected physical fitness components namely speed (0.229), explosive power (0.285), muscular strength endurance (0.284) and dynamic balance (0.200). The chosen physiological components; breath holding time (0.112), VO_2max (0.394) and anaerobic power (0.619) was significantly correlated with the sprinting ability. The selected speed parameters namely reaction time (0.847), acceleration speed (0.999), stride length (0.790), speed frequency (0.944), speed endurance (0.393) were highly correlated with the sprinting ability of the sprinters. As the obtained 'r' values was found at 0.05 level of confidence was higher than required table 'r' value 0.109.

The obtained and required 'r' values of selected anthropometric, physical, physiological, speed parameters with sprinting ability is displayed in table-I.

Table – I: Correlation between Criterion and Determinant Variables

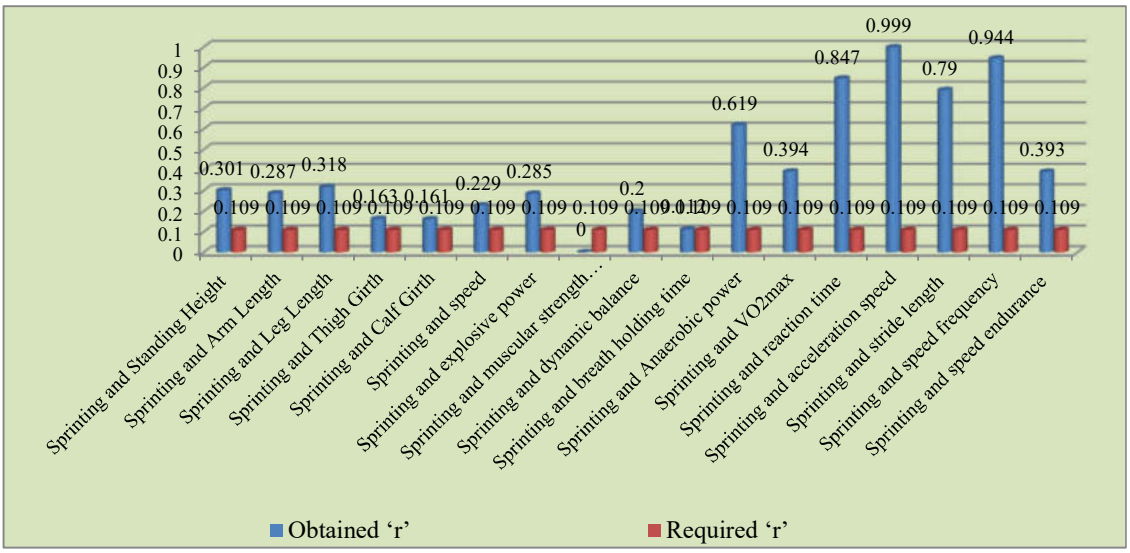

Step-Wise Multiple Regression Analysis

Stepwise multiple regression was computed to explore the prediction of dominant factors of sprinting ability from the predictor variables of inter-collegiate sprinters.

The analysis of variance for the influence of predictor variables on sprinting ability among inter-collegiate sprinters is in table -II.

Table II: Analysis of Variance for the Influence of Predictor Variables on Sprinting Ability Among Inter-collegiate Level Sprinters

Model		Sum of Squares	df	Mean Square	F	Sig.
1	Regression	8.877	1	8.877	15252.182	.000[b]
	Residual	0.016	28	0.001		
	Total	8.894	29			
2	Regression	8.884	2	4.442	12062.074	.000[c]
	Residual	0.010	27	.000		
	Total	8.894	29			
3	Regression	8.885	3	2.962	9077.734	.000[d]
	Residual	0.008	26	.000		
	Total	8.894	29			

a. Dependent Variable: sprint ability
b. Predictors: (Constant), ACCSPEED
c. Predictors: (Constant), ACCSPEED, STFRE
d. Predictors: (Constant), ACCSPEED, STFRE, ANEROBIC

It was clear from the table-II that the obtained 'F' value 15252.18, 120602.07 and 9077.73 are significant (0.05 levels). Hence, all the independent variables are collectively influenced on the sprinting ability of sprinters.

As the F ratio is significant multiple regressions was computed. Multiple regression equation was computed only because the multiple correlations were sufficiently high to warrant prediction from it. Then, the correlation identified the independent variables to be included and their order in the regression equation. Multiple correlations were computed by step-wise argument method and the results were presented in Table – III.

Table-III: Step-Wise Multiple Regression between Sprinting Ability and Independent Variables of Sprinters

Model	R	R Square	Adjusted R Square	Std. Error of the Estimate
1	0.999[a]	0.998	0.998	0.02413
2	0.999[b]	0.999	0.999	0.01919
3	1.000[c]	0.999	0.999	0.01806

a. Predictors: (Constant), ACCSPEED
b. Predictors: (Constant), ACCSPEED, STFRE
c. Predictors: (Constant), ACCSPEED, STFRE, ANEROBIC

From table-III, it was found that the multiple correlations co-efficient for predictors, such as acceleration speed, stride frequency and anaerobic power was 1.000 which produce highest multiple correlations with sprinting ability. 'R' square values show that the percentage of contribution of predictors to the sprinting ability (Dependent variables) is in the following order.

1. About 99.8% of the variation in the sprinting ability was explained by the regression model with one predictor acceleration speed.

2. About 99.9% of the variation in the sprinting ability was explained by the regression model with two predictors, acceleration speed and stride frequency. An additional 0.001% of the variance in the sprinting ability was contributed by stride frequency.

3. About 99.9% of the variation in the sprinting ability was explained by the regression model with three predictors, acceleration speed, stride frequency and anaerobic power. An additional 0.001% of the variance in the sprinting ability was contributed by anaerobic power.

Multiple regression equation was computed and the obtained results are presented in Table – IV.

Table-IV: Regression Analysis of Prediction Equation of Sprinters (Stepwise Method)

Model		Unstandardized Coefficients		Standardized Coefficients	t	Sig.
		B	Std. Error	Beta		
1	(Constant)	6.911	.041		168.176	.000
	ACCSPEED	1.017	.008	.999	123.500	.000
2	(Constant)	6.517	.100		64.915	.000
	ACCSPEED	.945	.018	.929	51.112	.000
	STFRE	.160	.039	.075	4.154	.000
3	(Constant)	7.189	.332		21.674	.000
	ACCSPEED	.941	.017	.925	53.782	.000
	STFRE	.146	.037	.069	3.968	.001
	ANEROBIC	-.002	.001	-.016	-2.115	.044

a. Dependent Variable: sprinting ability

Predictors in the Model 1: (Constant), Acceleration Speed.

Predictors in the Model 2: (Constant), Acceleration Speed, stride frequency.

Predictors in the Model 3: (Constant), Acceleration Speed, stride frequency and anaerobic power.

From the Table-IV, the following regression equations were derived for sprinting ability of sprinters.

Regression Equation in obtained scores form = CR

Sprinting Ability = 6.911 + 0.941 (Acceleration Speed) + 0.146 (stride frequency) - 0.002 (anaerobic power)

The regression equation for the dominant factors of sprinting ability includes acceleration speed, stride frequency and anaerobic power. As the multiple correlations on dominant factors of sprinting ability with the combined effect of these predictor variables are highly significant, it is apparent that the obtained regression equation has a high predictive validity.

Discussion

According to the current study, the apparent importance of anthropometric variables in running speed. Stride length increases with body height, and strength and power with muscle development, thereby influencing the sprint performance (Papaiakovou, et al., 2009). The improvement in sprint performance is related to the maturation of the neural system and improved muscle/neural coordination, in addition to the increase in muscle mass (Malina, Bouchard & Bar-Or. 2004). Wong et al., (2009) found that taller players performed better in 10 m and 30 m sprint. In the growth spurt, the variations in maturation for the same chronological age have been shown be as

much as 2 or 3 years, or even more, and Malina et al., (2007) suggest that body mass and maturity account for 50% of variance in short sprint.

Barrera et al., (2022) analyze the relationship between sprint performance (time), and strength and power capabilities in football players and found that peak torque at higher velocities and vertical jump performance correlates significantly with linear sprint performance. Suarez-Arrones et al., (2020) suggested that despite the existence of substantial correlations between variables, straight linear sprinting, jumping performance, CODs and squat power were, for the most part, separate motor qualities, suggesting that all of them should be specifically assessed and trained. Loturco et al., (2019) identified that maximum running speed is a very complex physical capacity, which should be assessed and trained using several methods and training strategies.

Human physiology and physique combine to be the most influential determinants of improved sprint performance (Majumdar & Robergs (2011). Physiological profiling is used within team sports to assess both the demands of the sport and provide evidence of position specific requirements (Geithner et al., 2006). For all athletes involved in high professional competitive sports the body is required to perform at optimum capacity in terms of biomechanics and physiology (Zaccagni, 2012).

Numerous investigators have attempted to isolate predictive factors for the selection of track and field athletes (Foreman, 1989; Henson et al., 1989a). Alabin et al., (1980) identified the following factors as predictors of track and field talent: height, weight, speed, stride frequency and stride length, reaction time, strength, power, endurance, coordination, psychological approaches, intellectual level, and biological growth rate. Foreman (1989) outlined some of the characteristics related to successful performance in terms of relative importance in various events. In the area of sprints and hurdles, natural speed, power, stride cadence, strength, movement time, and low percent fat were considered important.

Conclusion

The sprinting ability was significantly correlated with height, arm length, leg length, thigh girth, calf girth, speed, explosive power, muscular strength endurance, dynamic balance, breath holding time, VO_2max and anaerobic power, reaction time, stride frequency and speed endurance of sprinters. The predictor variables namely acceleration speed, stride frequency and anaerobic power can be used to predict the sprinting ability of inter-collegiate level sprinters.

References

Alabin, V., Nischt, G., & Jefimov, W. (1980). Talent selection, *Modem Athlete and Coach*, 18(1). 36-37.

Barrera, J. et al., (2022). Predictors of linear sprint performance in professional football players. *Biology of Sport*, *40*(2), 359-364.

Foreman, K. (1989). The use o f talent-predictive factors in the selection of track and field athletes. In V. Gambetta (Ed.), The Athletics Congress's track and field coaching manual (2nd ed.) (pp. 31-36). Champaign, IL: Leisure Press.

Geithner, C.A., Lee, A.M., Braco, M.R., (2006). Physical and Performance Differences among Forwards, Defensemen and Goalies in Elite Women's Hockey, *J. Stren Cond Res.,* 20(3): 500-505.

Henson, P., Turner, P . , & Lacourse, M. (1989a). Talent identification in track and field, *Report submitted to The Athletics Congress*.

Loturco, Irineu et al., (2019). Predictive Factors of Elite Sprint Performance: Influences of Muscle Mechanical Properties and Functional Parameters, *Journal of Strength and Conditioning Research*, 33(4):974-986.

Majumdar, Aditi S. and Robergs, Robert A. (2011). The Science of Speed: Determinants of Performance in the 100 m Sprint, *International Journal of Sports Science & Coaching* Volume, 6(3): 2011 479.

Malina RM, Ribeiro B, Aroso J, Cumming SP. (2007). Characteristics of youth soccer players aged 13–15 years classified by skill level, *Br J Sports Med*., 41: 290–295.

Malina, R. M., Bouchard, C., & Bar-Or, O. (2004). Growth, Maturation and Physical Activity (2nd ed.). Champaign, IL: Human Kinetics.

Papaiakovou, G. et al., (2009). The effect of chronological age and gender on the development of sprint performance during childhood and puberty, *J Strength Cond Res*., 23:2568–2573.

Suarez-Arrones, Luis et al., (2020). Relationships between Change of Direction, Sprint, Jump, and Squat Power Performance, *Sports,* 8(3): 38.

Wong PL, Chamari K, Dellal A, Wisløff U. (2009). Relationship between anthropometric and physiological characteristics in youth soccer players, *J Strength Cond Res*., 23(4):1204–1210.

Zaccagni, L. (2012). Anthropometric characteristics and body composition of Italian national wrestlers, *Eur. J. Sport Sci.,* 12(2):145-51.

AEGAEUM JOURNAL

An UGC-CARE Approved Group - II Journal

An ISO : 7021 - 2008 Certified Journal

ISSN NO: 0776-3808 / web: www.aegaeum.com / e-mail: submitaj@gmail.com

Certificate of Publication

This is to certify that the paper entitled

"PREDICTION OF THE FACTORS PREDOMINANT TO SPRINTING ABILITY OF INTER-COLLEGIATE LEVEL SPRINTERS"

Authored by:

V. Viju, Ph.d -Scholar

From

Annamalai University.

Has been published in

AEGAEUM JOURNAL, VOLUME X, ISSUE XI, NOVEMBER - 2022

S. Wimberger
Editor-In-Chief
AEGAEUM JOURNAL

6.2 IMPACT FACTOR

ISO International Organization for Standardization 7021-2008